EFFECT OF MINERALOGIC HETEROGENEITY ON ACID FRACTURING EFFICIENCY

A Dissertation

by

XIAO JIN

Submitted to the Office of Graduate and Professional Studies of
Texas A&M University
in partial fulfillment of the requirements for the degree of

DOCTOR OF PHILOSOPHY

Chair of Committee,	Ding Zhu
Committee Members,	Alfred Dan Hill
	Hisham Nasr-El-Din
	Juan Carlos Laya
Head of Department,	Jeffery Spath

August 2020

Major Subject: Petroleum Engineering

ABSTRACT[*]

Creating sufficient and sustained fracture conductivity contributes directly to the success of acid fracturing treatments[*]. The permeability and mineralogy distributions of formation rocks play significant roles in creating non-uniformly etched surfaces that can withstand high closure stress. Previous studies showed that depending on the properties of formation rock and acidizing conditions (acid selection, formation temperature, injection rate, and contact time), a wide range of etching patterns (roughness, uniform, channeling) could be created. Different etching patterns can dictate the resultant fracture conductivity. Insoluble minerals and their distribution can completely change the outcomes of acid fracturing treatments. However large portion of acid fracturing studies is based on experimental investigation and uses homogeneous rock samples such as Indiana limestones that do not represent the highly heterogeneous features of carbonate rocks. This work studies the effect of heterogeneity, and more importantly, the distribution of insoluble rock on acid fracture conductivity.

In this research, acid fracturing experiments were conducted using both outcrop homogeneous Indiana limestone samples and heterogeneous downhole carbonate rock samples. The Indiana limestone tests served as a baseline. The highly heterogeneous carbonate rock samples contain several types of insoluble minerals, such as quartz,

---

[*] Reprinted with permission from Jin, Xiao, Zhu, Ding, Hill, Alfred Daniel et al. 2019. Effects of Heterogeneity in Mineralogy Distribution on Acid-Fracturing Efficiency. *SPE Production & Operations* Preprint (Preprint): 14. https://doi.org/10.2118/194377-PA

anhydrite, pyrite, and various kinds of clays, along with sealed natural fractures. These minerals are distributed in the form of streaks correlated against the flow direction, or as smaller nodules. After acidizing the rock samples, these minerals act as pillars that significantly reduce fracture conductivity decline at higher closure stresses. Both x-ray diffraction (XRD) and x-ray fluorescence (XRF) test results help pinpoint the type and location of different minerals on the fracture surfaces. Surface scans showing surface topography after acidizing injection is captured by a surface profilometer. The surface scan results were used to correlate fracture conductivity as a function of mineralogy distribution. Theoretical models considering geostatistical correlation parameters were used to match and understand the experimental results.

The observations of the experimental study showed that insoluble minerals with higher mechanical properties were less crushed at higher closure stresses, resulting in a less steep conductivity decline with increased closure stress. If the acid-etching creates enough conductivity, the rock sample can sustain higher closure stress with a much lower fracture conductivity decline rate compared with Indiana limestone samples. Fracture surfaces with insoluble mineral streaks correlated against the flow direction offer the benefit of being able to maintain conductivity at high closure stress, but not necessarily high initial conductivity.

Using a fracture conductivity model with correlation length, the fracture conductivity behavior for the homogenous rock samples were matched. To match the downhole samples fracture conductivity behavior, the fracture conductivity model was modified with both x-ray diffraction tests for mineralogy distribution and triaxial tests for

the rock's Young's Modulus. Parametric study with the geostatistical parameters was conducted to show that the fracture surfaces with mineral streaks correlated with the flow direction could increase initial acid fracturing conductivity significantly as compared to the case when the streak is correlated against the flow direction.

The modified fracture conductivity mineralogy model was used in an acid fracturing model to calculate the overall fracture conductivity after the acid etched-width has been determined and the model is validated with the production data from a vertical deep carbonate well. The study used an inverse workflow to match the treatment pressure, determine fracture geometry, and match experimental fracture conductivity results with that simulated by the acid fracturing model.

This study shows that fracture conductivity can be optimized by taking advantage of the distribution of insoluble minerals along the fracture surface, and discusses the critical considerations to make the acid fracturing treatment successful. If the surface minerals are not properly accounted for as pillars, fracture conductivity at higher closure stresses might be severely under-predicted, leading to acid fracturing not being used even though it is a cost-effective simulation method.

DEDICATION

To my amazing wife, Amy Qiu;

and my children, Alina and Jaylen.

ACKNOWLEDGEMENTS

I want to express my sincere gratitude to both Dr. Zhu and Dr. A. Daniel Hill for their guidance during both my Masters of Science and Ph.D. graduate studies in Petroleum Engineering. Their expertise in nearly all aspects of well completions has allowed me to research some of the most important topics discussed by the industry today. Under their supervision and guidance, I have learned to take criticisms and turn those criticisms into my motivation to continuously improve my work, professionalism, and better understand how I can improve myself overall in the harsh and often relentless oil and gas industry.

I want to thank Dr. Hisham Nasr-El-Din for being one of my committee members and a good friend. His three classes: “well stimulation,” “formation damage remediation,” and “oilfield chemistry” was precious to me.

I want to thank Dr. Juan Carlos Laya for providing me the opportunity to learn about thin sections and gain a better understanding of how petrography and Scanning Electron Microscope can benefit my understanding of acid fracturing.

TABLE OF CONTENTS

Page

LIST OF FIGURES

Page

LIST OF TABLES

Page

1 INTRODUCTION

1.1 Background

Carbonate formations encompass more than half of the world's hydrocarbon reserves (Tansey, 2014). Large amounts of minerals that are dissolvable by hydrochloric acid (HCl) dominate these formations. These minerals mostly include calcite (CaCO3) and/or dolomite (CaMg(CO3)2). Acid stimulation is the preferred method to improve well performance due to these HCl-soluble minerals. Two stimulation methods have advantage in carbonate formations because of the existence of acid soluble minerals: acid fracturing and matrix acidizing.

Acid fracturing had been investigated extensively at the laboratory scale. However, acid fracturing experimental study is limited mainly to outcrop samples that are relatively homogenous rocks. In homogenous carbonate samples, fracture conductivity is created by uneven etching along the fracture surfaces. The variation of permeability on the fracture surface leads to the creation of conductivity. The experiments using homogenous rocks may not fully represent the conductivity created at downhole condition, when even a small percentage of insoluble minerals is included in the formation rock. Common acid-insoluble minerals in carbonate formations include but are not limited to various types of clay, quartz, pyrites, and anhydrite.

1.2 Literature Review

1.2.1 Significant Milestones in the Rise of Acid Fracturing Stimulation

The early time acidizing activities started back in the 1880s, while the first patent on acidizing was issued on March 17, 1896 (Frasch and Van Dyke, 1896). The patent described how the Standard Oil Company used hydrochloric acid (HCl) to stimulate a carbonate formation in Ohio. While this was the first recorded application of acidizing for well stimulation, it was not a successful one. Production soon declined, and acidizing was not started again until the 1920s. However, essential concepts were introduced in this patent that would eventually allow for the creation of acid fracturing.

The first documented acid fracturing was by Grebe and Stoesser (1935). While the initial treatment was designed to be below the formation parting pressure, during the treatment, pressures indicated that the formation was being fractured. Starting in the 1940s, research in proppant fracturing took over, and the advancement of acid fracturing research became limited. It was not until 1972 the next milestone was achieved in acid fracturing research when Nierode and Williams created their kinetic model for the reaction of hydrochloric acid with limestones. Soon after, a correlation was published by Nierode and Kruk (1973) based on experimental results using 1 in. by 2 in. core plugs that predicted the resultant fracture conductivity after acidizing. This led to a significant increase in the research work on acid fracturing treatment design using both experimental investigations and theoretical modeling work that continues today.

1.2.2 Early Experimental Investigations

A good amount of experimental work has been conducted over the past several decades to reduce uncertainty in acid fracturing performance. Barron et al. (1962) conducted experiments with Alabama Cream with a sawed fracture surface within a 1 in. diameter core holder; the total height of the sample was cut to less than 0.8 inches to allow for a maximum fracture width of 0.2 in. A wide range of acid flow rates and fracture width were tested, and the results were scaled up to create a correlation to predict the acid penetration length. Even though they were successful in the acid etching tests, fracture conductivity was not measured.

Broaddus et al. (1968) conducted acid etching tests using samples with disk-shaped fracture surfaces. The fracture conductivity was measured at 1000 psi of closure stress. Of the two formations where field data were available, the formation that responded better to acid fracturing stimulation also had much higher fracture conductivity in the experimental tests. They were able to use the experimental results to optimize their treatment design further.

Nierode and Kruk (1973) conducted acid etching with samples having a fracture surface of 1 in. diameter and a length of 2 in. The samples came from a wide range of formations (8 total), dominated by either limestone or dolomite. Their experimental setup allowed the measurement of fracture conductivity up to 7000 psi of closure stress. A universal correlation to predict the fracture conductivity based on the ideal width, closure stress, and the rock embedment strength was created based on the experimental results.

This correlation has been used extensively in the design of acid fracturing treatments utilizing any fracture geometry model.

Gong et al. (1999) successfully conducted 25 fracture conductivity experiments after acid injection. The samples used were Indiana limestone with a fracture surface of 2 in. wide by 2.5 in. long. The injection rate used ranged from 4 to 10 ml/min due to pump limitation. They concluded that there is a relationship between the fracture conductivity with the surface roughness and rock embedment strength. He found that the longer the acid contact time, the rougher the acid-etched surface, which would more likely result in higher fracture conductivity. However, a higher flow rate that would more likely resemble field conditions after upscaling was not used to create the acid-etched surface. The impact of higher flowrate on the acid-etched surface and its resultant fracture conductivity still needs to be investigated.

1.2.3 Surface Characterization

The first documented use of a surface profilometer to study surface topography before and after acidizing was by Ruffet et al. (1997). Since the profilometer is not automatic and a crank had to be used to move between each point manually, the amount of points measured is relatively limited. To maintain consistency between the location measured before made acidizing and after, the distance set between each measured point in the injection direction was at 0.4 in. This would allow an accurate calculation of dissolved volume on the fracture surface. An advanced surface profilometer was used by Nieto et al. (2006) to allow for the capture of the fracture surface topography before and after acidizing to determine the amount of rock removed from the fracture surface during acid injection. The profilometer

consists of a laser sensor and a servo table that automatically moves back and forth during scanning. The distance between each point of measurement along the sample is set to 0.01 in. Acid-etched patterns, including roughness, channeling, and uniform, could be clearly shown due to the 3D image created by interpreting the data from the profilometer.

1.2.4 Experimental Work Using the American Petroleum Institute (API) Modified Cell

Zou (2006) documented the design and testing of an advanced acid fracturing conductivity apparatus. This acid injection setup allows for an acid injection rate of 1 liter/min and the use of the American Petroleum Institute (API) conductivity cell for acid injection that will allow for samples with a larger fracture surface to be used. Samples used for the acid-etching test now have a fracture length of 7.25 in. and a width of 1.75 in. Differential pressure for leak-off can also be adjusted to create wormholes on the surface of the rock, mimicking what would likely happen in the field test. Lastly, an acid pump capable of pumping 1 liter/min was used for the experimental tests, which more closely resemble field rates than previous works. It was concluded based on the experimental work using the new acid injection apparatus that the treatment fluid, contact time, and wormholes created on the fracture surface all affect the fracture conductivity.

Given the availability of both the high injection rate acid injection apparatus and the profilometer, acid fracture conductivity, and the parameters that affect the conductivity behavior can now be properly studied. Melendez et al. (2007) conducted 15 sets of experiments, 5 with Indiana limestone, 5 with San Andres Dolomite, and 5 with Cream chalk at various contact time to observe the effect of contact time on fracture conductivity.

Rock embedment strength was also measured before and after acid after each experiment. They concluded that the channeling pattern dominates the fracture conductivity decline at increasing closure stress. When channels are not present, rock with higher strength after acidizing should result in better fracture conductivity behavior.

Most documented acid fracturing experiments have been conducted uses two sawed samples with flat fracture surfaces. Fracture surfaces created are in tension and not smooth in reality. While three types of etching patterns have been well documented, Neumann et al. (2012) believe that when the initial fracture surface is not smooth, a fourth pattern could be created by acid etching. This fourth pattern is the tensile etching pattern. In this pattern, peaks and valleys on the fracture surface are smoothed out during the acid injection process, and the resulting mismatch of the fracture surface generates fracture conductivity.

Almomen et al. (2014), conducted acid fracture conductivity experiments with dolomite samples. The result showed that samples initially broken in tension would produce a higher initial fracture conductivity than samples originally smooth. At low closure stress, the difference can be as significant as one magnitude of difference. However, as closure stress increase, the difference in fracture conductivity begins to decrease and eventually converge to similar fracture conductivity values.

1.2.5 Modeling of Acid Fracturing and Numerical Simulation

The objective of almost any acid fracture simulator is to estimate the approximate acid-etched width profile along the acid penetration length. This will require a prediction of the acid concentration as the acid travels along the fracture face. Terrill's (1965) heat

transfer analytical solutions for fluid flow between parallel porous plates. Terrill's solution was later used by William and Nierode (1972) to solve for the acid concentration along the fracture face and calculate acid penetration length and the acid-etched width. Ben-Naceur and Economides (1988), Lo and Dean (1989), and Settari (1993) all have also presented works that considered additional parameters including temperature effects, viscous fingering effects due to pumping of multiple viscosity fluids, leak-off behaviors, and the impact of the created fracture geometry during acid injection.

Settari's (2001) work also resulted in the introduction of a two-dimensional acid fracture model by solving the concentration along the fracture width. This led to the conclusion that one-dimensional models will likely underestimate the acid-etched-width profile. In that same year, a three-dimensional was introduced by Romero et al. (2001). In Romero's work, he assumed the height dimensional velocity profile was similar to that of the velocity along the fracture length. Mou et al. (2010) used numerical simulations and the Semi-Implicit Method for Pressure Linked Equations (SIMPLE) algorithms to solve for a velocity profile not limited to a three-dimensional non-uniform fracture shape between the fracture height and the fracture length. Even though the model accounts for all three dimensions, it was created as an intermediate-scaled acid fracture model. Mou's acid fracture model was modified by Oeth et al. (2014) to improve to field-scale size. This will allow a more realistically to simulate a field-sized treatment. However, Oeth et al.'s acid fracture model did not include a fracture propagation model or a heat transfer model. Without a fracture propagation model, external software was needed (Mfrac, FracPro, etc.) to simulate the fracture geometry and a method was needed to be able to transfer the

simulated fracture geometry into the three-dimensional model. Aljawad et al. (2016) used the Oeth acid fracturing model to study the selection of fluid systems based on formation permeability. Common with nearly all acid fracturing models, an empirical correlation to predict the acid fracturing conductivity is needed after simulating acid injection.

1.2.6 Empirical Correlations to Predict Acid Fracturing Conductivity

Acid fracturing simulators use correlations to calculate fracture conductivity. One of the most common correlations used is the Nierode-Kruk correlation (1973). However, the correlation had been shown to over-predict and under-predict fracture conductivity as shown by field measured acid fracture conductivities (Settari et al., 2001; Bale et al., 2010). This is due to the small core plugs used in the experimental tests which were used to derive the correlation.

Mou et al. (2010) developed a set of empirical correlations to calculate the fracture conductivity at zero closure stress as a function of permeability and mineralogy geostatistical parameters. The domain used by Mou was 10 ft. high by 10 ft. long, however, the gridbock used was 0.5 in. by 2 in (Mou et al., 2010). This will allow the dimensions of the domain to match that of an acid fracture simulator while its gridlocks resemble that of tests at the laboratory scale. The correlations are separated into three cases: 1) a permeability-distributed dominated case; 2) mineralogy-distribution dominated case; 3) competing effects of permeability- and mineralogy-distribution case. These cases all use three statistical parameters to describe the heterogeneity in permeability and mineralogy. These parameters include the vertical and horizontal correlation length and the dimensionless standard deviation. Utilizing the correlation

developed by Mou et al. (2010) for acid fracture conductivity, the model developed by Deng et al. (2012) allows the calculation of fracture conductivity at incremental closure stress. A methodology to obtain these parameters is described by Oeth et al. (2011).

While Mou-Deng's empirical correlation was based on intermediate scale simulations, its grid blocks are smaller than laboratory-scale experiments. The conductivity decline of calculated by the empirical correlation should adequately compare with the fracture conductivity decline seen in the laboratory experiments. The correlation will be used to match the fracture conductivity declines seen in these experiments.

1.3 Problem Description, Objectives, and Significance

Nearly all published results of acid fracturing experimental work are done with outcrop samples. These samples usually do not fully capture the heterogeneity of carbonate formations. The acid fracturing models developed today all require an empirical correlation to calculate the final fracture conductivity after simulating the acid-etched width. The Mou-Deng correlation permeability-distributed dominated case was benchmarked with the experimental results of outcrop Indiana limestones acid fracturing experiments with a wide range of surface profiles such as wormhole structures on the fracture surface and channels formed by the injection of viscosified acid. Using the benchmarked case, the mineralogy and the competing effect cases were created based on thousands of simulations.

This dissertation aims to use acid fracturing experimental results with downhole samples to benchmark the mineralogy related cases of the Mou-Deng model. The downhole samples contain minerals that commonly exist in nearly all carbonate

formations such as quartz, pyrite, anhydrite, and clay structures. The result of this work will include a modified Mou-Deng correlation for the mineralogy case, which will allow us to better use the acid fracturing models and the resulting fracture acid-etched-width to calculate the overall fracture conductivity.

1.4 Approach

1.4.1 Experimental Study

Experiments were run to measure the acid fracturing conductivity of downhole samples to study the impact of HCl-insoluble minerals on the fracture face on the overall fracture conductivity. The experimental results with downhole samples will be compared to outcrop Indiana limestone acid fracturing test results. These results will allow us to determine initial conductivity and fracture conductivity created by soluble minerals (calcite, dolomite) versus insoluble minerals (quartz, pyrite, clays, etc.).

1.4.2 Theoretical Work

Numerical simulations typically use an empirical model to calculate the final fracture conductivity. Currently, two correlations are commonly used; the Nierode-Kruk correlation and the Mou-Deng correlation. The Mou-Deng correlation will be calibrated to match the experimental results first. Then, the correlation will be used as a tool to calculate the fracture conductivity as part of a field-scale acid fracturing simulator.

1.5 Dissertation Outline

Chapter I gives the general background of this research by reviewing the literature and providing a problem for which this dissertation is trying to provide a solution. The

literature review will include both the experimental and simulation work relevant to acid fracturing in the past few decades.

Chapter 2 provides a detailed experimental procedure used for acid fracturing experiments using a modified API cell. This procedure will include new additions such as the x-ray diffraction testing, x-ray fluorescence testing, and tri-axial testing. These tests are all critical in acid fracturing experiments using downhole samples due to the sample fracture surface heterogeneity.

Chapter 3 looks at the experiments results of tests using both outcrops and downhole samples. The selected outcrop sample tested is Indiana limestone due to a high calcite content also expected in the downhole samples. Two sets of downhole samples were tested. One set was from a U.S. onshore location (Jin et al., 2019) and the other was from a Middle East formation (Naik et al., 2020). Fracture conductivity results as a function of closure stress were obtained for four Indiana limestone tests, five U.S. onshore downhole samples, and seven Middle East downhole samples.

Chapter 4 will use the experimental results of the U.S. onshore downhole samples to modify the Mou-Deng correlation mineralogy model. The Mou-Deng correlation uses both the calcite percentage and the Young's Modulus related to the downhole samples to calculate the fracture conductivity decline at increasing closure stress. X-ray diffraction (XRD) will be used to obtain the calcite percentages of the acid fracturing samples and the triaxial apparatus will be used to obtain a Young's Modulus range for the zone of interest.

Chapter 5 will discuss the application of a three-dimensional acid fracturing model for production history matching. The result of this study will be a matched production history of a deep carbonate formation vertical well. The modified Mou-Deng correlation from Chapter 4 will be used to calculate the final fracture conductivity and Aljawad's (2018) acid fracturing model will be used to simulate the acid etched-width needed by the correlation.

2 EXPERMENTAL DESIGN AND METHODOLOGY

This chapter presents testing samples information, experimental design, laboratory setup, material preparation procedure, and the new workflow designed to do a comprehensive study on acid fracturing experimental work using heterogeneous downhole samples.

2.1 Introduction

The acid fracturing experimental workflow had been documented thoroughly in the past decade.

The standard procedure is summarized in four steps:

1. Pre-acidizing surface scan and sample preparation for acid injection test
2. Acid injection test
3. Post-acidizing surface scan and sample preparation for a fracture conductivity test.
4. Fracture conductivity test

This procedure could adequately study the acid fracture conductivity of carbonate samples that mainly consist of calcite or dolomite. To study the conductivity behavior of downhole samples with acid-insoluble minerals that possibly act as pillars, holding the fracture open after acid injection, we modified the testing procedure.

2.2 Workflow and Procedure

The workflow and procedures used is shown in Figure **2-1**. The downhole rocks are cut into two different types of samples. The conductivity sets will be used for acid fracturing related experiments. The core plus will be used to measure the permeability of the rock

along the leak-off side and mechanical properties of the sample. The most important difference between this workflow and the traditional workflow (Guerra et al., 2018) is located in the three subsections describing x-ray diffraction (XRD), x-ray fluorescence (XRF), and measuring the Young's Modulus of the rock sample. The procedure of each step will be described in detail starting from inducing fracture in the fracture conductivity sets.

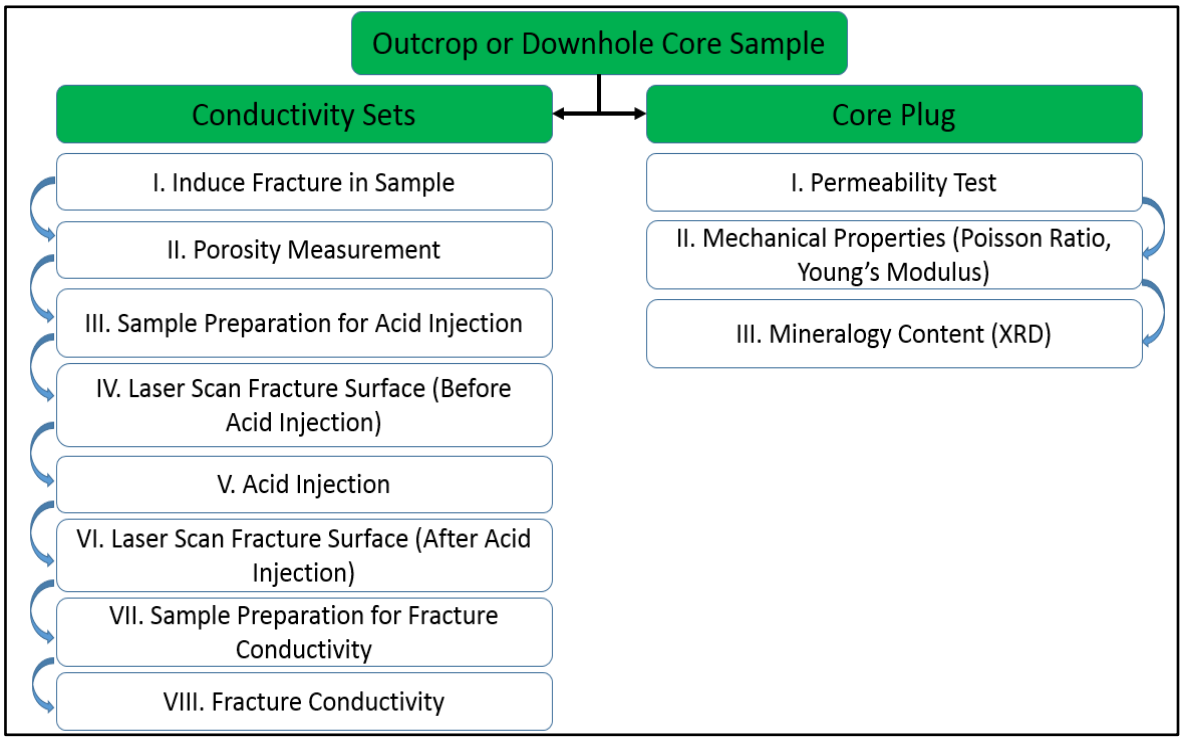

Figure 2-1: Modified flow chart of acid fracturing experimental study (Guerra et al., 2018).

2.2.1 Induce Fracture in Sample

1. Fracture the rock sample at the center either by sawing the sample (an even fracture) or by a tensile load (uneven fracture).

2. Cut the rock samples to dimensions of 7 in. in length and 1.61 in. in width.
3. Cut the sample in the height direction as close to 6 in. as possible.

2.2.2 Porosity Measurement Procedure

1. Dry both samples in the oven for several hours.
2. Measure the dry weight of the samples.
3. Saturate both samples at full vacuum pressure for at least 4 hours in vacuum pump (Figure **2-2**).

Figure 2-2: Vacuum pump used to saturate core samples.

4. Measure the wet weight of the samples.
5. Calculate the porosity using the difference in weight.

2.2.3 Sample Preparation for Acid Injection

1. Attach a sandstone spacer to the back of the carbonate rock sample if the sample is less than 6 inches in height.

2. Use blue tape to attach the sandstone spacer to the sample (Figure **2-3**).

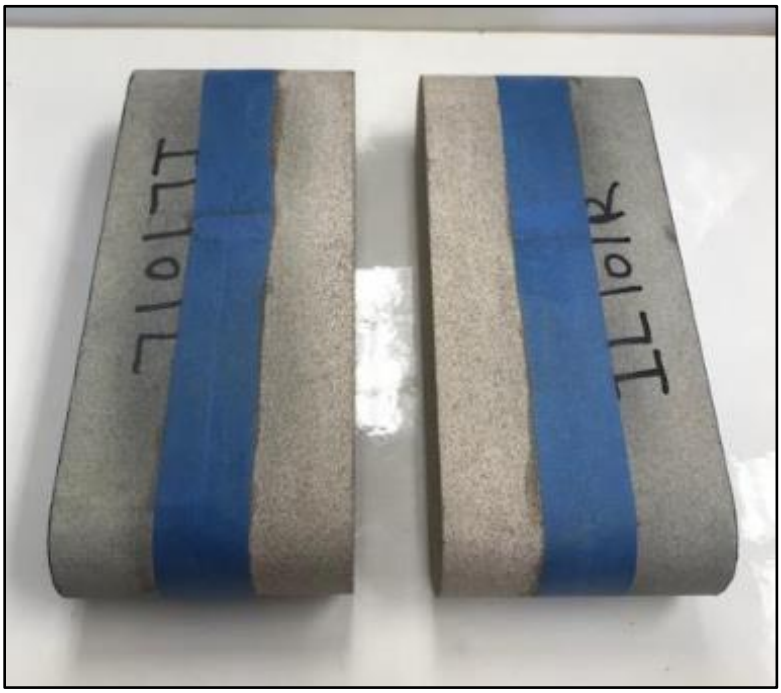

Figure 2-3: Samples less than 3 inches in height taped to spacers.

3. Use steel wool to rough the blue tape to improve the seal between the sandstone spacer and the rock sample.
4. Apply blue tape to the top and bottom area of the samples as shown in Figure **2-4**.

Figure 2-4: Additional tape applied to top and bottom of both samples.

5. Apply three layers of primer to the samples to increase adhesion between the rock and the RTV. After each application wait for 15 minutes.
6. Select the appropriate mold to make the sample (Figure **2-5**). The smaller mold used for acid injection is shown on the left. The mold include two sides, 3 side screws, a bottom base, and 4 bottom screws. The larger mold on the right is for making fracture conductivity samples in 1 step (this will be discussed later). The smaller mold can also be used to make fracture conductivity samples, but in two steps.

Figure 2-5: Left mold (Acidizing sample preparation) and right mold (Fracture conductivity sample preparation).

7. Clean the metal surface of the molds with cloth and acetone.
8. Apply three layers of silicone primer to the molds. After each application wait for 5 minutes.
9. Assemble the molds and screw on the four bottom and three side screws on each mold.
10. Place one sample in the molds and ensure that the sample is properly centered within the mold.
11. Prepare the RTV and pour into each mold carefully and slowly to ensure epoxy does not go on top of fracture surface.
12. Place the mold into the oven for 3 hours at 120 ^{o}F.
13. Extract the sample from the mold by removing the base first, then the sides. Use a screwdriver to chip the side so one side comes lose. The other side can then be

remove with a hydraulic press. The resulting mold should appear to be similar to Figure **2-6**. If there are breakage point on the side of the mold, red RTV can be applied evenly on the damaged area. The resulting sample dimensions should now by 7.25 in. in length, 1.75 in. in width, and 6 in. in height.

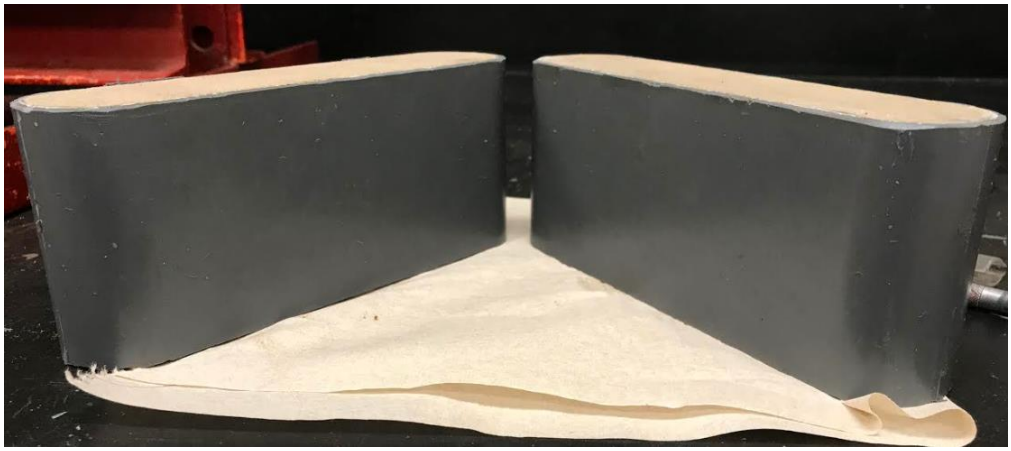

Figure 2-6: Acid fracturing samples with epoxy.

2.2.4 Fracture Surface Scan Pre-Acid Injection

The profilometer is used for two things: 1) to capture the acid-etched pattern after acid injection, and 2) determine the acid-`etched volume. The unique design of this profilometer allows for a high definition resolution of the scanned image. Each scanned point can be set to 0.05 in. apart without issues. This resolution will enable the measurement of 5,000 points before and after acidizing to create a volume difference surface scan. The surface scans will be used to explain the measured fracture conductivity in Chapter 3.

1. Place the sample on the servo table below the laser sensor (Figure **2-7**).
2. Mark the height of the laser as it can be moved up or down.

3. Open the vi. file.
4. Use the control box to move the servo-table to the origin of 0 in. on the x-axis and 0 in. on the y-axis.
5. Set the scan conditions to scan the appropriate length and width of the fracture face.
6. Set the resolution of the scanner to 0.05 in. between each point on the X and Y axis.
7. Start scanning by hitting the start button. Let the scanner finish by itself, premature shut-down of the scanner have been known to cause damage to the equipment.

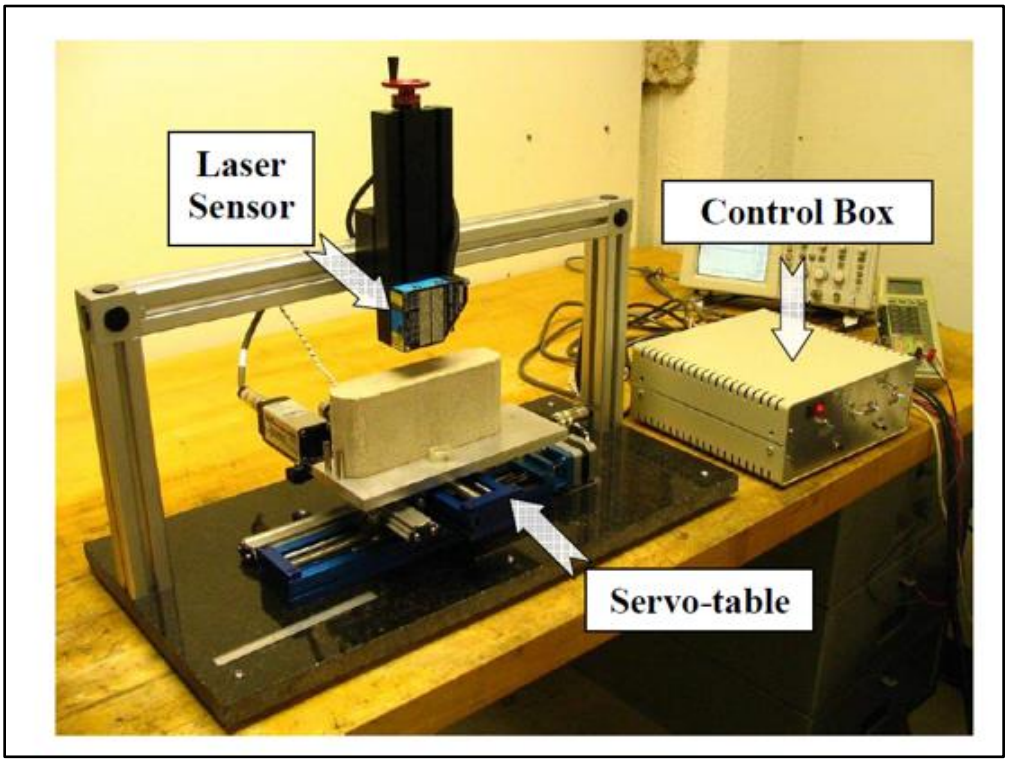

Figure 2-7: Surface laser profilometer.

2.2.5 X-Ray Florescence (XRF)

The x-ray florescence scanner (**Figure 2-8**) used for this study is located at the Texas A&M International Ocean Discovery Program (IODP) building. The equipment is designed for the scanning of surfaces ranging from a few inches (fracture conductivity samples) to greater than 10 feet long (samples recovered from ocean floor, etc).

Figure 2-8: XRF fracture surface scanner at IODP.

2.2.6 Acid Injection Preparation

The schematic of the acid injection apparatus is shown in Figure **2-9** (Jin et al., 2019). A pump capable of high injection rate is essential to the experiment. The high pressure pump in the figure can pump at a rate of 1 liter/minute. The procedure for the setup as well as the actual experiment is given in the following steps:

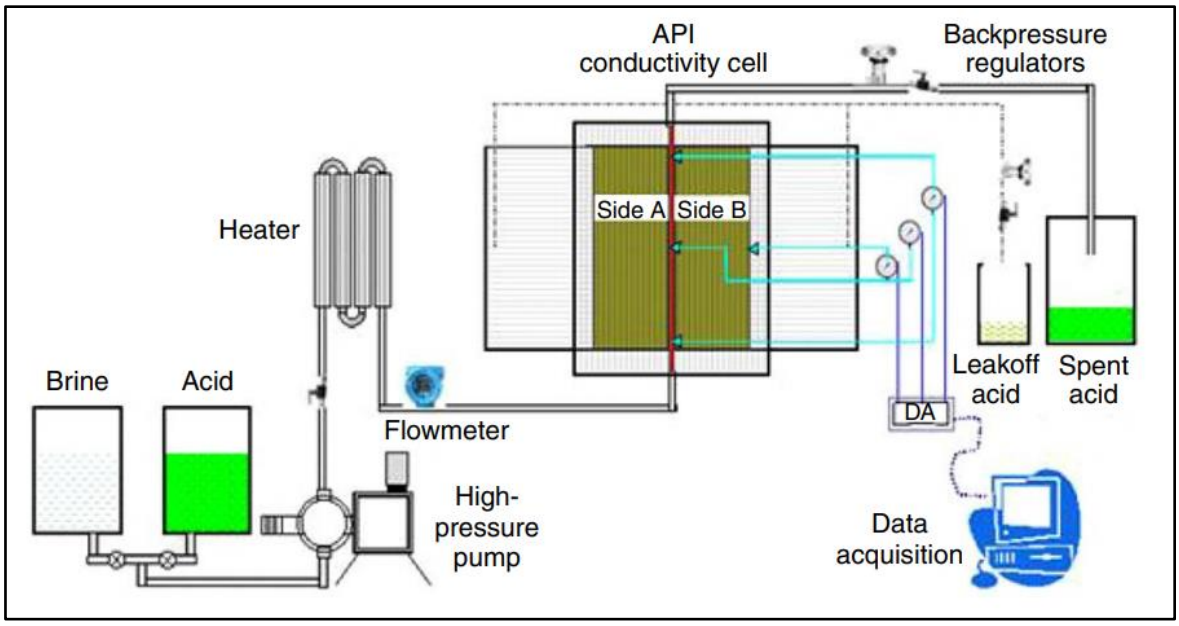

Figure 2-9: Experimental set up for acidizing (Reprinted from Jin et al., 2019).

1. Saturate the samples again at full vacuum pressure for 4 hours.
2. Insertion the two samples each with 7.25 in. in length and 1.75 in. in width after RTV is applied. Figure **2-10** shows the test cell and the cured core samples.

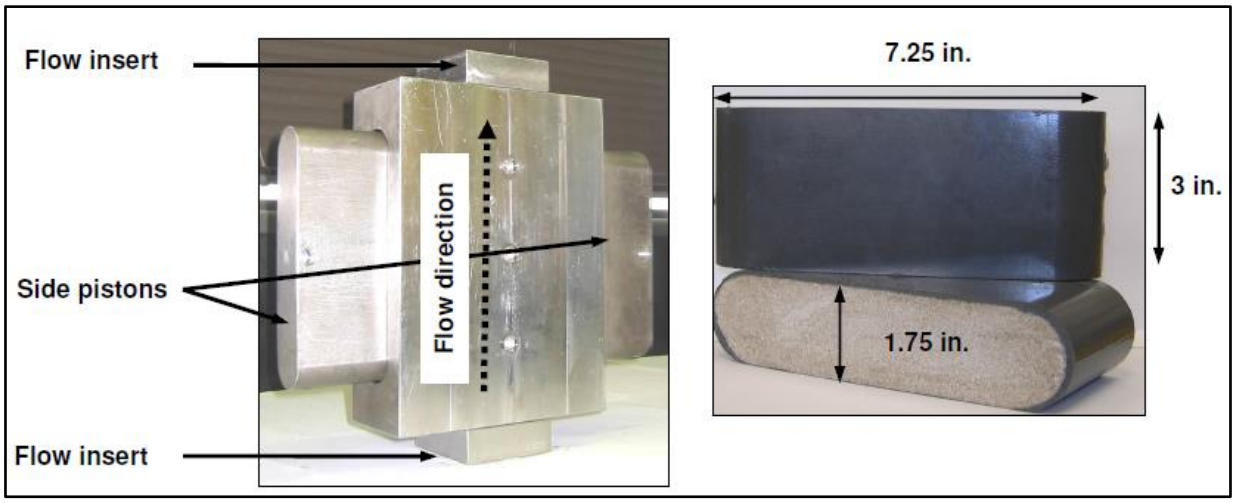

Figure 2-10: Test cell and core sample.

3. Apply grease along the RTV to assist the samples to slide into the cell, be careful to ensure grease does not touch fracture surface.
4. Insert one samples into the cell with a hydraulic press. Stop once the sample reaches the center of the cell. Figure **2-11** shows the hydraulic press and the inside of the cell after one core sample is placed inside the cell with the fracture surface up. It is very important that during the insertion of the sample that all 4 sides of the sample are checked to ensure it is centered. Failure to do so leads to breaking of the RTV and repeating the sample preparation stage
5. Release force exerted by hydraulic press.
6. Flip the cell and place a 0.15-0.2 in. shim along the surface of the sample inserted previously.
7. Insert the other sample until the sample's fracture surface touches the shim. Release force exerted by the hydraulic press.

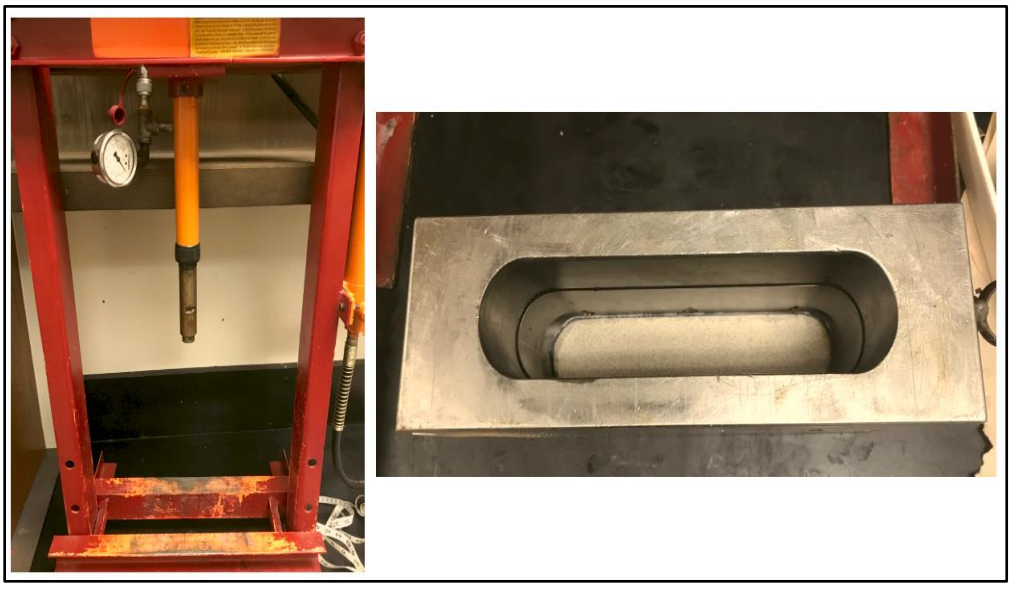

Figure 2-11: Hydraulic press and sample inside test cell.

8. Place the cell in the center of the acid injection apparatus, ensure the inlet is facing downwards and the outlet is facing upwards.
9. Fit the side pistons on the left and right side of the sell.
10. Connect all the fittings for all four sides of the cell.
11. Place the heating jacket on the test cell and turn on its controller. Set the controller to the desired temperature.
12. Turn on the controller for the heating tape. Figure **2-12** shows the heating tape and Figure **2-13** is the heating bathe.

Figure 2-12: Heating tape to increase fluid temperature.

Figure 2-13: Heating tub for higher temperature experiments.

2.2.7 Acid Injection

1. Fill the acid tank with the appropriate acid solution. Turn on the magnet stir to ensure the solution is well mixed.
2. Turn on the pump and set flow to 1 L/min.
3. Check for leaks in the apparatus by slowly increasing the cell pressure to 1000 psi. If any leaks in the connections are seen release cell pressure and fix leaks.
4. Pump desired volume of acid and switch to water injection. Allow water injection to run for 10 minutes or more. This is important to remove the acid in the system to protect the equipment.
5. Shutdown pump and disassemble the acidizing apparatus.
6. Use the hydraulic pump to remove the samples by pushing down with a buffer. Do not exceed 500 psi pressure during this step.

2.2.8 Fracture Surface Scan Post-Acid Injection

1. Repeat the steps in Section 2.2.4 with the now acidized fracture surface.
2. Use the Matlab code for the profilometer to interpret the results.
3. Calculate the volume of rock dissolved and produce the surface characterization images to interpret surface patterns.

2.2.9 Sample Preparation for Fracture Conductivity

1. Remove the RTV on the samples used for acidizing (Figure **2-14**).

Figure 2-14: Samples after removal of RTV.

2. Reapply blue tape to each of the two samples between the sample and spacer.
3. Rough the blue tape again with steel wool to ensure a tight seal.
4. Place one sample above the other along the fracture surface and apply additional blue tape the same way as the previous step. Use steel wool to ensure a tight seal.

5. Apply three layers of primer to the samples which increase adhesion between the rock and the RTV. After each application wait for 15 minutes.
6. Assemble the mold and place the sample in the center.
7. Prepare the RTV and pour into the mold carefully and slowly to ensure the RTV does not touch the fracture surface.
8. Put the mold into the oven for 3 hours at 120 ^{o}F.
9. Extract the sample from the mold and cut square openings of 0.5 in. by 0.5 in. to act as openings for the pressure transducer ports along the center of the sample (**Figure 2-15**). The openings are located at 0.9 in., 3.5 in., and 6.1 in. from left to right
10. Cut 0.5 by 0.5 in. sections along the two ends for the inlet and outlet for pressure measurements.

Figure 2-15: Fracture conductivity sample wrapped in epoxy.

2.2.10 Fracture Conductivity Test

The schematic of the fracture conductivity setup is Figure **2-16**. In this experiment nitrogen is injected and goes across the entire fracture surface. The differential pressure created during the flow is measured by two pressure transducers at the left and right side of the sample. The cell pressure is measured with the transducer in the middle. Fracture conductivity at each closure stress is calculated as a function of the differential pressure and the nitrogen injection rate. The setup and the experimental procedure is provided in the following steps:

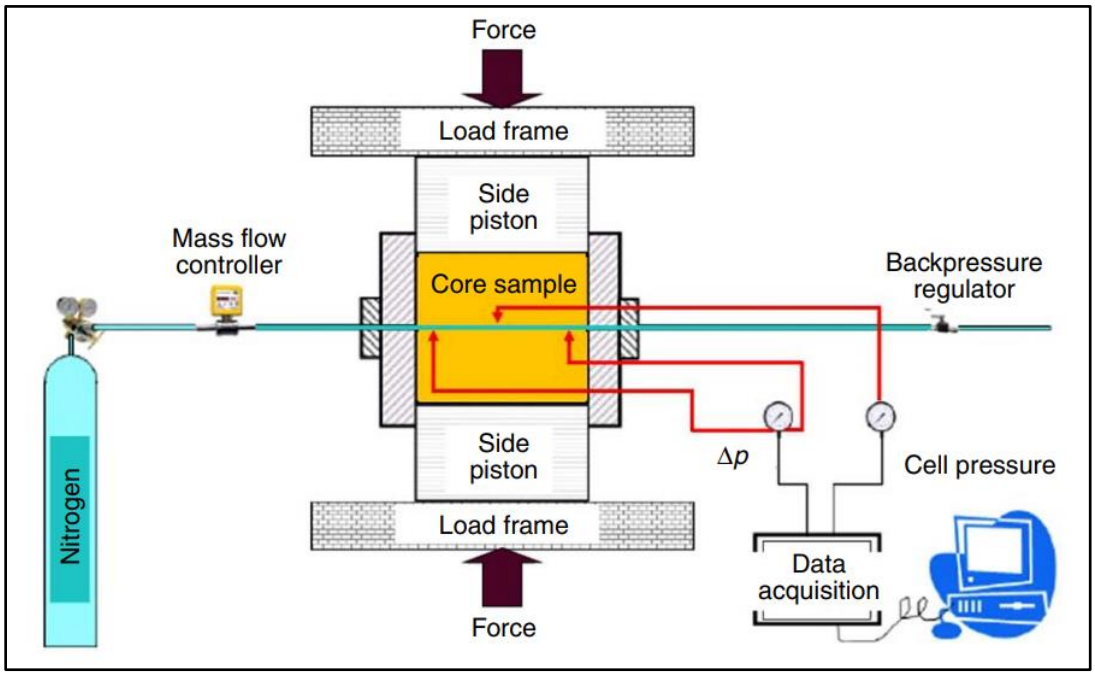

Figure 2-16: Conductivity test set up (Reprinted from Jin et al., 2019).

1. Wrap four single layer Teflon tape on the horizontal side and two double layer Teflon tape on the vertical side (**Figure 2-17**).

2. Apply enough grease to cover the entire sample and ensure the grease fully turns the Teflon tape yellow (left picture compared to right picture in **Figure 2-17**).
3. Insert the sample into the fracture conductivity cell without allowing the grease to get into the open sections previously cut for pressure measurements.

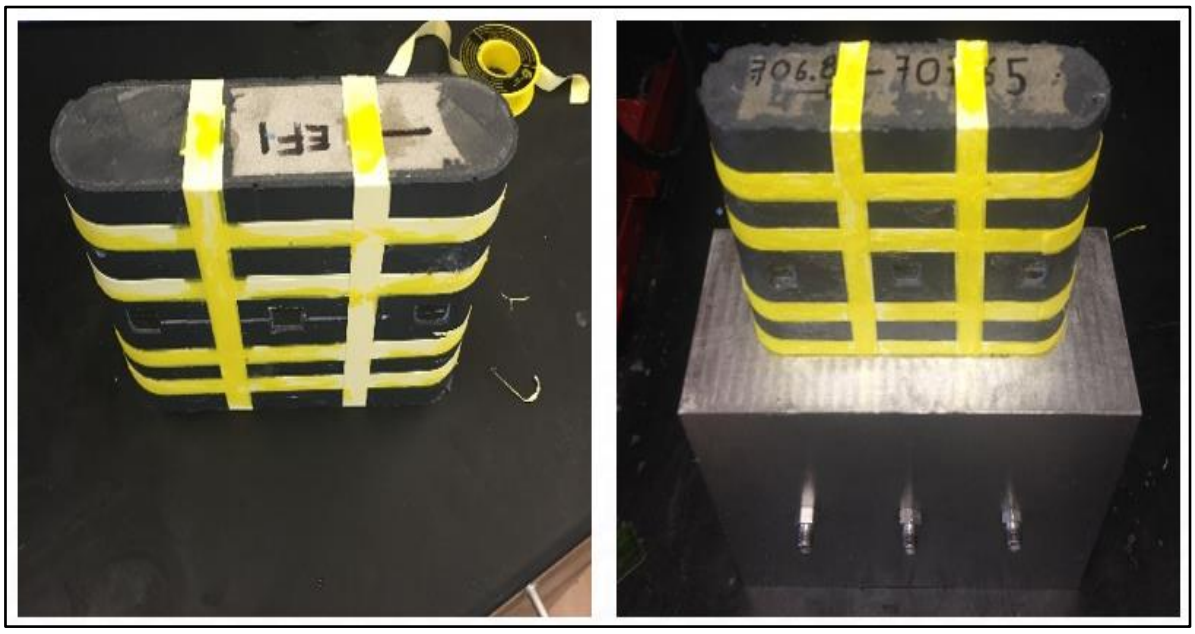

Figure 2-17: Preparing test sample for conductivity cell (Reprinted from Guerra et al., 2018)

4. Use a hydraulic press to insert the sample into the cell.
5. Place side pistons on the top, bottom of the conductivity cell, and then place everything below the load frame. Use a ruler to ensure all 4 sides are perfectly centered underneath the load frame.
6. Use the load frame controller to lower the load frame so it is touching the side piston.
7. Increase load to 500 psi.

8. Turn on the mass flow rate controller and wait until the displayed flow rate stabilizes.
9. Record the baseline flow rate.
10. Close the backpressure regulator located on the downstream side of the conductivity apparatus.
11. Open the nitrogen tank.
12. Use the spring valve to carefully allow a flow of nitrogen into the cell. This will increase the differential pressure as well as the flow rate. The flow meter is designed to measure a maximum of 10 L/min and the pressure transducer reads a maximum of 2 psi differential. Do not exceed either limitation.
13. Allow the differential pressure to rise above 1 psi so 4 measurements can be taken at each closure stress. After recording the first measurement of rate and differential pressure reduce the flow rate using the downstream back pressure regulator.
14. Wait for 15 minutes for the system to stabilize and measure new differential pressure.
15. Repeat this until 4 measurements are done at the 500 psi closure stress.
16. Calculate the resulting fracture conductivity.
17. Increase load by 500 psi and repeat steps 7-15. Do this until the desired closure stress is reached or fracture closure is observed.

2.2.11 Permeability Test

A small core plug is used to measure the permeability by doing coreflooding. Core holders are available for 1 in. to 1.5 in. in diameter core plugs. The equipment is shown in **Figure 2-18**. It is the same equipment used for standard matrix acidizing experiments.

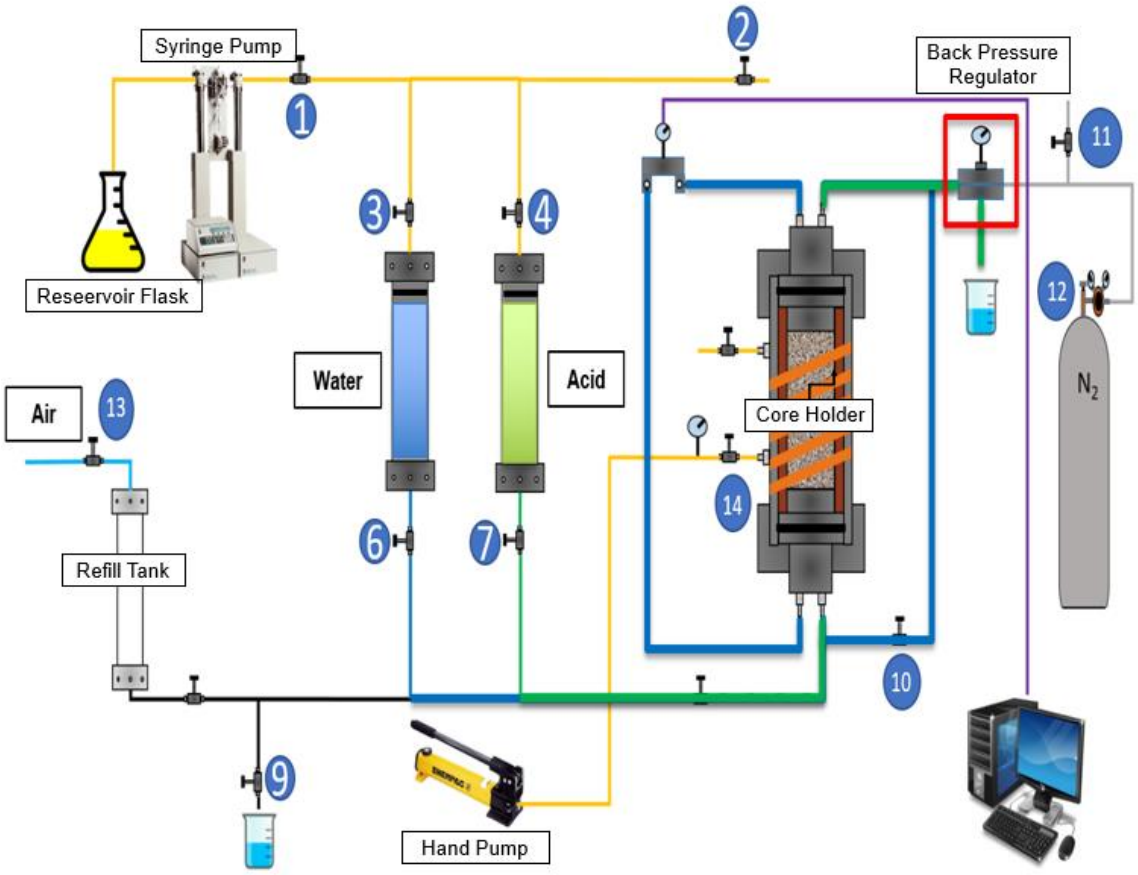

Figure 2-18: Coreflood equipment setup (Reprinted from Jin, 2013).

Important parts of a corefood apparatus include.

1) Injection pump
2) Core holder

3) Hydraulic accumulators
4) Overburden Pump
5) Backpressure regulator
6) Data acquisition system
7) Fluid heater

A detailed procedure of the permeability test can be found by Jin (2013).

2.2.12 X-Ray Diffraction (XRD)

The XRD equipment used is the D8 Advance Eco. A picture of the equipment is shown in Figure **2-19**. The sample is broken with a pestle and mortar. After grinding of around 30 minutes, the ground sample is put into the set of filtering sieves used for 100-mesh sand. The core material that does not go through the sieve is crushed again. This process is repeated until all the core material is filtered. The importance of ensuring all core material is filtered is because certain minerals are easier to grind than others. If a given sample is not fully grinded the XRD test may not show a true representation of the percentage of each type of mineral.

Figure 2-19: XRD testing apparatus.

The prepared powder was front-loaded into the standard specimen holder. The slit configuration consisted of a 0.3° divergence slit and 2.5° soller slits for the incident beam, and 2.5° soller slits for the diffracted beam. This arrangement provides a good combination of intensity, peak shapes, and angular resolution for the widest number of samples. Diffraction scans were made at conditions which run at 40 kV and 25 mA with an angular range of 4 to 70 °2θ (Cu), a step increment of 0.02 °2θ, and a count rate 2 seconds per step. Using an available database, the prominent diffraction peaks are used to calculate the mineralogy structure of the sample.

The result of a XRD test is shown in Figure **2-20**. The remaining core material after cutting a fracture conductivity set is grinded to make the XRD sample. The XRD

shows a mineralogy of 80.4% calcite, 16.27% anhydrite, 2.01% quartz, and 1.31% gypsum.

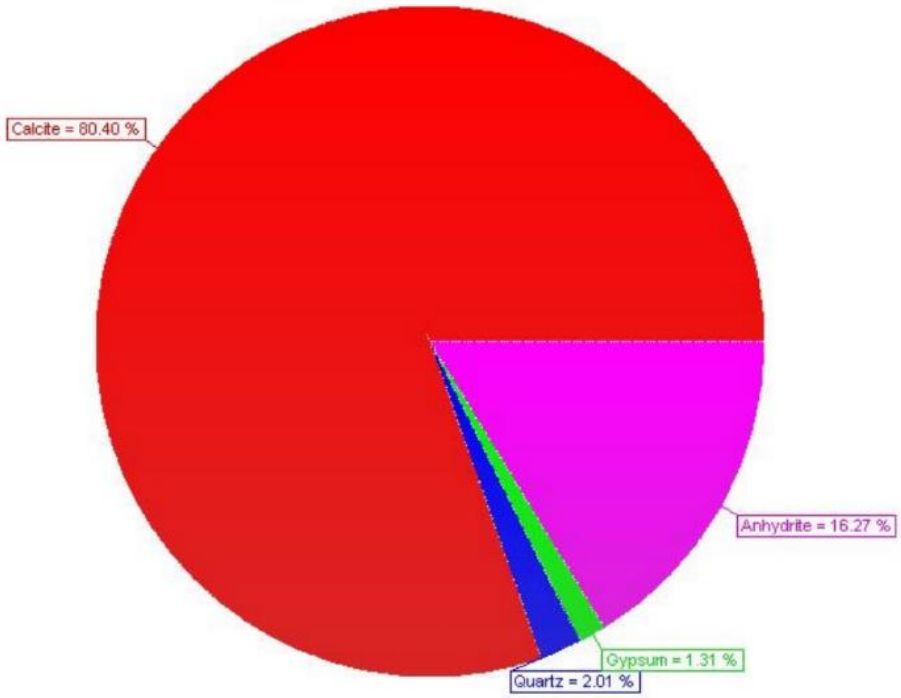

Figure 2-20: Example XRD result.

2.3 Chapter Summary

In this chapter, the workflow for the acid fracturing experiment is presented. Downhole samples are cut into both fracture conductivity samples and also core plugs. The fracture conductivity set samples go through acid injection, surface scan, and the fracture conductivity test. The core plugs undergo the coreflood test and the triaxial test. Finally, the trims after cutting both the fracture conductivity set and the core plugs are used for the XRD test.

Acid fracturing experimental test requires an arduous procedure. Due to the number of steps required and the different types of tests required for the test, it is recommended to understand the procedure before testing fully. Outcrop samples are always recommended for the tests until all the acid fracturing procedures can be completed successfully.

3 ACID FRACTURE CONDUCTIVITY EXPERIMENTAL STUDY*

3.1 Introduction

The objective of this experimental study is to determine if acid fracturing is a viable stimulation method for the Ratawi limestone formation. To accomplish this, three different types of limestone samples were used. The Ratawi limestone is very heterogeneous in its mineralogical make-up (calcite, dolomite, illite, kaolinite, quartz, pyrite as determined by XRD), which would make the rock a great candidate for an acid fracturing experimental study since most experimental work on acid fracturing uses rock samples made almost entirely of either calcite or dolomite.

The limited downhole core material of the Ratawi limestone was enough for only the fracture conductivity testing with very limited leftover rock pieces to make the samples for XRD. Downhole analog samples with similar complexity in mineralogical make-up were also provided. There was enough analog sample core material to also conduct mechanical properties and permeability testing in addition to the fracture conductivity and XRD tests.

Before testing downhole core material, Indiana limestone was used for baseline fracture conductivity tests. This limestone is made almost entirely of calcite (>99%) with only a trace amount of quartz as the HCl-insoluble mineral. There are several reasons to test the Indiana limestone samples first: 1) Several acid systems were

---

* Reprinted with permission from Jin, Xiao, Zhu, Ding, Hill, Alfred Daniel et al. 2019. Effects of Heterogeneity in Mineralogy Distribution on Acid-Fracturing Efficiency. *SPE Production & Operations* Preprint (Preprint): 14. https://doi.org/10.2118/194377-PA

selected, these acid systems can be evaluated first to reduce the selection, 2) acid fracturing experiments are complicated, fracture conductivity of these Indiana limestone tests should show comparable results to previously published papers , and 3) downhole samples are limited, Indiana limestone is always readily available.

In Table **3-1**, all 16 tests are summarized. Four tests were done with Indiana limestones (IL), 5 with analog limestone (AL), and 7 with the Ratawi limestone (RL). Three different acid systems were used, 15% HCl with straight acid, linear gelled acid loaded with 20% HCl, and viscoelastic surfactant (VES) acid loaded with 15% HCl. The linear gelled acid and the VES acid systems are combined together in a sequence injection for some of the tests (described later). Linear gelled acid is created by adding polymers to a HCl solution. The resulting polymer-acid mixtures are non-Newtonian fluids and are usually described by power-law rheological models (Gomaa et al., 2011). VES acid systems are a class of surfactants that create high viscosity when the strong acid is spent by reacting with carbonate minerals.

The porosity and permeability measurements show that Indiana limestone have better porosity and permeability than the two sets of downhole samples. A small amount of leak-off pressure (0.5 psi) was needed to create high densities of wormholes on the surface of the Indiana limestone samples (shown later) during acid injection. Due to the much lower permeability of the downhole samples, leak-off did not contribute significantly to wormholes forming on the surface of the rock and it was later on decided during the AL tests to cut leak-off pressure completely.

The tests done for each set of fracture conductivity set are also summarized in the table. Conductivity tests would also include acidizing the sample first. The testing condition for acid injection was at 140 ^{o}F. Acid was injected at a rate of 1 liter/minute with 20 minutes of contact time. Surface analysis would include measuring the surface before and after acidizing, and producing a surface image showing the volume of rock dissolved across the fracture surface. XRD and XRF were not done for all the tests. The decision to do XRF was not made until Test 7. This was due to the complexity of the fracture surfaces seen in the AL samples after acidizing. XRF would complement the XRD to explain the results of tests as needed.

Table 3-1: Summary of tests conducted in this study.

	Experiment No.	Acid Type	Porosity (%)	Permeability (md)	Tests Done
Indiana limestone (IL)	Test 1	Straight (15% HCl)	14	3	Conductivity, surface
	Test 2	Gel (20% HCl)	12	3	Conductivity, surface
	Test 3	VES (15% HCl)	12	3	Conductivity, surface
	Test 4	Sequence	13	3	Conductivity, surface
Analog limestone (AL)	Test 5	Straight (15% HCl)	5.1	0.023	Conductivity, surface, XRD
	Test 6	Straight (15% HCl)	2.03	0.001	Conductivity, surface, XRD
	Test 7	Straight (15% HCl)	1.68	0.001	Conductivity, surface, XRD, XRF
	Test 8	Sequence	7.76	0.0005	Conductivity, surface, XRD, XRF
	Test 9	Sequence	1.23	0.02	Conductivity, surface, XRD, XRF
Ratawi Limestone (RL)	Test 10	Straight (15% HCl)	1.58	-	Conductivity, surface, XRD, XRF
	Test 11	Sequence	7.91	-	Conductivity, surface, XRD

	Test 12	Sequence	5.87	-	Conductivity, surface, XRD, XRF
	Test 13	VES (15% HCl)	3.77	-	Conductivity, surface, XRD, XRF
	Test 14	Straight (15% HCl)	1.58	-	Conductivity, surface, XRD, XRF
	Test 15	VES (15% HCl)	2.69	-	Conductivity, surface, XRD
	Test 16	Sequence	2.53	-	Conductivity, surface, XRD

3.4 Acid Fracture Conductivity of Indiana Limestone

3.4.1 Acid Fracture Conductivity Test Results

The resulting fracture conductivity of Tests 1 to 4 is shown in Table **3-2**: Fracture conductivity results of Indiana limestone. The first fracture conductivity point is measured at 1,000 psi. The fracture conductivity is increased by 500 psi until reaching 6,000 psi of closure stress or if the fracture conductivity is no longer measurable due to the limit of the differential pressure transducer (calibrated to measure differential pressure up to 1 psi). The fracture conductivity results are plotted in Figure **3-1**. 15% HCl was used for Test 1 and resulted in much less initial fracture conductivity compared to Tests 2-4, which all used viscosified acid systems. Test 1 was terminated at 3,000 psi of course stress because the fracture conductivity was too low to measure (due to a large increase in pressure drop during nitrogen flow).

Table 3-2: Fracture conductivity results of Indiana limestone (Reprinted from Jin et al. 2019).

Closure Stress (psi)	Conductivity (md-ft)			
	1	2	3	4
1,000	890	5,656	13,676	3,017
1,500	396	1,823	6,141	2,303
2,000	196	1,089	2,184	1,462
2,500	106	800	898	1,428
3,000		738	616	904
3,500		291	482	367
4,000		193	355	190
4,500		132	173	54
5,000		86	81	50
5,500		59	52	42
6,000		40	30	31

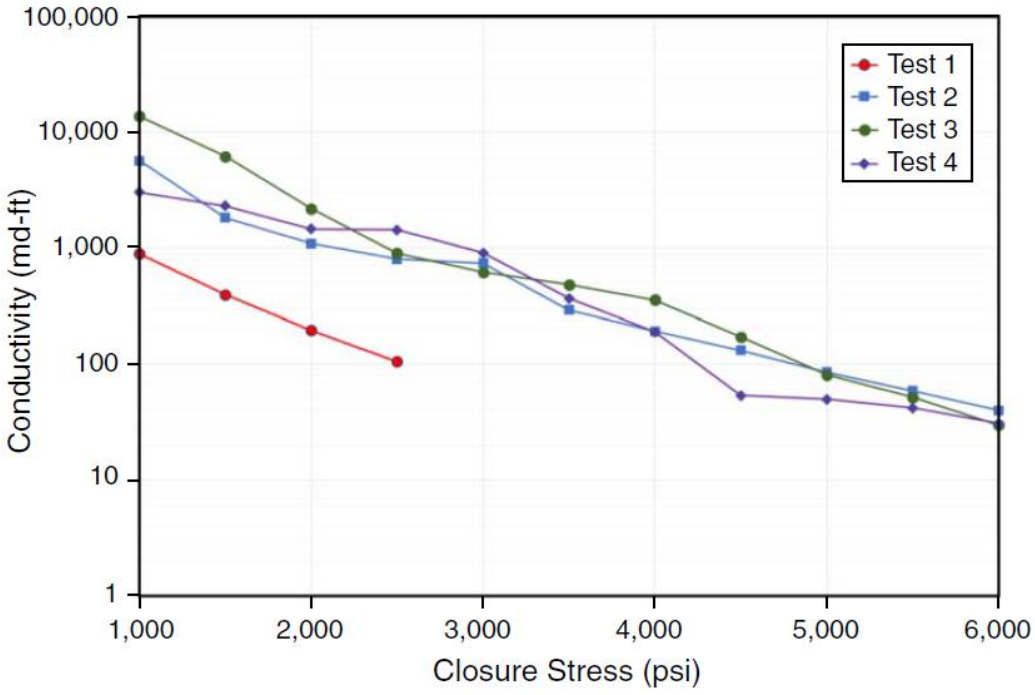

Figure 3-1: Fracture conductivity results of Indiana limestone tests (Reprinted from Jin et al. 2019).

Surface scans were carried out in each test to evaluate the etching pattern and total dissolved rock volume. Test 1 surface scan is shown in **Figure 3-2**. The acid is injected along the x-direction from left to right. The color bar shows how the color along the surface scan correlates with how much of the rock is dissolved at each measured point, in inches. An obvious entry effect was observed, and the rest of the fracture surface displayed a relatively uniform surface with minimal differential etching. This likely led to low overall fracture conductivity. Tests 2-4 all showed channeling patterns. The surface scan of Test 3 is shown as an example in Figure **3-3**. A deep channel resulted in the creation of higher initial fracture conductivity.

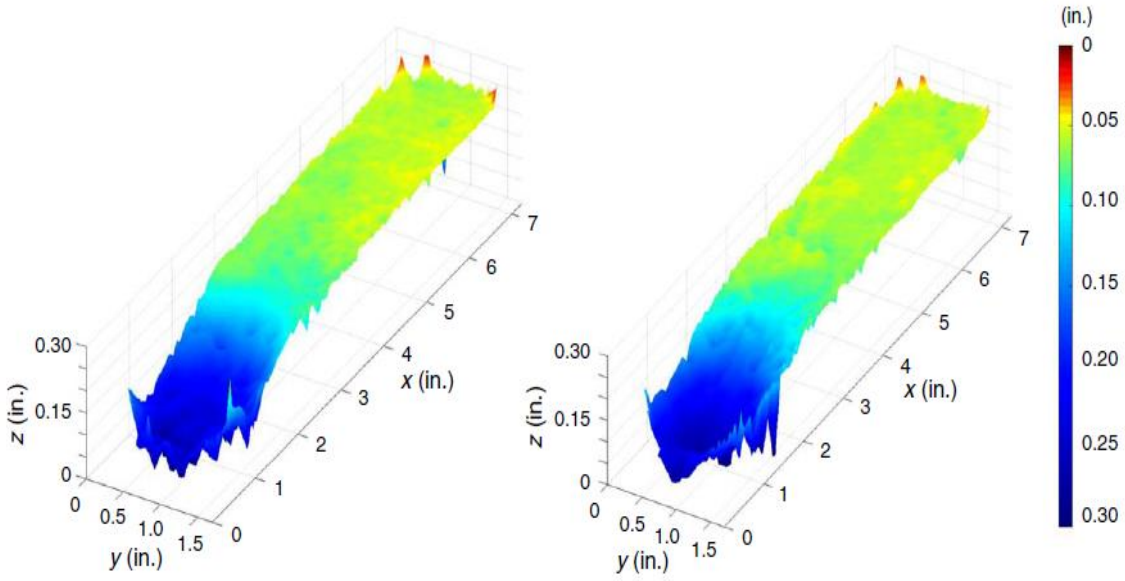

Figure 3-2: Test 1 surface scans showing a more uniform etching pattern.

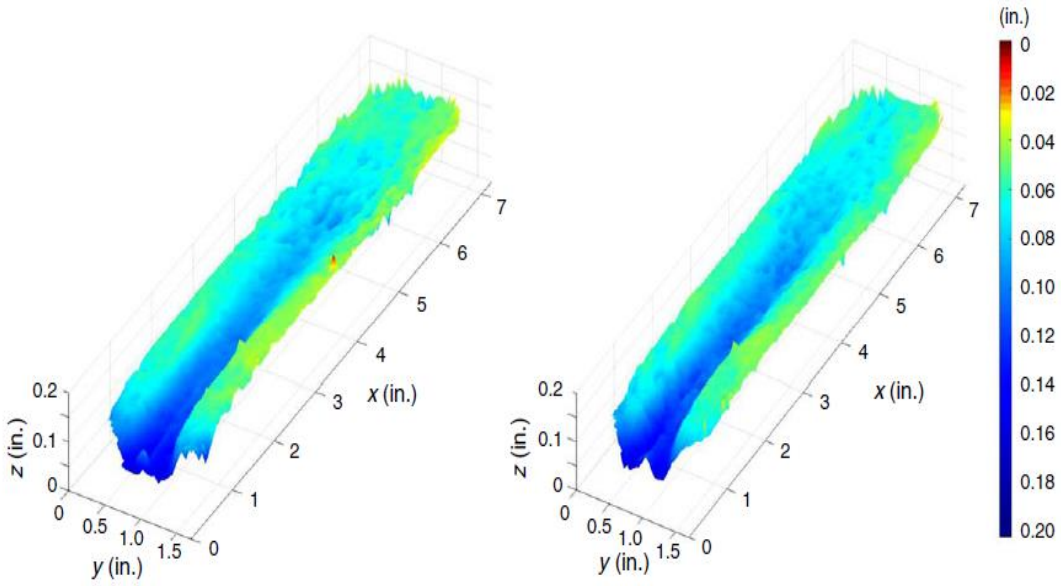

Figure 3-3: Test 3 surface scans showing a channeling pattern after acid injection

3.4.2 Comparison with Historical Indiana Limestone Tests

Test 1-4 were used as baselines for the four different acid combinations. Fracture conductivity was not measurable for Test 1 above 3000 psi of closure stress and reached very low values once the closure stress reached 6,000 psi for Tests 2-4. Previously published results using the same testing apparatus showed a larger database of Indiana limestone test results (Pournik et al., 2009). The summary of all the Indiana limestone tests are shown in Table **3-3**. Of these 12 tests, fracture conductivity was measurable only for seven of the tests at 5,000 psi of closure stress, the rest of the tests all had fracture completely closed as the closure pressure increased from 1000 to 5,000 psi. Closure stress of 6,000 psi was the highest closure stress that was tested in this set of studies. In these tests, the viscoelastic acid system also offered the highest initial fracture conductivity, similar to Test 3, which also used a type of VES.

Table 3-3: Summary of Indiana limestone properties and acid selection (Reprinted from Pournik et al., 2009).

				Fracture Conductivity (md-ft) vs. Closure Stress (psi)						
	Temp °F	Time (min.)		100	1,000	2,000	3,000	4,000	5,000	6,000
15 % HCl	175	5	Turbulence	14,354	8,375	4,607	1,010	172		
15 % HCl	175	10	Turbulence		26,056	14,037	12,696	5,476	174	112
15 % HCl	175	15	Turbulence		1,367	1,244	807	401	139	74
15% HCl	175	20	Turbulence	2,069	236	19				
Gelled	175	5	Roughness	18,711	8,696	4,890	5,180	103		
Gelled	175	10	Roughness		2,987		119	6		
Gelled	175	15	Roughness	14,579	3,187	208	69	125	25	
Gelled	175	20	Roughness	1,994	1,208	523	266	191	55	
Gelled	175	30	Roughness	4,314	48	38	31	15		
Viscoelastic	200	15	Channeling		16,838	12,991	10,189	7,179	1,903	38
Viscoelastic	200	30	Channeling		34,273	10,606	1,633	189	100	
Viscoelastic	200	60	Uniform		36,500	1,910	461	127	104	20

3.4.2 XRD Test Result of Indiana Limestone

XRD was done on the same rock sample that was used to create samples for the conductivity tests of Tests 1-4. The sample had 99.37% calcite and 0.63% quartz. For all acid used, the fracture conductivity is mainly provided by non-uniform itching of calcite, which leads to a high decline of fracture conductivity.

3.4.3 Creation of Wormholes on Fracture Surface

As pressure differential was applied to the leak-off line, Tests 1-4 all had wormholes on the fracture surface. Figure **3-4** shows the randomly distributed wormholes on the fracture surface.

Figure 3-4: Test 1 (left) and Test 3 (right) fracture surfaces after acidizing.

Thin sections were created from the surface of an Indiana limestone conductivity sample that was not acidized (Figure **3-5**). The polished thin sections are colored with a fluorescent spike to showing porosity. Areas with no blue spike have no porosity, and likely no permeability. The thin section was put under a petrographic microscope. A zoomed-in section of the thin section is shown in Figure **3-6** with a scale bar in millimeters. When a differential pressure is applied, and the injected acid flows into the sample perpendicular to the flow direction, the acid could only travel to areas shown in blue as some permeability typically exists in regions with porosity. This picture explains why the wormholes appear randomly in Figure **3-4**.

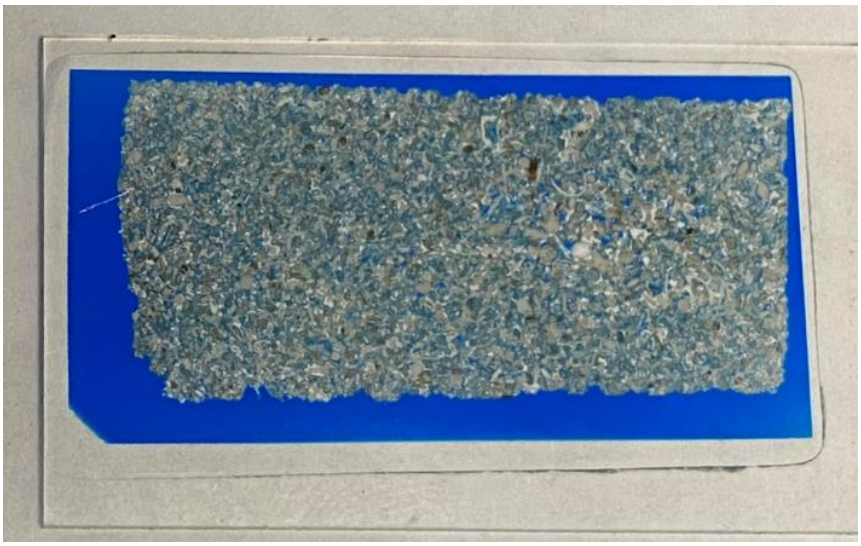

Figure 3-5: Thin section sample from Indianalimestone

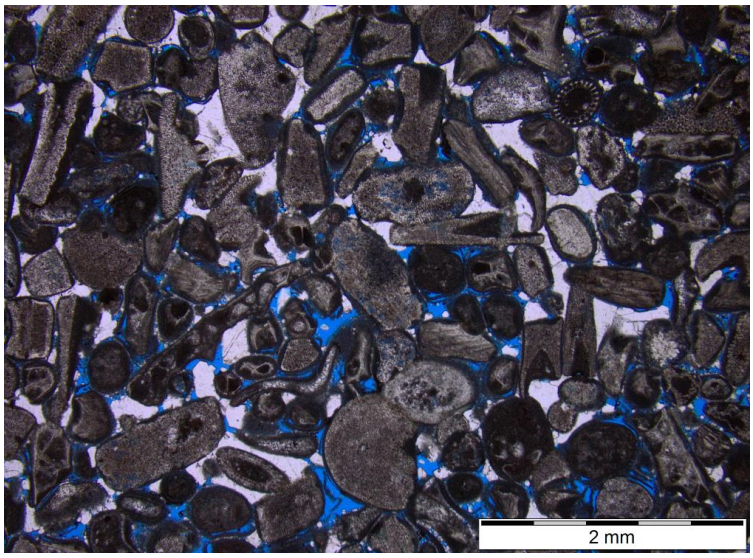

Figure 3-6: Thin section petrography picture showing blue areas to be areas with porosity.

3.4.5 Type of Calcite

To determine the content and impact of magnesium, a scanning electron microscope (SEM) was used to study the thin sections discussed in Section 3.4.4. The SEM image was selected with both calcite and quartz. The image is approximately 120. The elemental tables in both Figure **3-7** and Figure **3-8** correspond to the area marked by a red circle. In both tables, no magnesium (Mg) was detected. In Figure **3-7**, the SEM showed almost entirely calcite (CaCO3) with a trace amount of quartz (SiO2). In Figure **3-8**, quartz is the dominant mineral.

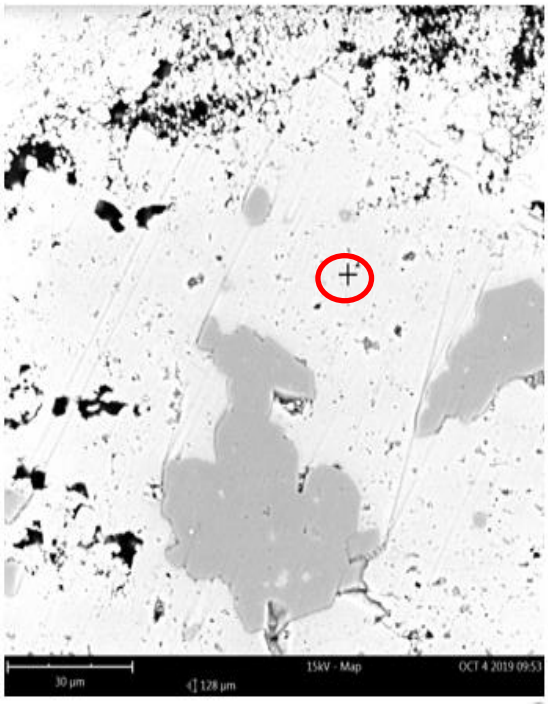

Element Number	Element Symbol	Element Name	Atomic Conc.	Weight Conc.
8	O	Oxygen	56.19	45.89
6	C	Carbon	24.32	14.91
20	Ca	Calcium	18.52	37.90
14	Si	Silicon	0.51	0.73

Figure 3-7: SEM white area dominated by calcite.

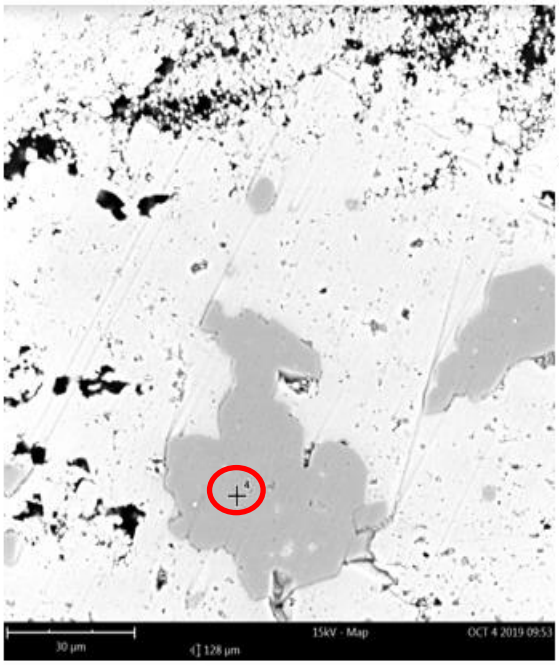

Element Number	Element Symbol	Element Name	Atomic Conc.	Weight Conc.
8	O	Oxygen	72.70	58.90
14	Si	Silicon	23.67	33.66
20	Ca	Calcium	3.51	7.12

Figure 3-8: SEM grey area dominated by quartz.

3.5 Acid Fracturing Conductivity for Analog Limestone Downhole Samples

Downhole limestone formations typically have a more complicated mineralogy composition than that of Indiana limestone. While Indiana limestone outcrop samples could offer a qualitative study comparing variations in design parameters such as acid selection, it does not represent the expected acid fracturing conductivity of the Ratawi limestone formation, which is the target of interest of this study.

As mentioned in the introduction, the analog samples are analogs to the Ratawi limestone located in the middle east. The analog samples are of particular interest because of the consistent calcite percentage of 80 to 85%, allowing the tests to be used as baseline tests for the even more mineralogically complicated formations of the Ratawi limestone. Saudi Arabian Chevron provided both analog samples and the Ratawi limestone samples

to study how increased mineral heterogeneity in limestone formations could affect overall fracture conductivity (Naik et al., 2020). The result of these sets of tests on the downhole samples ultimately decides if acid fracturing is a viable stimulation method for the Ratawi limestone.

These analog samples used in this study have an average permeability of 0.01 mD and an average porosity of 3.6%. For heterogeneous cores, both acid system and rock mineralogy affect the conductivity. To identify the cause of conductivity behavior, the mineralogy of the test samples was measured first. Then with the conductivity test results, the mineralogy distribution was used to explain the etching patterns observed.

3.5.1 X-Ray Diffraction Analysis (XRD)

XRD results are discussed first because for downhole samples, the mineralogy is more complex and plays a critical role in creating fracture conductivity. Test 5 to 9 from Table **3-2** are the analog samples. The XRD results for these tests are shown in Table **3-4**. The results of the XD show a fairly consistent calcite percentage among all samples of 80-85%. It shows a relatively high percentage of insoluble minerals in these heterogeneous samples, ranging from 5-15%. Test 5 and 6 samples also contain a higher percentage of dolomite. The dominating HCl-insoluble mineral for Test 5, 7, and 9 is quartz, and for Test 8, it is anhydrite. Test 6 sample contains the highest overall percentage of HCl-insoluble minerals. For this particular rock type, the insoluble minerals can reduce the dissolved volume from the acid injection but have higher rock mechanical strength than the carbonate components, and may provide more sustainable conductivity under closure stress.

Table 3-4: XRD results for Tests 5-9 (Reprinted from Jin et al., 2019).

Minerals	Test 5	Test 6	Test 7	Test 8	Test 9
Calcite	80.40	84.27	84.59	80.40	83.75
Dolomite	8.36	9.38	0.39	0	0.99
Feldspar	1.41	0.00	0	0	0
Gypsum	0.82	1.27	0.36	1.31	0
Illite	3.62	2.36	3.57	0.00	4.97
Quartz	5.38	2.84	11.08	2.01	8.98
Kaolinite	0	0	0	0	0.99
Anhydrite	0	0	0	16.27	0.49
Total	100	100	100	100	100

3.5.2 Acid Fracturing Conductivity Results

Of the 5 tests conducted, three of them (Tests 5, 6, and 7) used straight 15% HCl, and two of them (Tests 8 and 9) used alternating injection of linear gel – VES – linear gel. Test 5 and 6 had a leak-off differential pressure of 4 psi to allow leak-off from the cell. Tests 7 – 9 had the leak-off line closed. The conductivity results for the five downhole core tests are listed in Table **3-5** and plotted in Figure **3-9**. The downhole cores withstand higher closure stress. Except Test 9, all tests had measurable conductivity up to 8,000 psi of closure stress. The fracture conductivity was unmeasurable at 7,000 psi for Test 9. The sample for Test 8 failed partially toward the outlet where the anhydrite was located. It is possible that the rearrangement of broken pieces of the rock sample during the nitrogen injection made the fracture conductivity increase when the closure pressure increased to 2,000 psi. Recall that for the Indiana limestone tests, none of the tests had measurable fracture conductivity above 6,000 psi of closure stress.

Table 3-5: Fracture conductivity results for tests 5-9 (Reprinted from Jin et al., 2019).

Closure Stress (Psi)	Conductivity (md-ft)				
	5	6	7	8	9
1000	1234	1092	1148	470	211
1500	536	473	914	600	110
2000	288	284	727	1167	86
2500	235	226	622	620	59
3000	247	207	488	409	46
3500	231	201	433	333	46
4000	254	203	351	330	40
4500	242	169	322	329	38
5000	247	173	210	227	35
5500	224	135	176	152	30
6000	209	139	123	145	32
7000	164	121	81	115	-
8000	125	106	62	66	-

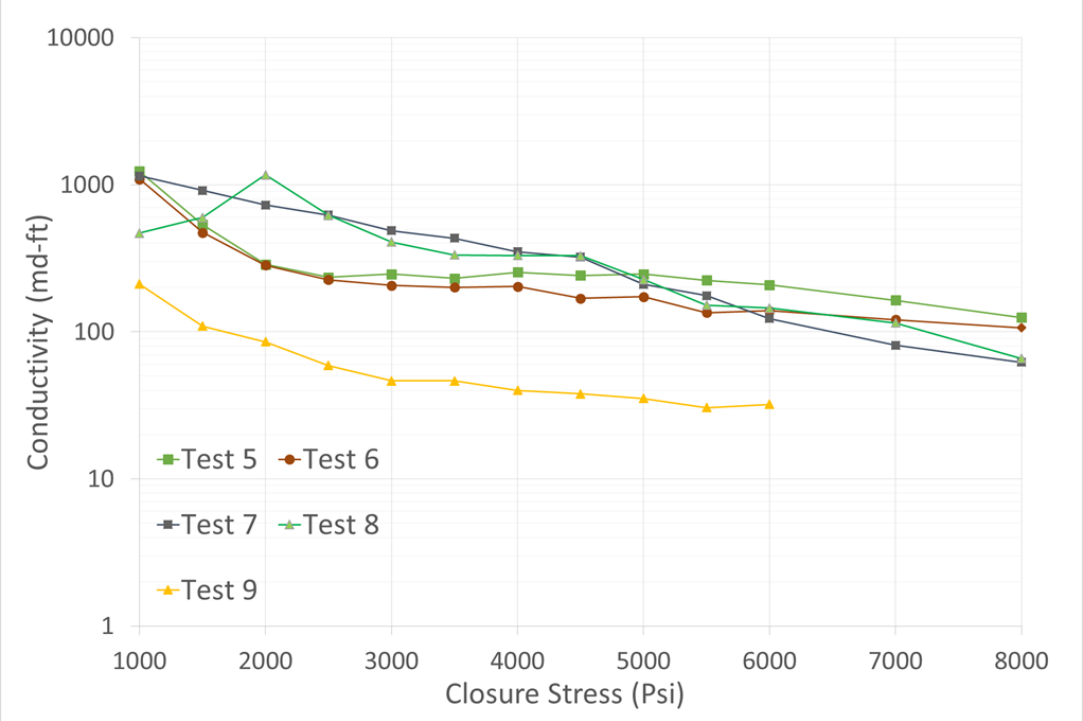

Figure 3-9: Fracture conductivity results comparing Tests 5-9 (Reprinted from Jin et al., 2019)

3.5.3 Impact of Acid-Etched Volume on Acid Fracturing Efficiency

As mentioned before, for heterogeneous cores, the mineralogy of the core affects the conductivity in two ways: less dissolved volume because of the insoluble minerals, and more sustained conductivity because of the higher content of harder minerals. The volume of rock dissolved by acid injection is listed in Table **3-6**. The dissolved volumes were obtained using the surface scans. As expected, Test 6 sample yielded the highest dissolved volume as a result of being the rock sample with the highest dissolvable mineral content. The low dissolved volumes for Tests 8 and 9 are attributed to both higher content of the insoluble minerals in those test samples, and more so, to the slower-reacting, viscosified acids used in the tests

In addition to the content of insoluble minerals, the low initial conductivity in Tests 8 and 9 is also related to the lower dissolved volume after acid injection. These two tests were conducted with gelled acid and VES in three injection steps. This injection procedure is used to prevent excess leak-off and promote etched fracture length. This study showed that for heterogeneous formations, lower acid fracture efficiency is possible because of the combination of insoluble minerals when acids with lower reaction rates are used. The dissolved volume determines the initial fracture conductivity. If viscosified acid systems are considered initial to limit fluid leak-off, the type of viscosified system need to be selected more carefully in heterogeneous formations to avoid low acid-etched volume on the fracture surface.

Table 3-6: Acid-Etched Volumes

Test #	Acid System	Etched Volume (in^3)
5	15% HCl	1.65
6	15% HCl	2.30
7	15% HCl	0.77
8	Gel, VES, Gel	0.42
9	Gel, VES, Gel	0.24

3.5.4 Impact of Mineral Distribution on Acid Fracturing Efficiency

An interesting observation of this study is the effect of mineralogy distribution on the fracture face. The mineralogy distribution can be described by correlation length. If correlation length is longer in the flow direction compared with the other dimension on the fracture surface, most likely channels or dissolved streaks will be developed after acid injection (Mou et al., 2009). During acid injection, the dissolvable minerals react with acid, exposing the insoluble mineral to the fracture surface to support the fracture open under closure stress. The distribution of insoluble minerals plays a vital role in fracture conductivity behavior. To study this effect, we examine the etching pattern for the five heterogeneous samples.

Due to the orientation of the provided cores, the testing samples were all cut with the insoluble mineral streaks perpendicular to the flow direction. Figure 3-10 to Figure

3-14 display the scanned surfaces of Test 5 to 9 after acidizing. Warmer colors indicate the high points/area along the surface and the locations of the HCl-insoluble minerals. Clear patterns of streaks across the fracture surfaces perpendicular to the flow direction were observed in Tests 5, 6, 7, and 9. One sample that did not show streaks (Test 8) had the same level of conductivity even with the slower-spending acid sequence. The combination of low acid-etched volumes and insoluble mineral streaks perpendicular to flow made Test 9 the worst-case scenario of all tests.

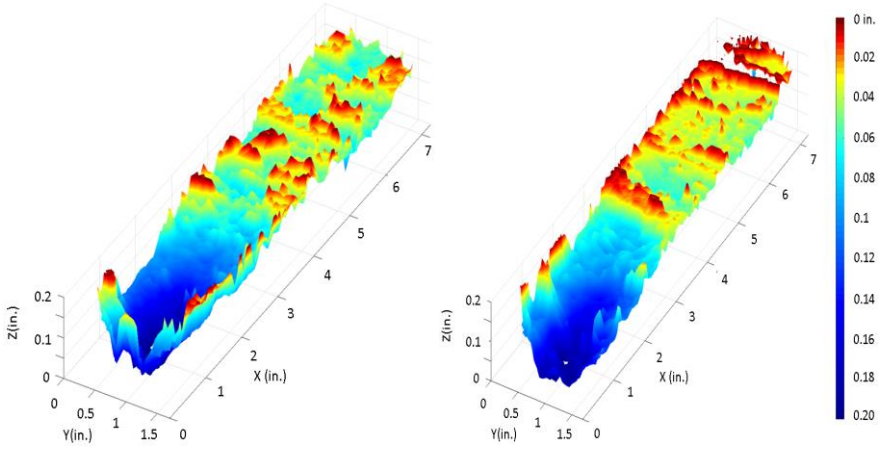

Figure 3-10: Test 5 after acidizing surface scans.

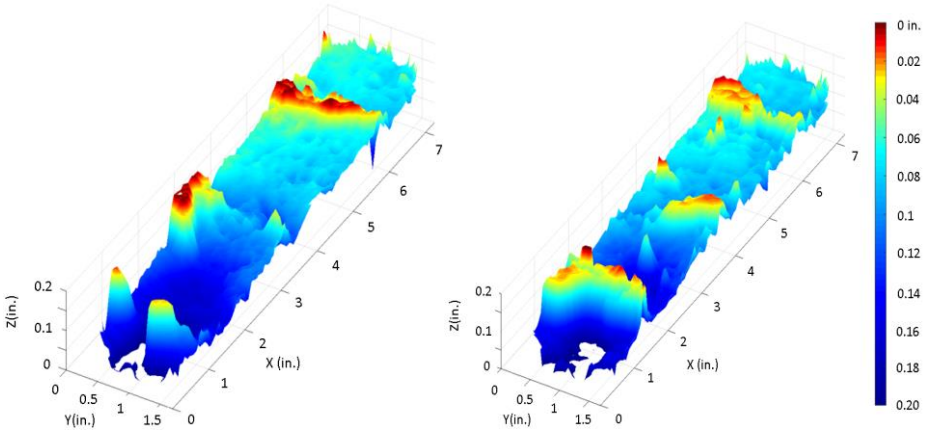

Figure 3-11: Test 6 after acidizing surface scans.

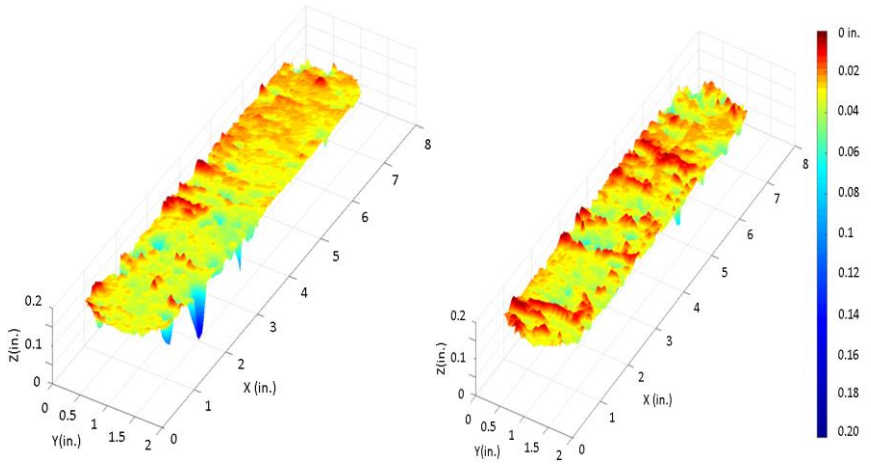

Figure 3-12: Test 7 after acidizing surface scans.

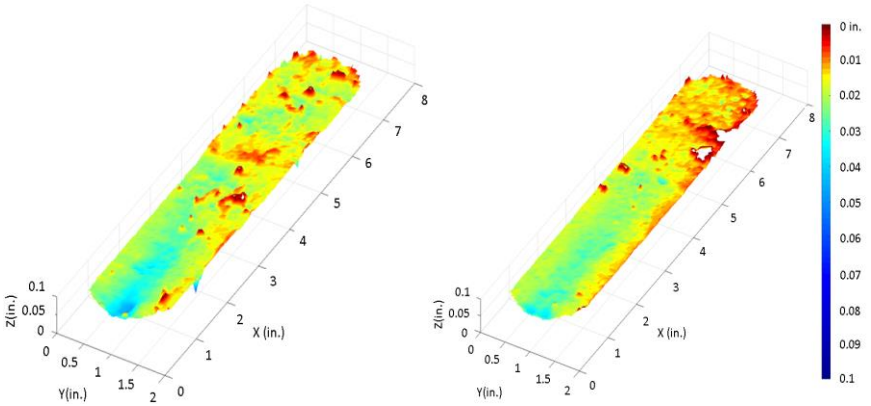

Figure 3-13: Test 8 after acidizing surface scans.

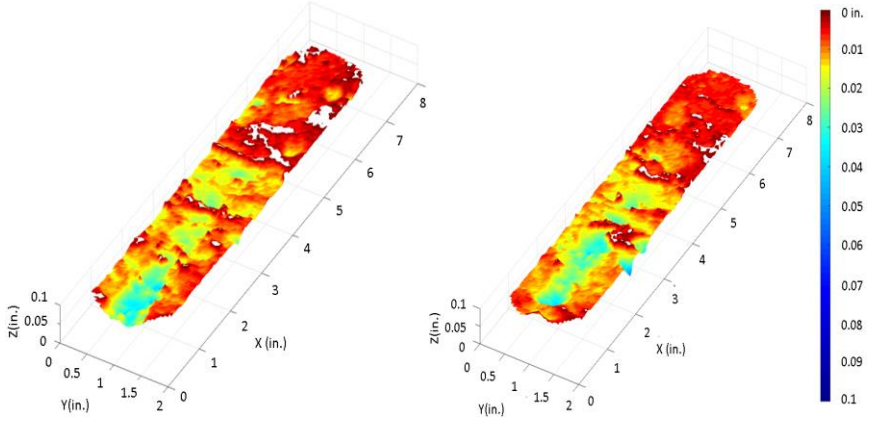

Figure 3-14**:** Test 9 after acidizing surface scans.

In the field, if the mineralogy correlation orientation can be determined, and if the stress orientation allows, completion and fracture design can be optimized to align with the mineralogy correlation direction. Successful alignment can enhance acid fracture channeling patterns to improve fracture conductivity.

The insoluble minerals in the sample have higher mechanical properties than the calcite. Figure **3-15** shows the scanned fracture surface before (Figure **3-15**a) and after the conductivity test (Figure **3-15**b) for Test 5. The closure stress increased to 8000 psi during the conductivity test. The insoluble minerals (the locations of the red-colored area) supported the fracture opening under high closure stress. This is clearly evidenced in Figure **3-16**, which plots the conductivity results for Test 1-9. Recall that Tests 1-4 are the homogenous Indiana Limestone cores, and Test 5-9 are the downhole heterogeneous cores. The two dotted lines show the trend of conductivity decline of the two sets of rocks. The heterogeneous cores have lower initial conductivity, but slower decline rate, compared with the homogeneous Indiana limestone. The behavior of low initial and low decline rate are both mainly because of the insoluble minerals in the core samples, which makes the heterogeneous rock a better candidate for acid fracturing. At higher closure stress, the heterogeneous cores kept higher conductivity compared with the Indiana Limestone, which matters more than the initial value of conductivity. The only exception is Test 9, which was the case with the lowest acid-etched volume.

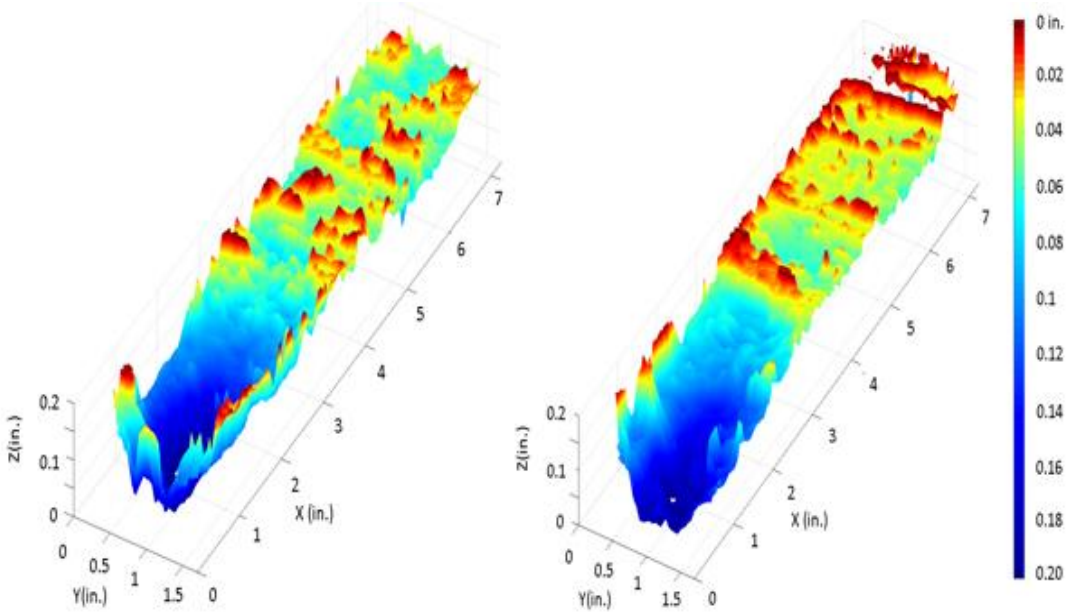

a) Before conductivity test

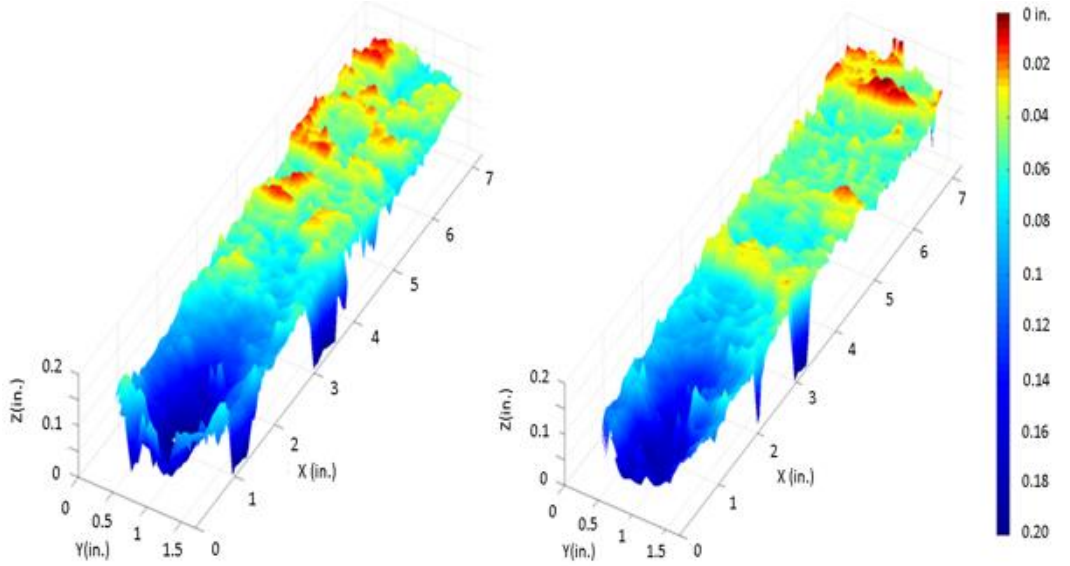

b) After conductivity test

Figure 3-15: Test 5 surface comparison before and after conductivity test (Reprinted from Jin et al., 2019).

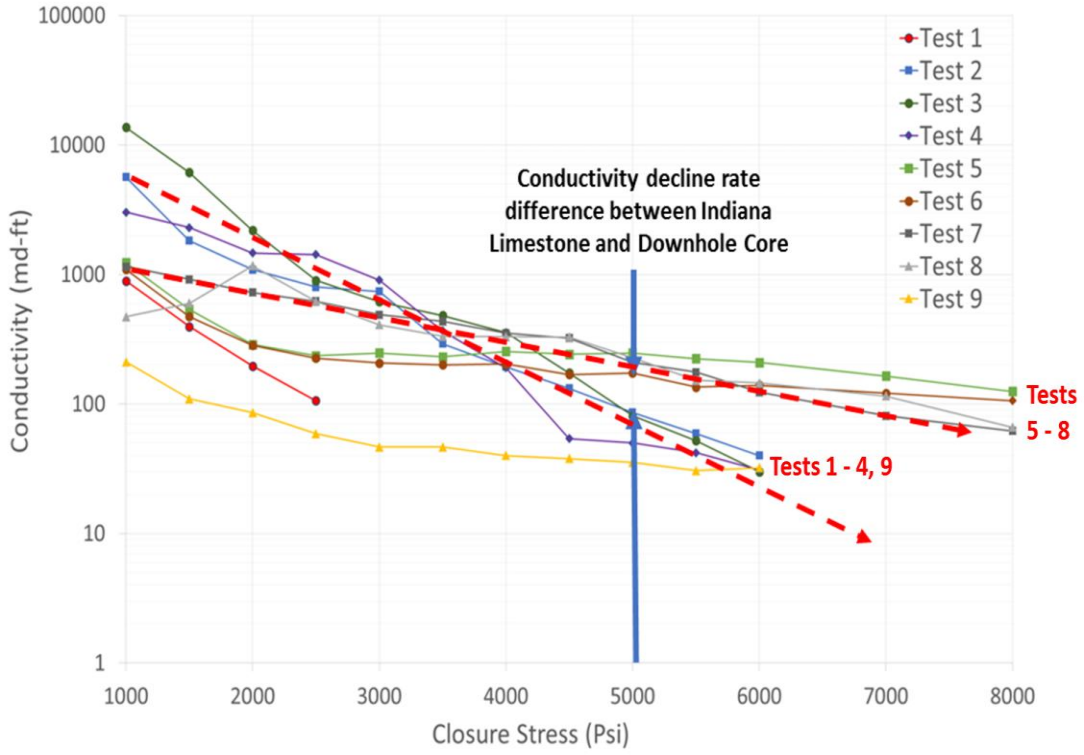

Figure 3-16: Conductivity of all tests showing the difference on initial conductivity and decline rate for Indiana Limestone and heterogeneous downhole cores (Reprinted from Jin et al., 2019).

3.5.5 X-Ray Fluorescence (XRF) Analysis

XRF tests have been conducted on several of the samples to accompany the XRD testing to identify the correlation between mineralogy distribution and etching patterns. XRF tests identify the elements on the fracture surface. The XRF tests are done on isolated square areas, and the elemental intensity values are taken as an average for each of the small squares. The layout is shown in **Figure 3-17**. Each of the boxes represents a 0.2 in. by 0.2 in. section on the sample surface. The XRF equipment takes an average intensity value at each of the blocks for each element. A darker red box means the box is saturated with that

element, while a lightly colored box will have low concentrations of the element. Higher intensity values can also show more reliability in the measurements (XRF equipment can detect Ca more clearly than Mg); otherwise, it is used as a way to qualitatively describe the saturation of the element in each grid box.

Figure **3-18** shows the surface scan of Test 7 after acid injection. This scan can be aligned with the XRF results to have a clearer picture of the impact of mineralogy distribution on etching/dissolution pattern. Figure **3-19** shows the mineral distribution of seven elements (Al, Ca, Fe, K, Mg, S, Si). The intensity color bar shows the concentration of each element within each box. Each image in Figure **3-19** uses a scale bar with a minimum intensity and maximum intensity value. For each element, the top picture is the XRF scan, the bottom image is the XRF image stacked on top of one of the surface scans after acidizing. The element Ca seems to correlate most closely with the yellow to blue regions, the more dissolved areas. Elements such as Al, K, and S, are more common in clay minerals. A high concentration of Si would dictate those regions have quartz, which XRD results showed approximately 11 percent of the rock sample.

Fracture face dissolution is correlated with Ca locations, which shows higher intensity values of dissolvable material. The mineral streaks are caused by HCl-insoluble minerals, correlated with Si locations. A very high intensity of Si (deep red box) would associate with the quartz minerals on the fracture surface. A lower intensity of Si (light red box) would correlate with the clay content on the fracture surface. Quartz was shown in Table **3-4** to have appeared in every one of the downhole samples.

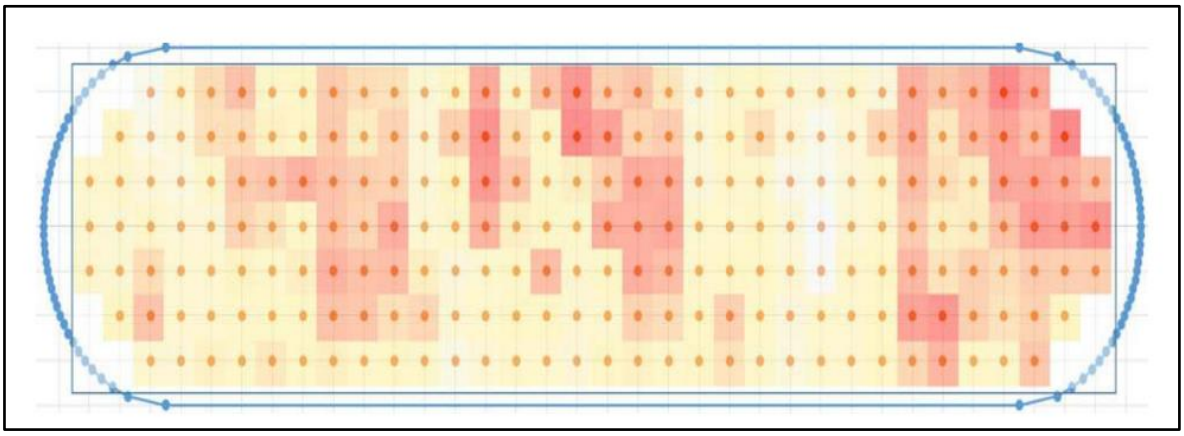

Figure 3-17: XRF grid system (Reprinted from Jin et al., 2019).

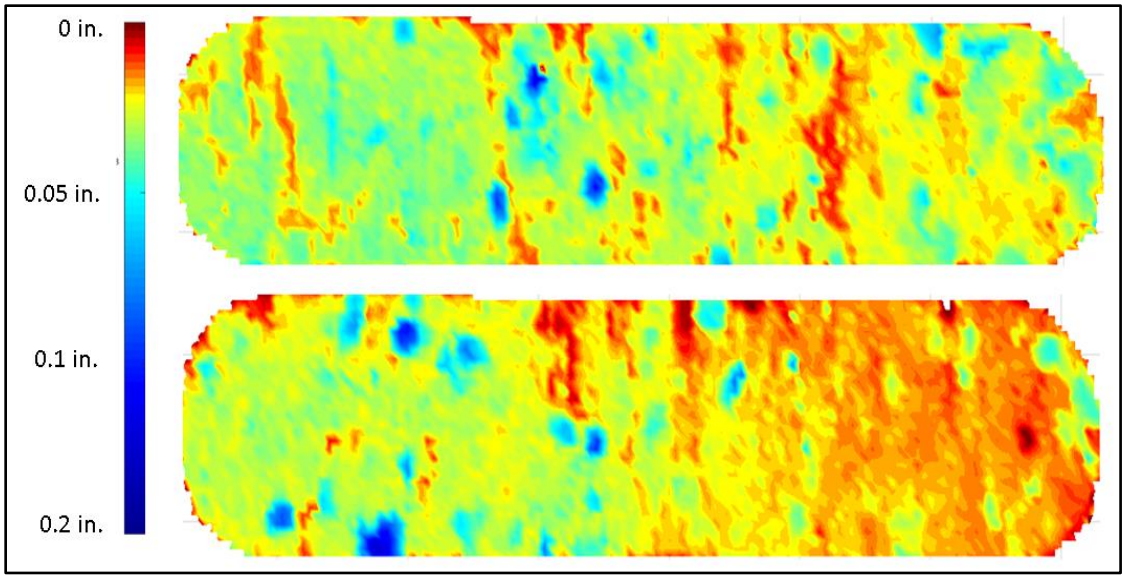

Figure 3-18: 2D surface scans for Test 7 (Reprinted from Jin et al., 2019).

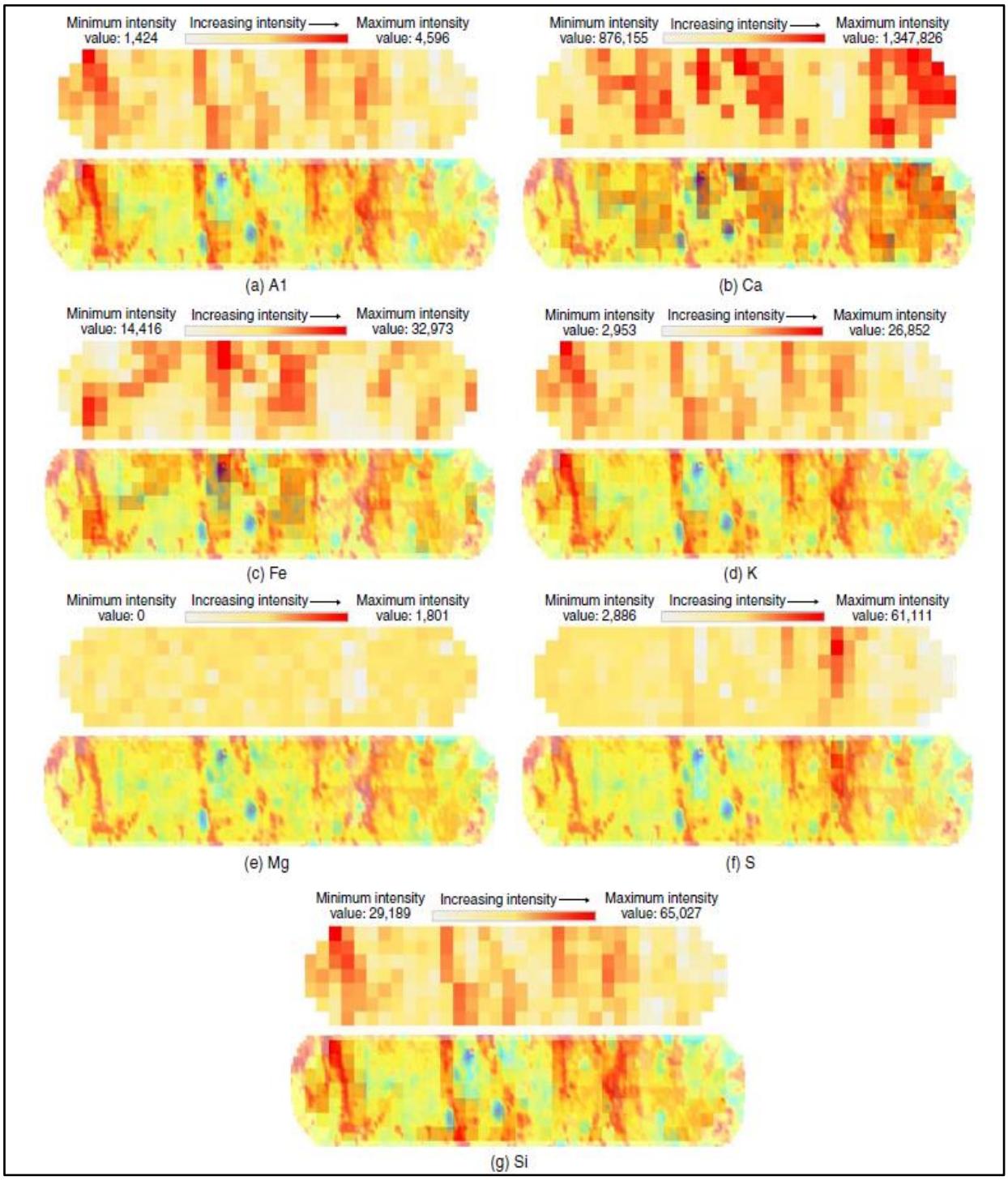

Figure 3-19 Mineralogy Distribution of Test 7 (Reprinted from Jin et al., 2019).

3.6 Acid Fracture Conductivity of Ratawi Limestone Downhole Samples*

A large part of the Ratawi formation is in the Wafra field consisting of three members: The Ratawi Oolite (base), the Ratawi limestone (middle), and the Ratawi Shale (top) (Al-Dwaish et al., 2016). The total thickness of the three members of the Ratawi formation totals 600 to 700 feet. The thickness of the Ratawi limestone member is around 100 feet. The depth of the formation is located at approximately 7,000. The Wafra field is located in the Partitioned Zone (PZ) between Kuwait and Saudi Arabia. The mineral rights in this region are shared equally between the two countries, and Saudi Arabian Chevron holds 100% ownership of the field (Naik et al., 2020).

Seven tests were conducted using the downhole samples from the Ratawi limestone. These tests are shown as Test 10 to 16 in Table **3-1**. Due to the limited amount of core material, only the fracture conductivity sets can be cut, core plugs to measure the permeability of the sample were then not able to be made. The average porosity of the samples is around 3%. Leak-off differential pressure was not applied. The fracture conductivity results of these tests ultimately determine if acid fracturing treatment is a viable simulation method for the formation that contains the Ratawi limestone applied.

---

* Reprinted with permission from Naik, Sarvesh, Dean, Mark, McDuff, Darren et al. 2020. Acid Fracture Conductivity Testing on the Tight Carbonate Ratawi Limestone in the Partitioned Zone. Presented at the International Petroleum Technology Conference, Dhahran, Kingdom of Saudi Arabia. 2020/1/13/. https://doi.org/10.2523/IPTC-19724-Abstract

3.6.1 X-Ray Diffraction Analysis (XRD)

The XRD results are shown in Table 3-7. Compare to the mineralogy content of the analog samples (Tests 5-9); the only new mineral is pyrite. The asterisk next to Test 10, 11, 15, and 16 indicates the samples were oil-saturated. The core material used to run the XRD test was also only from the oil-saturated regions. The cores were cleaned before XRD tests. The Dean-Stark equipment was used to remove the oil before crushing the core material. For Test 12, 13, and 14, the core material did not have oil-saturated regions. There is more variation in calcite percentage in these Ratawi limestone samples compared to the analog samples. However, if the calcite percentage and dolomite percentage were to be combined, the mineralogy that are dissolvable by HCl still exceeds 80%. Note the existence of quartz in all of the core material and dolomite only in the core material for Test 12, 13, and 16. Test 12 is dominated by dolomite instead of calcite.

Table 3-7 Mineralogy content for Middle East samples (Reprinted from Naik et al., 2020).

Minerals	Test 10*	Test 11*	Test 12	Test 13	Test 14	Test 15*	Test 16*
Calcite	99.76	99.08	26.69	67.35	98.26	99.74	97.33
Dolomite	0	0	61.77	19.26	0	0	2.11
Feldspar	0	0	0	0	0	0	0
Gypsum	0	0	0	0	0	0	0
Illite	0	0	0	3.16	0	0	0
Quartz	0.24	0.27	2.72	4.53	0.73	0.26	0.56
Kaolinite	0	0	7.49	5.7	1.01	0	0
Anhydrite	0	0	0	0	0	0	0
Pyrite	0	0.65	1.33	0	0	0	0
Total	100	100	100	100	100	100	100

3.6.2 Acid Fracture Conductivity Results of Ratawi Limestone Tests

Of the seven tests conducted, two of them (Tests 10, and 14) used straight 15% HCl, and two of them (Tests 11 and 15) used VES and three of the tests (Tests 11, 12, and 14) used an alternating injection of linear gelled acid – VES – linear gelled acid. The fracture conductivity results are plotted in Figure 3-20. Due to the more complicated mineralogy of the Ratawi limestone, the fracture conductivity test results also varied greatly in initial fracture conductivity. The highest initial fracture conductivity measured was 10,623 md-ft, and the lowest initial fracture conductivity measured was 67, more than 2 magnitudes different. Both a fast and slow fracture decline were observed with increasing closure stress. A high decline rate similar to Indiana limestone was observed in Test 13, and very slow conductivity decline similar to the analog samples was observed in Test 14.

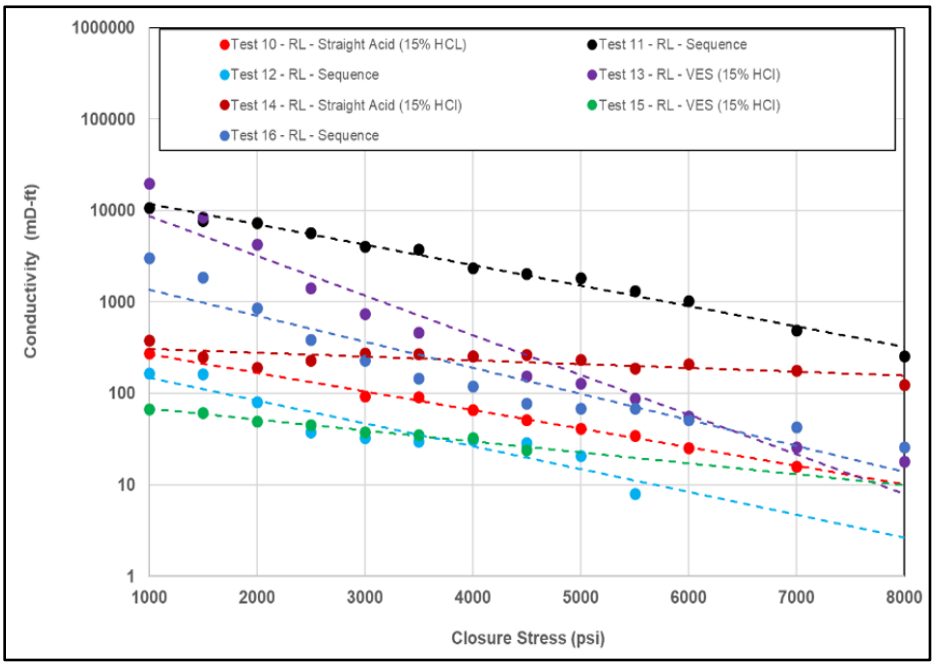

Figure 3-20: Fracture conductivity results of Tests 10 to 16.

The following sections discusses what contributed to the wide range of initial conductivity and fracture conductivity declines observed in Figure **3-20**. We start with what contributes to the lowest fracture conductivity and continue to the scenario that gives the overall highest fracture conductivity.

3.6.3 Impact of Acid-Etched Volume on Acid Fracturing Efficiency

The Ratawi limestone test with the lowest fracture conductivity at high closure stress is Test 12 (**Figure 3-21**). In Section 3.5.3, the study of the acid-etched volume on fracture conductivity efficiency showed that when the dissolved volume is too low, the fracture conductivity drops significantly. In Table **3-8** the lowest acid etched volume is Test 12. This test had both a very poor initial fracture conductivity and a high fracture conductivity decline. Similar to Test 9 with the analog samples, sequence injection of the linear gelled acid and VES was used. Comparing the three acid systems used for downhole samples (15% HCl, VES, and sequence injection), sequence injection appears to most likely cause low acid-etched volumes due to it being a two-part linear gelled acid system, which is the least reactive of the acid types between straight HCl, VES, and linear gelled acid.

Table 3-8: Acid-etched volumes for field samples (Reprinted from Naik et al., 2020).

Test No	Acid System	Acid-Etched Volume (in^3)
10	Straight Acid (15% HCl)	0.84
11	Sequence	0.57
12	Sequence	0.27
13	VES (15% HCl)	0.94
14	15% HCl	1.66
15	VES (15% HCl)	0.91
16	Sequence	0.65

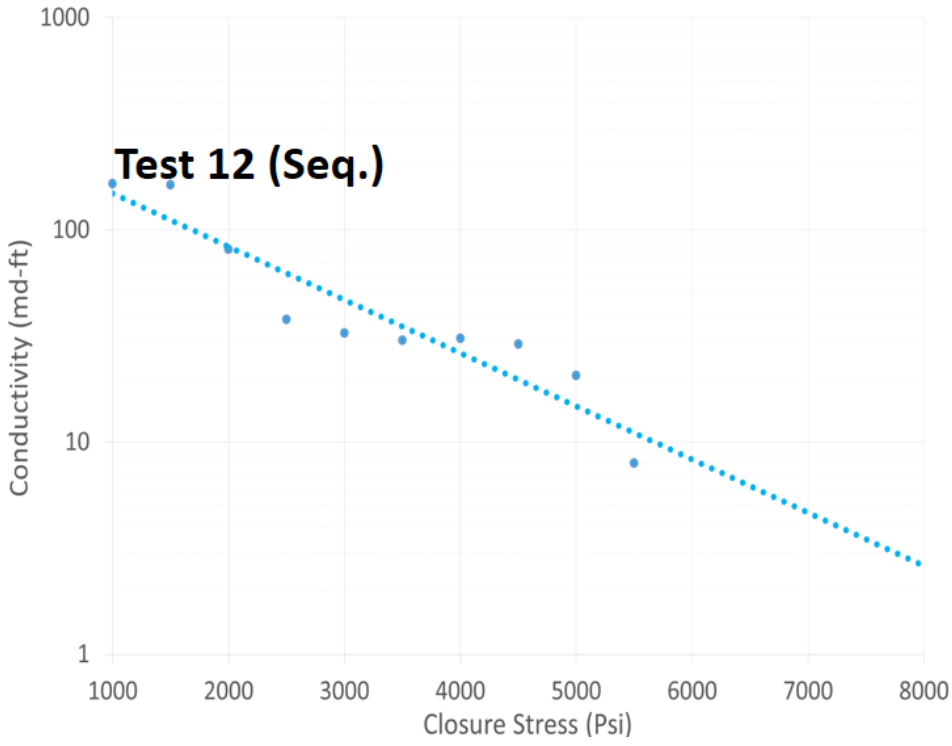

Figure 3-21: Poor fracture conductivity due to low acid-etched volume.

3.6.4 Impact of Thick Mineral Streaks on Fracture Conductivity

Test 10 and Test 15 both had oil saturated regions on the fracture surface. Trims with darker regions were isolated from the trims with no dark regions. The Dean-Stark apparatus was used on the dark colored samples. Oil was confirmed to be removed. These originally oil-saturated trims were then crushed and made into samples for XRD. XRD results show these dark regions are made up of >99% calcite.

These oil-saturated calcite areas were less reactive with acid, which left wide mineral streaks. However, unlike the mineral streaks made from HCl-insoluble minerals, these oil-saturated streaks have weaker mechanical properties, leading to poor fracture conductivity. Additionally, wider mineral streaks perpendicular flow also increases the flow resistance during nitrogen flow. The oil-saturated regions are clearly observed in **Figure 3-22** as darker regions on the fracture surface. The surface scan of one of the the after acidized surface is shown on the right side of **Figure 3-23**. Test 10 showed oil-saturated regions as both wide streaks and thin streaks perpendicular to the flow direction. This led to slightly better result than Test 15 because the wide mineral streaks did not fully block flow.

Figure 3-22: Test 15 before acidizing (left) and after acidizing (right).

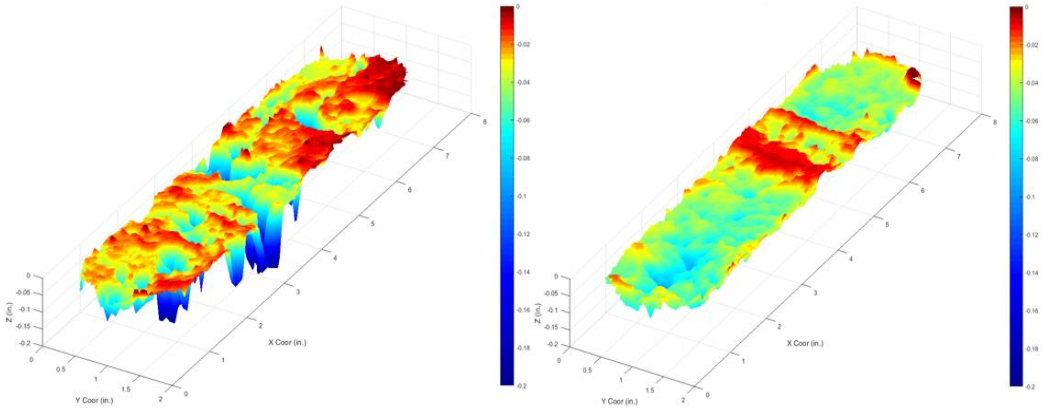

Figure 3-23: Poor fracture conductivity due to low acid-etched volume.

The fracture conductivity is plotted in **Figure 3-24**. Test 10 is shown in orange, and Test 15 is shown in yellow. While both tests showed poor fracture conductivity, they still performed better compared to Test 12, which was discussed in Section 3.6.3,

suffered from low acid-etched volume on the fracture surface. Test 12 is shown as the white plot.

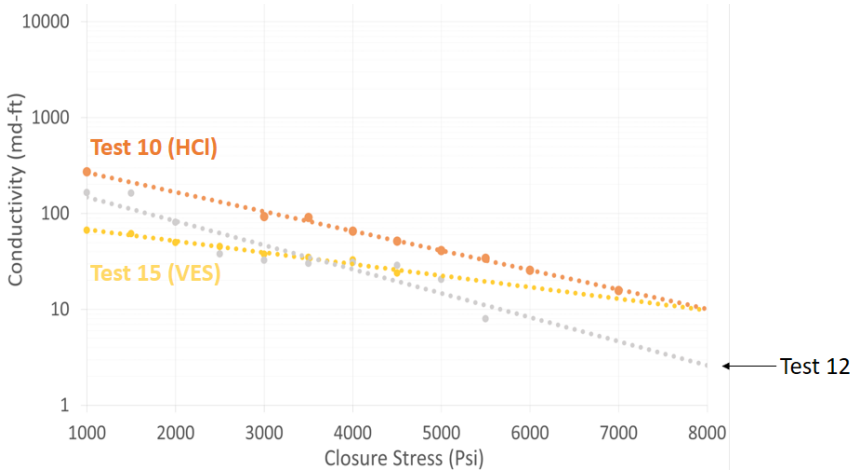

Figure 3-24: Poor fracture conductivity due to wide mineral streaks

3.6.5 Impact of Thin Mineral Streaks on Fracture Conductivity

While the wide mineral streaks in the previous section were made of less reactive calcite due to being oil-saturated (Naik et al., 2020), the thin HCl-insoluble mineral streaks provided better support for higher fracture conductivity measurements likely due to better mechanical properties (confirmed in Chapter 4 with the testing of the Young's Modulus using a triaxial testing apparatus). **Figure 3-25** shows Test 14 and Test 16 both as blue lines, and the white lines are the previously discussed Test 10, 12, and 15. In Test 14, the fracture conductivity decline rate is very low because the thin HCl-insoluble mineral streak was able to withstand closure stress. The initial conductivity of Test 14 is lower because Test 16 did not have mineral streaks that fully cross the entire sample

against the flow direction. The channeling created by the viscosified acid systems also increased the initial conductivity of Test 16 compared to Test 14.

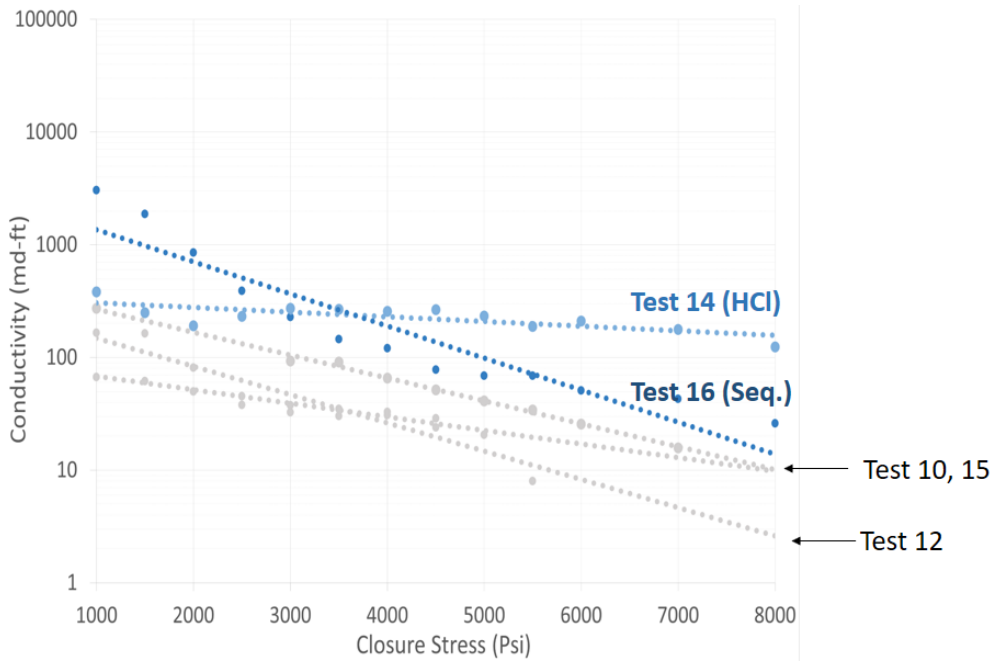

Figure 3-25: Fracture conductivity of Test 14 and Test 16.

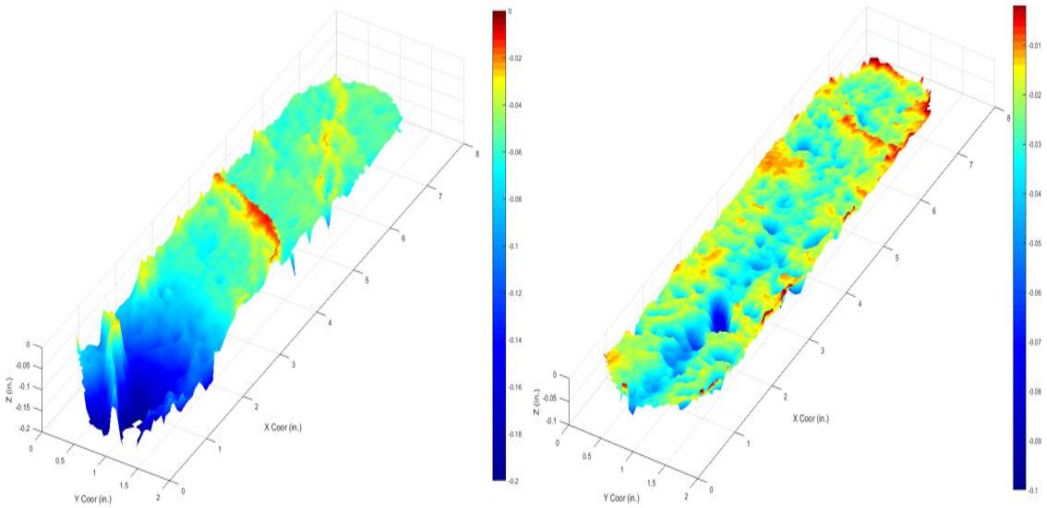

Figure 3-26: Surface scans of Test 14 (left) and Test 16 (Right).

These tests on the Ratawi limestone most closely resemble that of the tests on the analog downhole samples.

3.6.6 Impact of Dolomite Channel on Fracture Conductivity

Test has higher dolomite content than the previous tests. The first half of the sample has high calcite content, and the second half high in dolomite. **Figure 3-27** shows the fracture conductivity result compared to the previously discussed tests. The initial fracture conductivity was the highest, but the fracture decline rate was also the highest. **Figure 3-28** shows the XRF scan results. The red area in the XRF scan is the magnesium, which also represents the dolomite region.

Test 13 was similar to Test 4 in fracture conductivity measurement (**Figure 3-29**) and surface etching pattern (**Figure 3-30**) in the fact that an uninterrupted channel was created. This type of channel leads to high initial fracture conductivity. The high fracture conductivity decline of both tests is due to the material holding the fracture open exist only on the sides of the surface rather than across the entire sample, as shown in previous tests. The HCl-insoluble minerals that typically holds open the fracture seem to be less in Test 13 than the other samples. Lastly, it is important to note again that XRD results are from the trims cut after making the conductivity sample, so the HCl-insoluble minerals of illite, quartz, kaolinite may not be represented as such on the fracture surface of the samples used for Test 13.

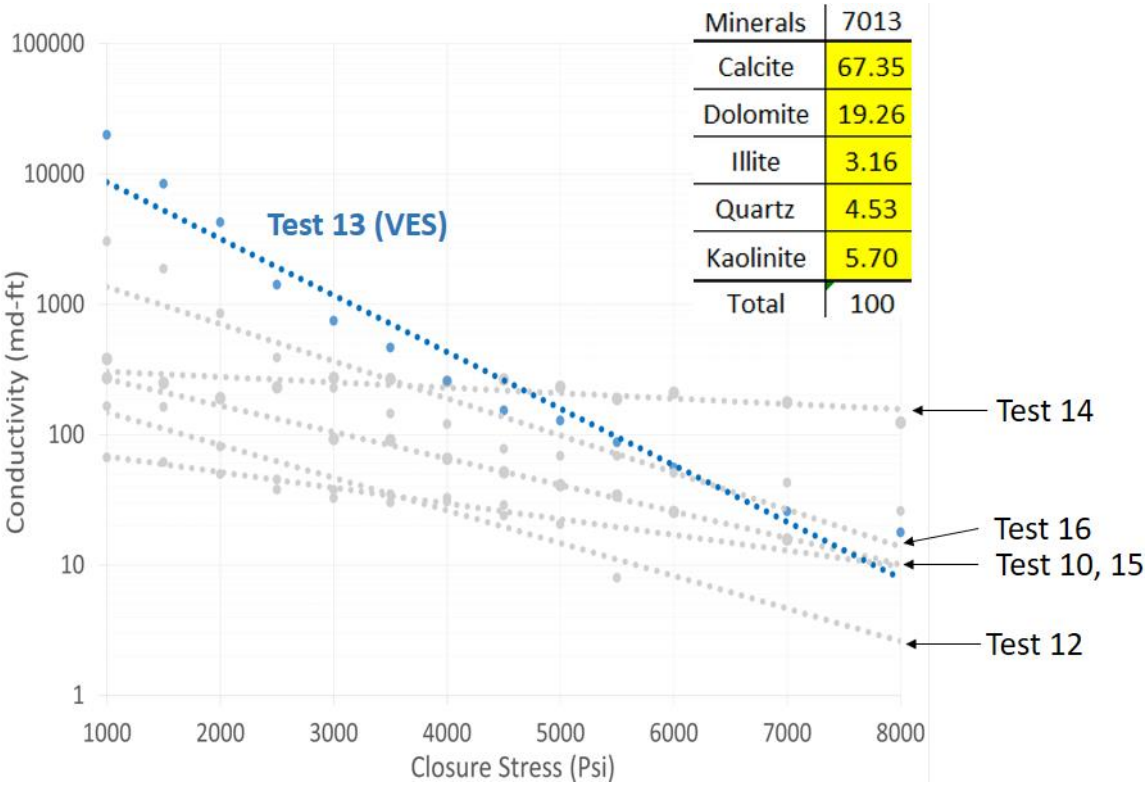

Figure 3-27: Fracture conductivity result for Test 13.

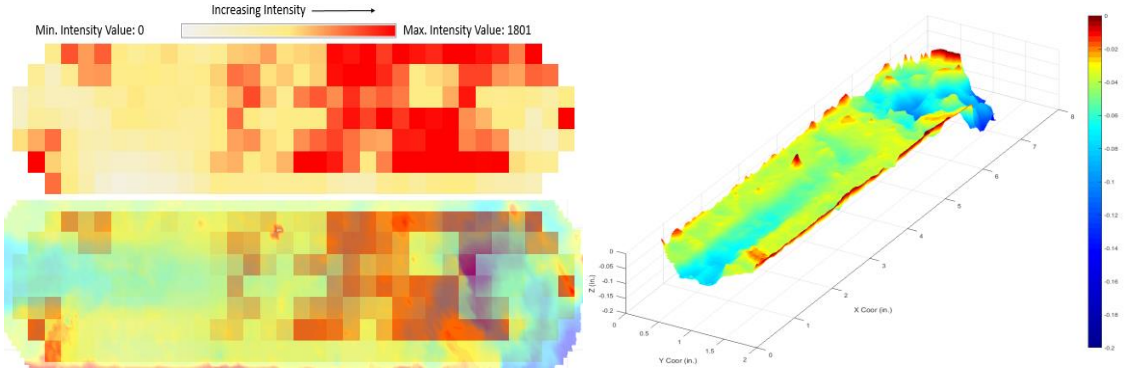

Figure 3-28: XRF surface showing high magnesium as red and the corresponding surface scan of one side.

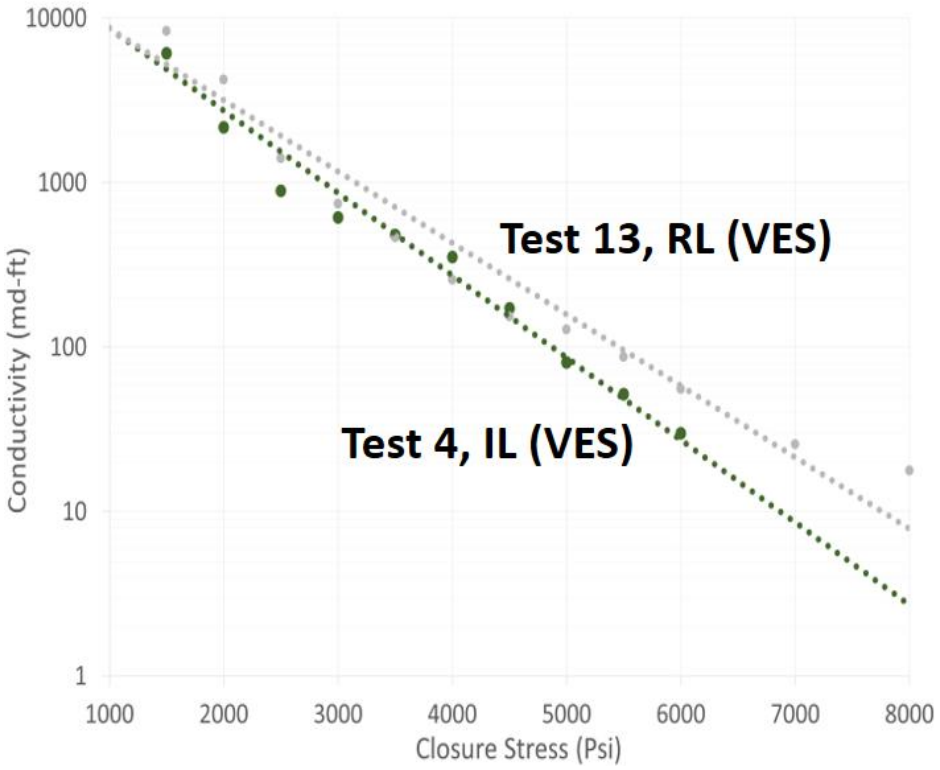

Figure 3-29: Comparing Test 4 and Test 13, both with high initial fracture conductivity and high fracture conductivity decline.

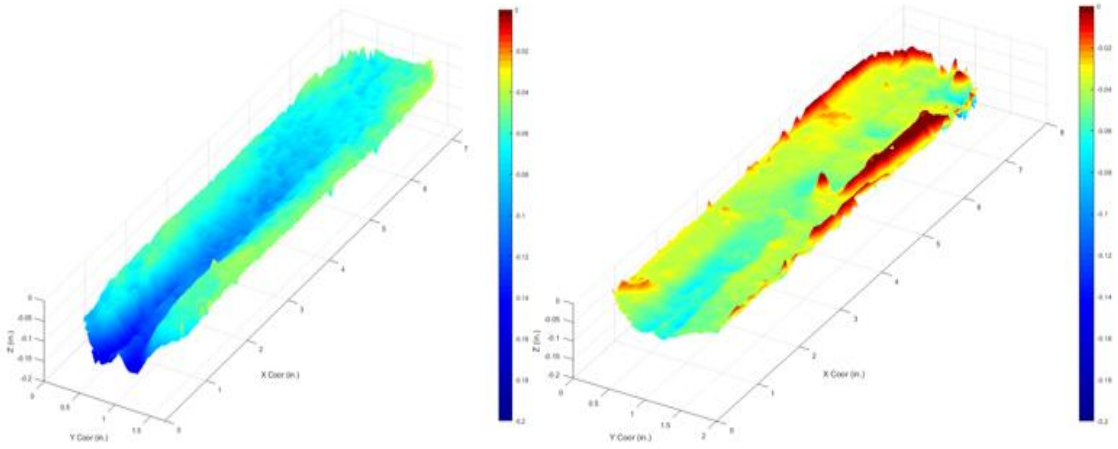

Figure 3-30: Surface scan of one side of Test 4 and one side of Test 13.

3.6.7 Conditions For Creation of the Highest Fracture Conductivity

When the insoluble mineral distribution on the fracture surface aligns with the flow direction, and when sufficient reaction between rock and the acid system occurs (measured by the acid-etched volume), the combination of these two conditions provide the best conductivity behavior; high initial and low decline. Test 11 in this study is the best example of this situation, as shown in (**Figure 3-31**). From the surface scans in **Figure 3-32**, we observe that the viscosified acid created a channel, and the channel was not blocked by the partial mineral streak against the flow direction. Also, the surface HCl-insoluble minerals had strong enough mechanical properties to withstand 8,000 psi of closure stress without being crushed.

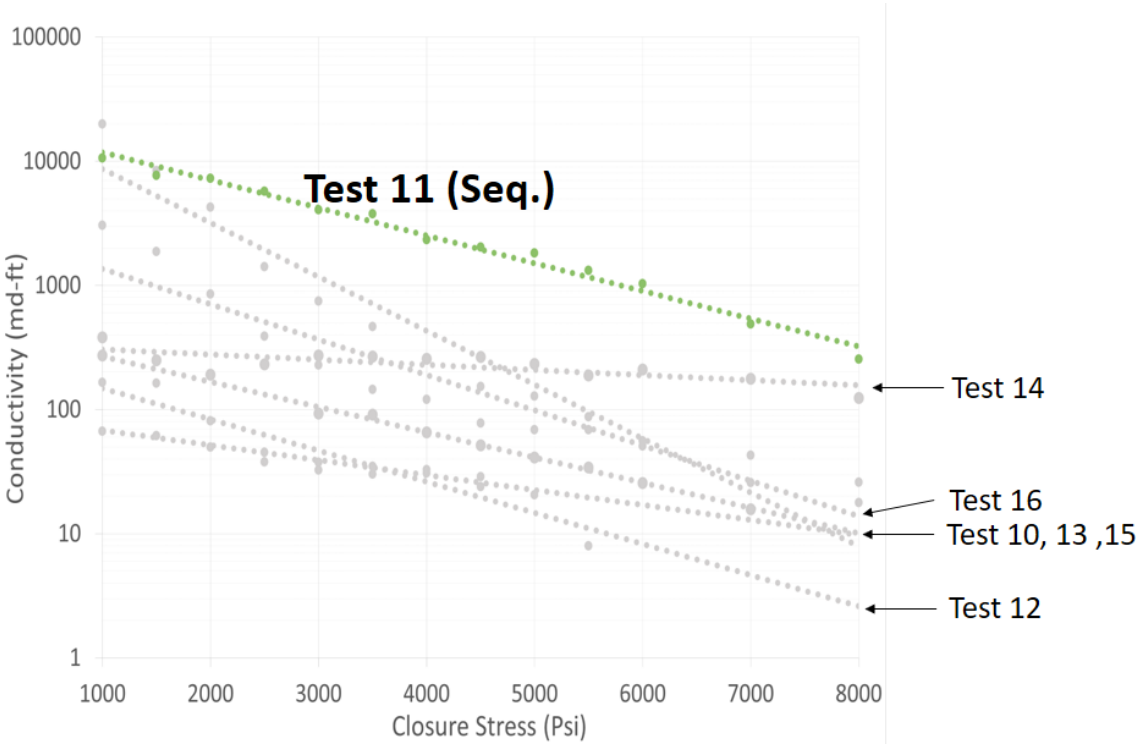

Figure 3-31: Fracture conductivity results of Test 11.

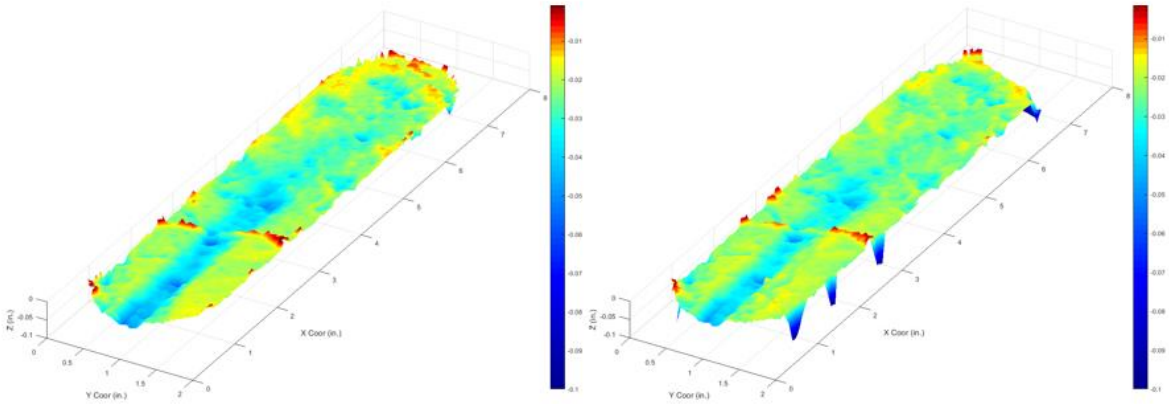

Figure 3-32: Surface scans of Test 11 after acidizing (left side) and after fracture conductivity test (right side).

3.7 Chapter Summary

Sixteen total tests were conducted. Of the 16 tests conducted, 4 of them are baseline tests using outcrop Indiana Limestone rocks. Five of which used analog limestone rock samples from the U.S., and seven tests using Ratawi Limestone samples. The experimental results offered insights on how surface mineral heterogeneity affects fracture conductivity. Some of the conclusions from this study are given below:

- The downhole samples (Tests 5-16) showed sustained fracture conductivity can be created with acid fracturing stimulation because of the heterogeneity of rock mineral contact. Comparing these 12 tests to the Indiana Limestone tests, 7 of the 12 downhole samples had higher fracture conductivity at closure stresses less than 3,000 psi, and 9 of the 12 performed better at closure stresses up to 5,000 psi.

- The selection of the acid system is essential to create enough acid-etched volume. Modified acid systems such as gelled acid and VES further reduce the dissolved volume for the tests using heterogeneous samples and could show negative impacts on fracture conductivity. If using a modified acid system, the design needs to consider that enough reaction occurs to create uneven surface for conductivity. The insoluble minerals are harder to crush compared with calcite, and therefore can sustain fracture conductivity at high closure stress.
- For high calcite content zones, sequence injection can create channel-like dissolution patterns that could enhance fracture conductivity.
- When the insoluble mineral distribution on the fracture surface aligns with the flow direction, and when sufficient reaction between rock and the acid system occurs (measured by the acid-etched volume), the combination of these two conditions provide the best conductivity behavior; high initial conductivity and low decline.

4 MODIFIED MOU-DENG CORRELATION FOR ACID FRACTURE CONDUCTIVITY

4.1 Introduction

In the previous chapter, the effect of mineral heterogeneity on fracture conductivity was investigated. However, the study was done at the laboratory scale, which needs to be scaled to the fracture conductivity at field scale. Laboratory studies can often be used as qualitative studies to compare acid systems and design parameters on the resultant fracture conductivity. With proper upscaling, the laboratory results could assist in field treatment designs. In this chapter, we examine the correlations that are used to upscale field results. This begins with using an intermediate-scale empirical correlation that was originally benchmarked using acid fracturing experimental results with Indiana limestone. The correlation is modified to capture fracture conductivity behavior observed in the experimental investigation in this study by the downhole samples. Due to the limited Ratawi limestone core material for mechanical properties testing to determine the Young's Modulus, the analog limestone cores from the U.S. were used to test the mechanical properties.

4.2 Mechanical Properties Testing of Analog Limestone Downhole Samples

Three triaxial tests were done with 1 in. by 2 in. core plugs. These core plugs were cut from the extra core material available to the analog Tests 5-9. The initial set up for triaxial testing is shown in Figure **4-1**. The experiment uses a linear variable differential transformer (LVDT), which measures small changes along the vertical and radial directions. The LVDT allows the measurement of change on the core sample, which to

calculates both the Young's Modulus and Poisson's Ratio. Since the Mou-Deng correlation only considers the Young's Modulus, only that properly will be calculated from the triaxial tests.

The core plug is placed inside the triaxial testing cell shown in Figure **4-2**. Since the testing procedure follows standard API procedure (unlike the modified fracture conductivity testing), the procedure will not be included.

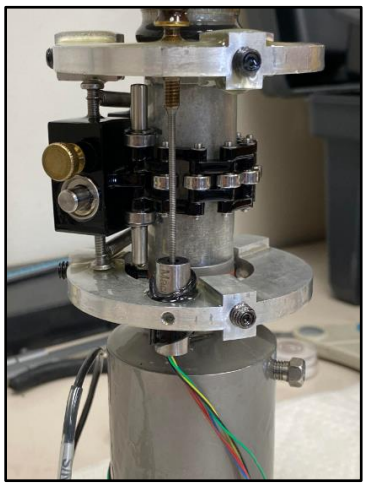

Figure 4-1: Setup of core sample before triaxial test.

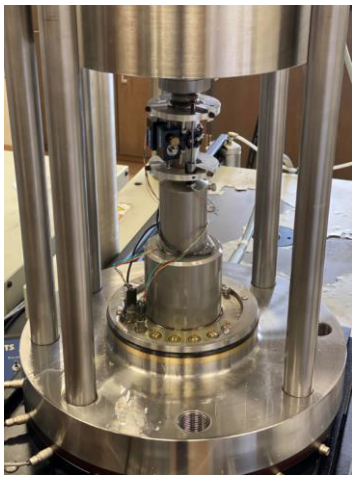

Figure 4-2 Sample placed in triaxial testing cell.

The first triaxial test done with a maximum deviator stress of 80 MPa (11,603 psi), at which no more deviator stress is applied. The plot relating deviator stress to axial strain percentage is shown in Figure **4-3**. The deviator stress is the difference between the major and minor principal stresses. Taking the section of the plot that considered to be linear (in between the two vertical lines), the slope of the line is the Young's Modulus. The unit of Mpa is converted to MPsi afterward.

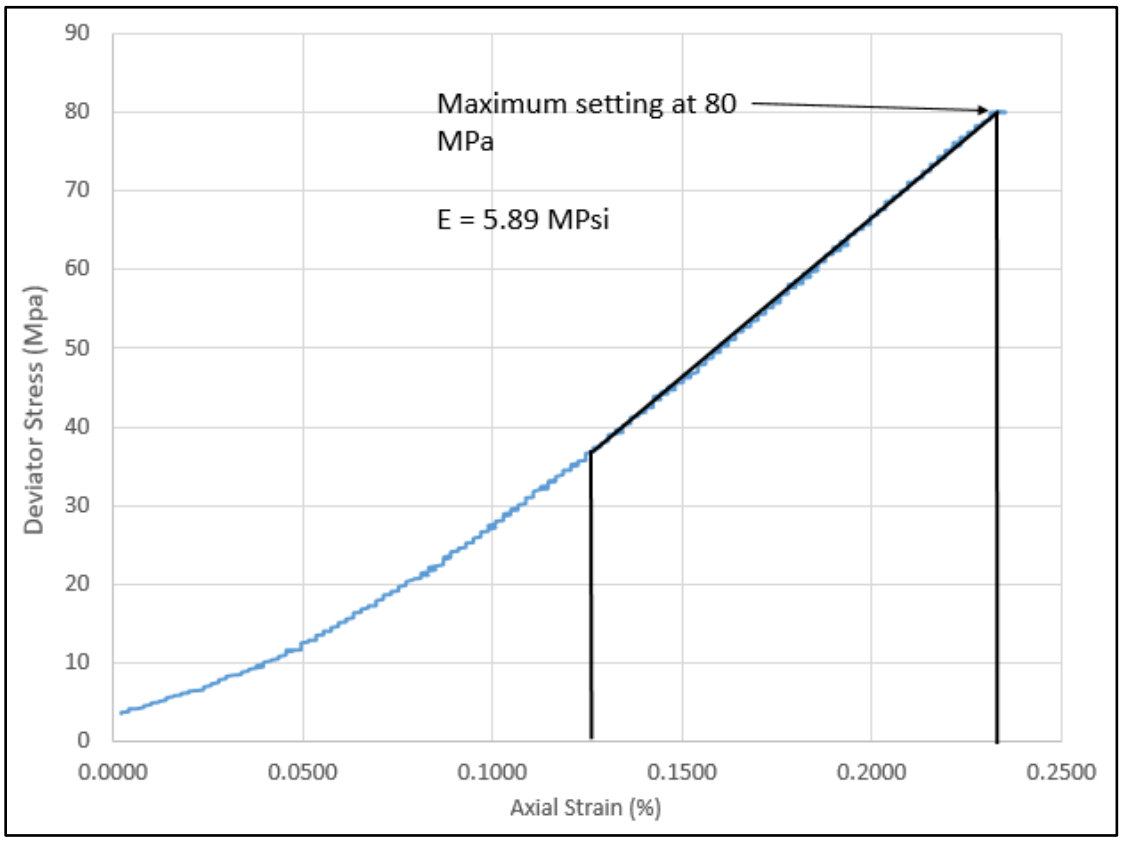

Figure 4-3: Test 1deviator stress versus axial strain.

The result of the first test was a Young's Modulus of 5.89 MPsi, which is typically considered a strong sample that should withhold high closure stress. In a parametric case study done by Deng et al. (2013), he showed that for rocks that have low Young's

Modulus, fracture conductivity could change by almost a magnitude at higher closure stress of 4,000 psi (Figure **4-4**), which is the expected closure stress of the Ratawi limestone. The triaxial tests discussed later will have a low range of experimentally determined Young's Modulus.

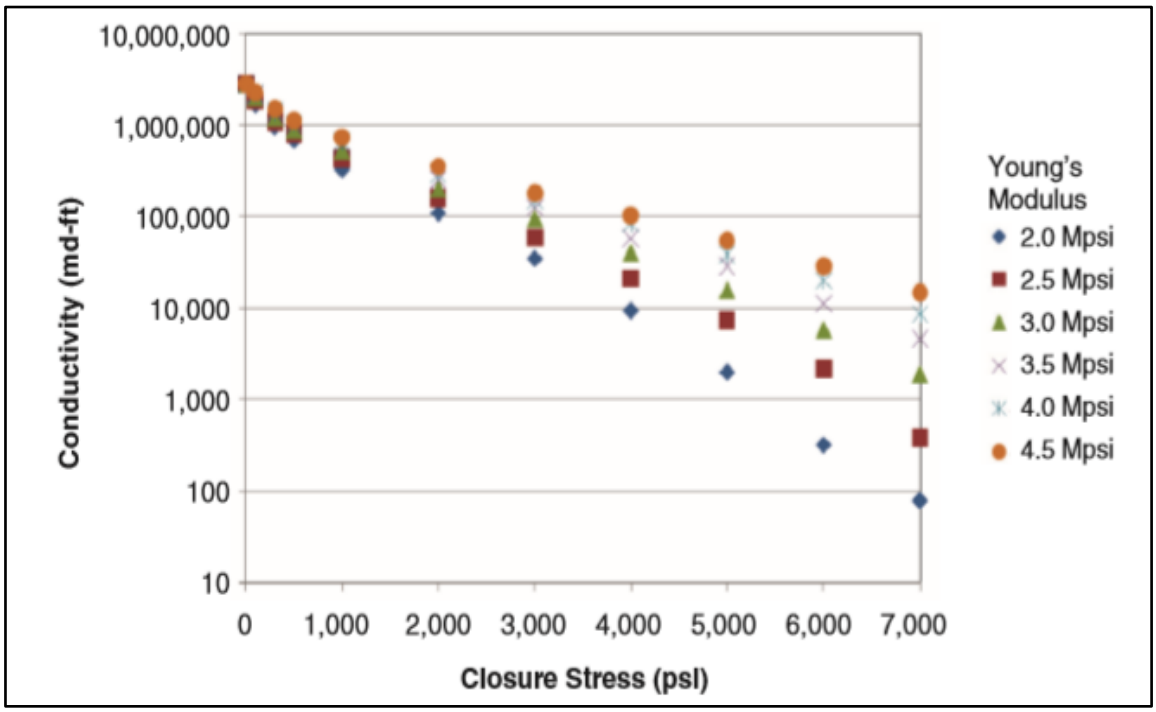

Figure 4-4: Effect of Young's Modulus on fracture conductivity (Reprinted from Deng et al., 2013).

The second triaxial test resulted in a low Young's modulus of 1.96 Mpsi. The rock broke before the deviator stress reached 50 Mpa. When the rock fails, there is a chance to damage the LVDT in the vertical direction, so the test should be terminated as soon as the deviator stress level off (**Figure 4-5**).

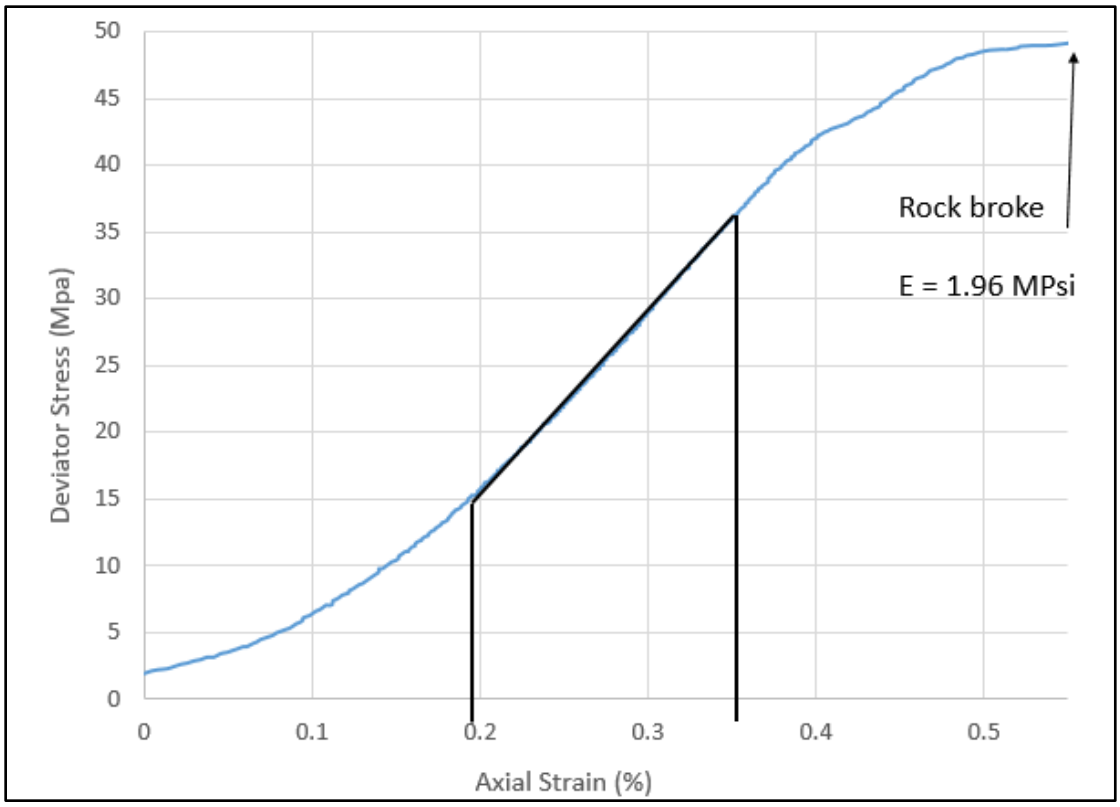

Figure 4-5 : Test 2 deviator stress versus axial strain.

Test 3 (Figure **4-6**) also showed resulted in a similar Young's Modulus compared to triaxial test 2. In this case, the resulting Young's Modulus was 1.91 Mpsi. The results of the three Young's Modulus tests showed a range of 1.91 to 5.89 Mpsi. With a heterogeneous downhole sample and its more complicated mineralogy, a wide range of Young's Modulus value is expected. Given the available core samples for this study, we will use this range as the lower and upper bounds to correct the correlation.

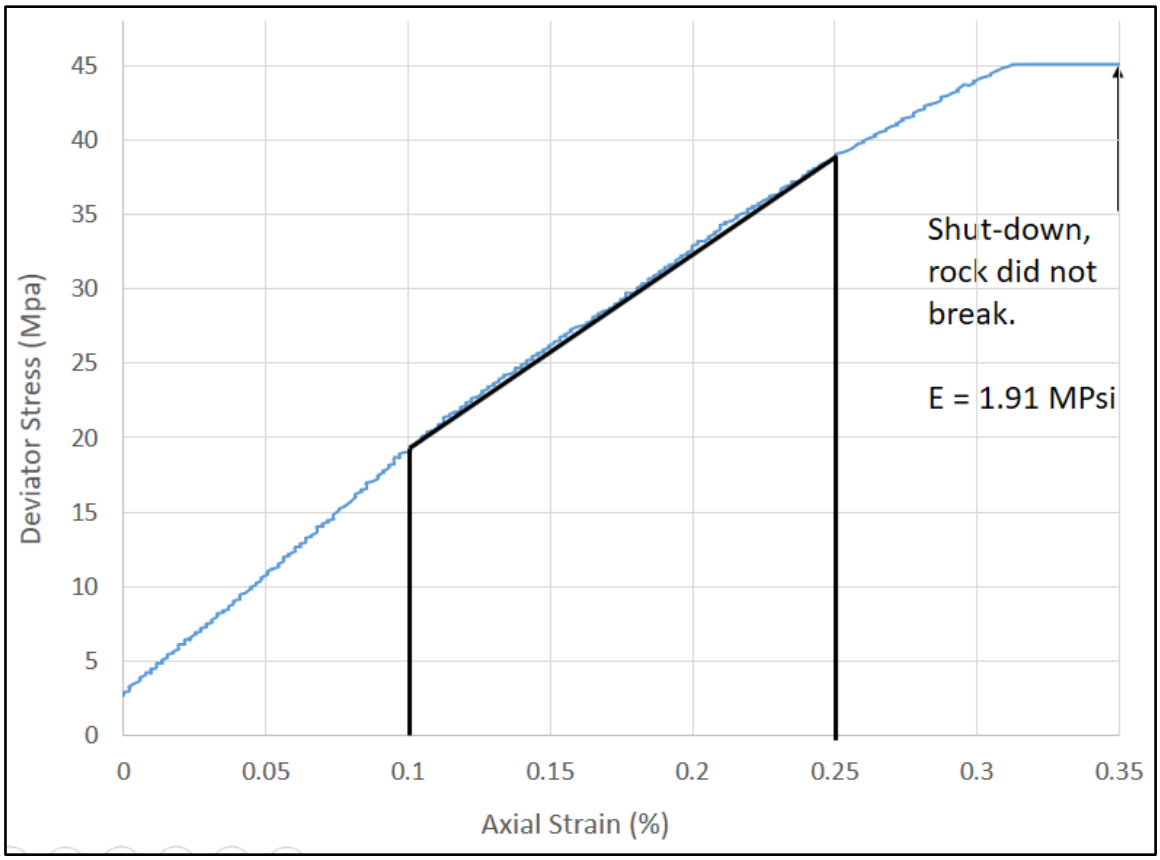

Figure 4-6: Test 3 deviator stress versus axial strain.

4.3 Summary of the Mou-Deng Correlations

In acid fracture stimulation after the etched-width is simulated, one uses a correlation to calculate the overall fracture conductivity. The commonly used correlation is the the Nierode and Kruk correlation (1973), which does not account for the distribution of permeability and mineralogy on the fracture face and their effect on fracture conductivity. Modified correlations were presented by Deng et al. (2011) to predict fracture conductivity as a function of closure stress and capture the impacts of permeability and mineralogy effects. These correlations use the conductivity at zero closure stress presented by Mou et

al. (2010). The Mou correlations are divided into three conditions: 1) a permeability-distribution dominated case; 2) mineralogy-distribution dominated case, and 3) competing effects of permeability- and mineralogy-distribution case. Case 1 is typically used to predict fracture conductivity in homogenous formations dominated by calcite or dolomite minerals, where fracture conductivity is created due to permeability differences on the fracture surface during the acid injection. The uneven etching is the source of fracture conductivity. Case 2 and 3 are used when the formation is more heterogeneous.

Four parameters were considered in Mou-Deng's correlation. Two dimensionless statistical parameters, $\lambda_{D,x}$ and $\lambda_{D,z}$, characterize how permeability and mineralogy are geostatistically correlated to the flow direction. $\lambda_{D,x}$ is the dimensionless horizontal correlation length and $\lambda_{D,z}$ is the dimensionless vertical correlation length. The dimensionless standard deviation of the natural log of permeability, σ_D, describes the heterogeneity in permeability. The final parameter, $f_{calcite}$, describes the percentage of calcite. The range for each of the geostatistical parameters were given in Deng et al., (2012). The range for $\lambda_{D,x}$ was suggested as $0.0156 \leq \lambda_{D,x} \leq 1$, where increasing $\lambda_{D,x}$ indicates an increase in the uniformity of mineralogy in the flow direction, and therefore increase fracture conductivity. The range for $\lambda_{D,z}$ was given as $0.004 \leq \lambda_{D,z} \leq 0.5$, where increasing $\lambda_{D,z}$ indicates the permeability is more correlated in the direction perpendicular to flow, and therefore would decrease the fracture conductivity. The standard deviation σ_D has a range of $0.1 \leq \sigma_D \leq 0.9$, where increasing σ_D would increase variation of mineralogy, and resulting in a more heterogeneous formation. More details

on how to obtain the statistical parameters used in this correlation can be found in Oeth et al. (2011).

In this chapter, the permeability-distribution dominated case is first used to match the fracture conductivity results of Indiana Limestone. Then the mineralogy dominated case is modified to include geostatistical parameters to capture the low decline rates observed from this study.

4.4 Modify Correlation with Experimental Results of Indiana Limestone Cores for the Permeability-Distribution Dominated Case

The Mou-Deng correlations for the permeability-distribution dominated case are given in Equations 4-1 through 4-5,

$$(\mathrm{wk_f})_0 = 4.48*10^9 \bar{w}^3 \left[1 + \left(a_1 erf\left(a_2\left(\lambda_{D,x} - a_3\right)\right) - a_4 \,\mathrm{erf}\left(a_5\left(\lambda_{D,z} - a_6\right)\right)\right)\right] \sqrt{(e^{\sigma_D} - 1)} \quad (4\text{-}1)$$

$$\alpha = (wk_f)_0 \left[0.22(\lambda_{D,x}\sigma_D)^{2.8} + 0.01\left(\left(1 - \lambda_{D,z}\right)\sigma_D\right)^{0.4}\right]^{0.52} \quad (4\text{-}2)$$

$$\beta = [14.9 - 3.78\ln(\sigma_D) - 6.81\ln(E)] * 10^{-4} \quad (4\text{-}3)$$

$$\bar{w} = 0.56\,\mathrm{erf}\,(0.8\sigma_D) w_i^{0.83} \quad (4\text{-}4)$$

$$wk_f = \alpha e^{-\beta\sigma_c} \quad (4\text{-}5)$$

where wk_f, is the fracture conductivity in md-ft, $(wk_f)_0$ is the fracture conductivity at zero closure stress in md-ft, w_i is the ideal width in inches, $\bar{w}$ is the average width in inches, and a_1, a_2, a_3, a_4, a_5, and a_6 are constants. The values of the constants are

provided in Table 4-1. The initial fracture conductivity is given by α. The β term controls the decline rate of the fracture conductivity, accounting for the importance of mechanical properties.

Table 4-1: Constants for equation 1.

Constants	Values
a1	1.82
a2	3.25
a3	0.12
a4	1.31
a5	6.71
a6	0.03

Figure 4-1 shows the fracture conductivity calculation using the Mou-Deng model. The initial conductivity can vary greatly depending on the correlation length value and the acid-etched volume. The yellow line is calculated with the highest acid-etched volume from the experiments and using a perfect correlation length of one along the x-direction. The red line is calculated with the lowest experimental acid-etched volume and a low correlation length along the x-direction of 0.1. While the initial fracture conductivity can

vary by two magnitudes (depending on the selection of geostatistical parameters and acid-etched volume), the decline rate is more consistent and maybe more important. β controls the fracture conductivity decline rate as closure stress increases; it becomes more critical at higher closure stress. In the figure, the decline rate of the conductivity is very consistent with the four experimental tests using Indiana limestone (Tests 1-4). This is expected as the permeability-distribution model was first developed for an intermediate scale, 10 feet by 10 feet domain, and then corrected with the constants to fit the experimental results of previous Indiana limestone tests.

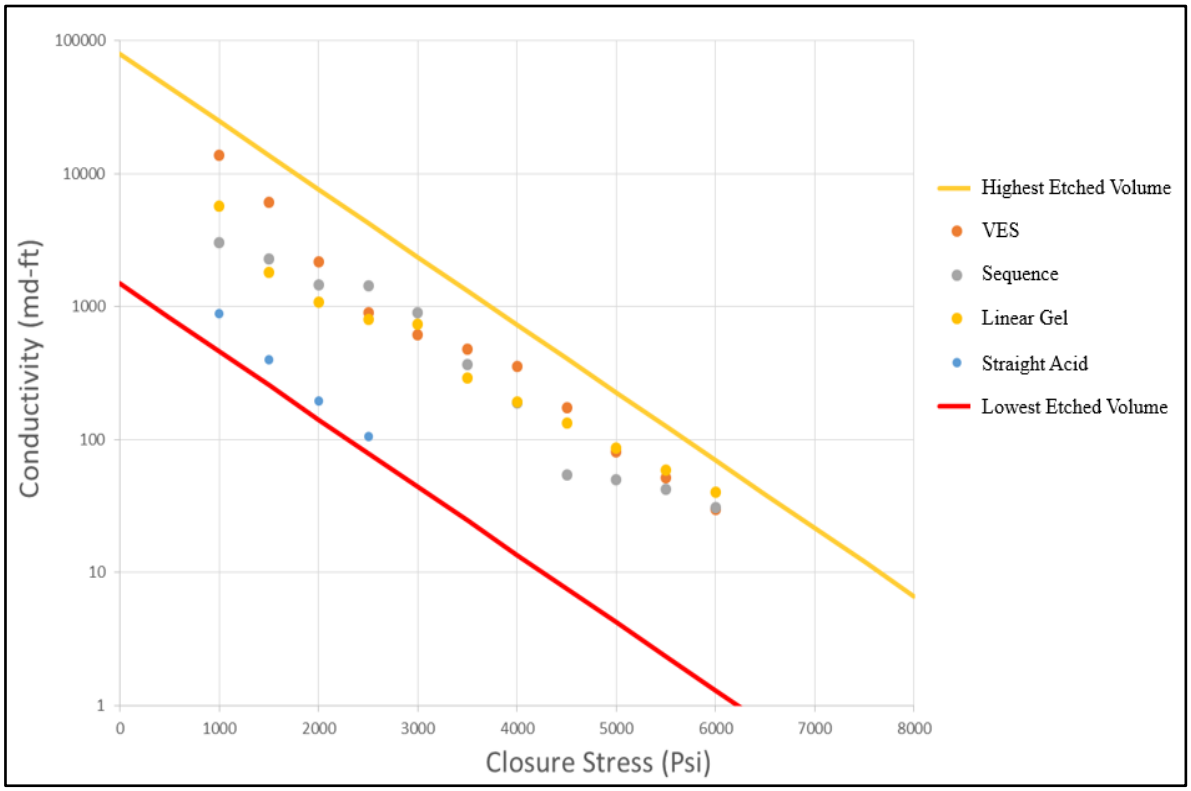

Figure 4-7: Applying the Mou-Deng correlation to Indiana Limestone Tests.

4.5 Modifying the Mou-Deng Correlations with Experimental Results of Analog Limestone Downhole Cores

The Mou-Deng correlations for mineralogy is given in Equations 4-6 through 4-9,

$$(\mathrm{wk_f})_0 = 4.48*10^9(1 + 2.97(1 - f_{calcite})^{2.02}]x[0.13f_{calcite}^{0.56}]^3 w_i^{2.52} \quad (4\text{-}6)$$

$$\alpha = (wk_f)_0[0.81 - 0.853f_{calcite}]^{0.52} \quad (4\text{-}7)$$

$$\beta = [1.2\exp(0.952f_{calcite}) + 10.5E^{-1.823}]x10^{-4} \quad (4\text{-}8)$$

$$wk_f = \alpha e^{-\beta\sigma_c} \quad (4\text{-}9)$$

This model assumes the mineralogy exists as streaks parallel to the flow direction only; hence, no geostatistical parameters are included. This would give the highest predicted initial conductivity and would over-predict the fracture conductivity if used in an acid fracturing model to calculate the final fracture conductivity. From the experimental study, the minerals on the fracture faces are often observed to be not perfectly parallel to flow, but distributed randomly and creating tortuous pathways. To capture this effect, the mineralogy-distribution model should also consider changes in the geostatistical properties.

The mineralogy-dominated correlation is derived from the correlation for competing effect of permeability and mineralogy-distribution. This competing effect correlation is given in Equations 4-10 through 4-13.

$$(\mathrm{wk_f})_0 = 4.48 * 10^9\left[1 + a_1 + \left(a_2\,\mathrm{erf}\left(a_3\left(\lambda_{D,x} - a_4\right)\right) - a_5\,\mathrm{erf}\left(a_6\left(\lambda_{D,z} - a_7\right)\right)\right)\sqrt{e^{\sigma_D} - 1}\right] X\left[a_8 f_{calcite}^{a_9} + a_{10}\sigma_D\right]^3 w_e^{a_{11}} \quad (4\text{-}10)$$

$$\alpha = (wk_f)_0\left[0.21\lambda_{D,x}^{0.16} + 0.046\ln(\sigma_D) + 0.15\lambda_{D,z}^{-0.17}\right] \quad (4\text{-}11)$$

$$\beta = [53.8 - 4.58\ln(E) + 18.9\ln(\sigma_D)] * 10^{-4} \quad (4\text{-}12)$$

$$wk_f = \alpha e^{-\beta\sigma_c} \quad (4\text{-}13)$$

4.5.1 Previous Modification of the Mineralogy Distribution Dominated Model

In Jin et al. (2019), the calculated β result in a high fracture conductivity decline rate similar to Indiana limestone experiments. When the constant of 10^{-4} is changed to 10^{-5}, the decline is similar to that of the experimental results of Tests 5-9. This can be seen in Figure 4-8, where the blue line is the calculated fracture conductivity with a low correlation length, and the green line is calculated using a high correlation length. Without modification, the blue line decline to 1 md-ft around 4,000 psi of closure stress. Even though this approach does offer a decent fit to the experimental result as shown in Figure **4-8**, it is not justified because the power change affects all the constants and variables within Equation 4-12. A more accurate modification of Equation 4-12 will be presented in the next section.

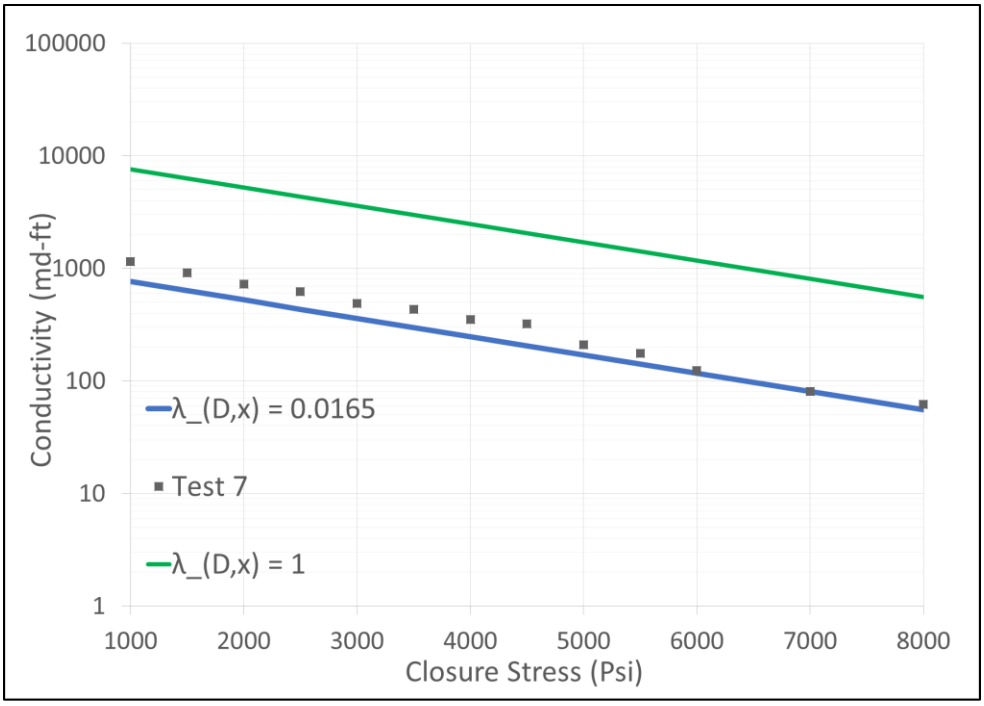

Figure 4-8: Fracture conductivity match for Test 7 (Reprinted from Jin et al., 2019).

4.5.2 Further Modification of the Mineralogy Distribution Dominated Model with Mechanical Property

If we use the β in Equation 4-8 in the mineralogy-distribution dominated correlations, we get a very similar fracture decline behavior as the modified case of Equation 4-12 with 10^{-5} instead of 10^{-4}. This is most likely the original constants in Equation 4-8 were developed to account for the slower fracture conductivity decline when the mineralogy have more complexity then just limestone/dolomite on the fracture surface. Equation 4-8 can then be improved with mechanical property testing to determine the range of Young's Modulus for the rock samples.

The new proposed mineralogy correlation for the Mou-Deng model now include Equations 4-10 and 4-11 to account for the effect of geostatistical mineralogy distribution

on the initial fracture conductivity and then Equation 4-8 instead of Equation 4-12. Equation 4-8 will be modified based on the resulting Young's Modulus values from the results of the triaxial tests of the core plugs cut using remaining core material after making the samples for downhole Tests 5-9. The competing effects correlations and the mineralogy distribution dominated correlations will be merged together to form one set of mineralogy equations benchmarked by the experimental results of Tests 5-9. The set of equations for the mineralogy model now includes Equations 4-14 through 4-17:

$$(\mathrm{wk_f})_0 = 4.48 * 10^9 \left[1 + a_1 + \left(a_2 \operatorname{erf}\left(a_3\left(\lambda_{D,x} - a_4\right)\right) - a_5 \operatorname{erf}\left(a_6\left(\lambda_{D,z} - a_7\right)\right)\right)\sqrt{e^{\sigma_D} - 1}\right] X\left[a_8 f_{calcite}^{a_9} + a_{10}\sigma_D\right]^3 w_e^{a_{11}} \quad (4\text{-}14)$$

$$\alpha = (wk_f)_0\left[0.21\lambda_{D,x}^{0.16} + 0.046\ln(\sigma_D) + 0.15\lambda_{D,z}^{-0.17}\right] \quad (4\text{-}15)$$

$$\beta = [1.2\exp(0.952 f_{calcite}) + 10.5E^{-1.823}]x10^{-4} \quad (4\text{-}16)$$

$$wk_f = \alpha e^{-\beta\sigma_c} \quad (4\text{-}17)$$

4.5.3 Modifying the Mou-Deng Mineralogy Correlation

The correlation to be modified is Equation 4-18. The constants C and D will be determined based on the triaxial test results.

$$\beta = [C\exp(0.952 f_{calcite}) + 10.5E^{-D}]x10^{-4} \quad (4\text{-}18)$$

Figure 4-9 shows the fracture conductivity results of Test 5-9. Each of the fracture conductivity fitted with an exponential curve shown in Figure 4-10. Of the five curves, the one with the highest fracture conductivity decline rate is Test 7 and the test with the lowest fracture conductivity decline rate is Test 5.

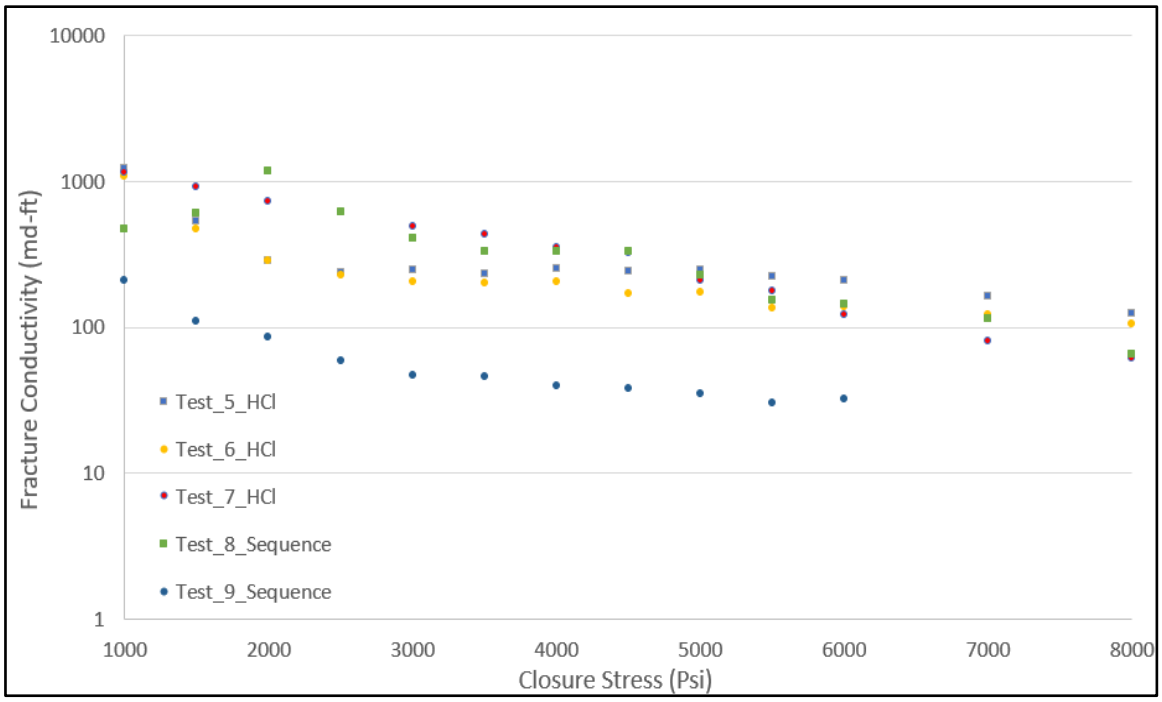

Figure 4-9: Fracture conductivity results of Test 5-9.

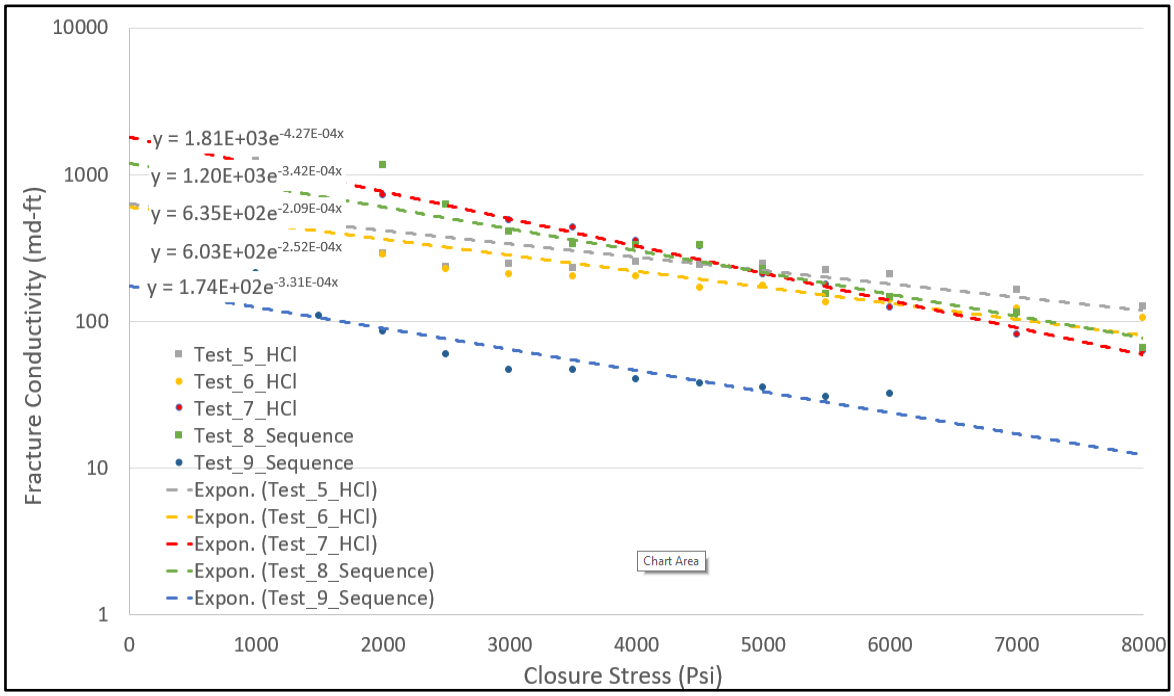

Figure 4-10: Exponential fits for Tests 5-9

Recall the goal is to obtain a corrected β (based on experimental results) in the Mou-Deng mineralogy correlations and the α in the competing correlations to fit the experimental results. In Figure 4-11, the exponential curve with the highest decline rate is shown as red dotted lines. The blue dotted lines in Figure 4-12 is Test 5, which had the slowest decline rate. In Equation 4-18, both C and D need to be changed. Because that the equation consists two variables already, $f_{calcite}$ and the Young's Modulus, the results of the XRD and triaxial test are used. With the triaxial test, Young's Modulus range of 1.91 to 5.89 Mpsi. For the XRD tests, since we only used trims to make the samples, individual XRD test does not representation the entire fracture face. However, the calcite content ranges from 80.4% to 84.6%. To match the experiment with the fastest decline rate of these samples, we use the lowest Young's Modulus (2 Mpsi) and lowest calcite percentage (80.4%). To match the experiment with the slowest decline rate, the highest Young's Modulus (6 Mpsi) and the highest calcite percentage (84.6%) are used. The two constants relating to the values of $f_{calcite}$ and Young's Modulus terms are corrected and shown in Equation 4-19. The result of the match for both tests is shown in Figure 4-11 and Figure 4-12. In both figures, the equation for the calculated line is shown on the left and the fitted line is to the right, located inside the red elipse. In Figure 4-11, the exponential has an identical value of -4.27×10^{-4}. In Figure 4-12, the exponential value was -2.09×10^{-4}. Both cases show a perfect match. Equation 4-18 can then be modified with C = 0.81 and D = -2.05, resulting in Equation 4-19, the new equation for β in the new mineralogy distribution dominated model.

$$\beta = [0.81 \exp(0.952 f_{calcite}) + 10.5E^{-2.05}]x10^{-4} \quad (4\text{-}19)$$

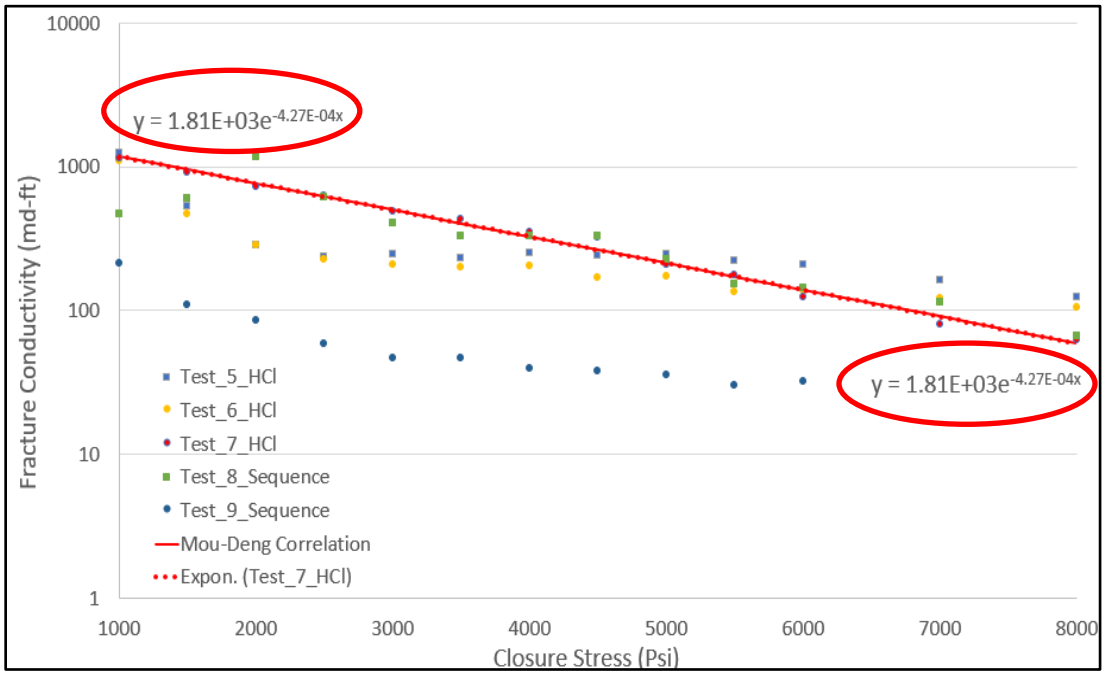

Figure 4-11: Highest decline exponential fit and modified Mou-Deng correlation match.

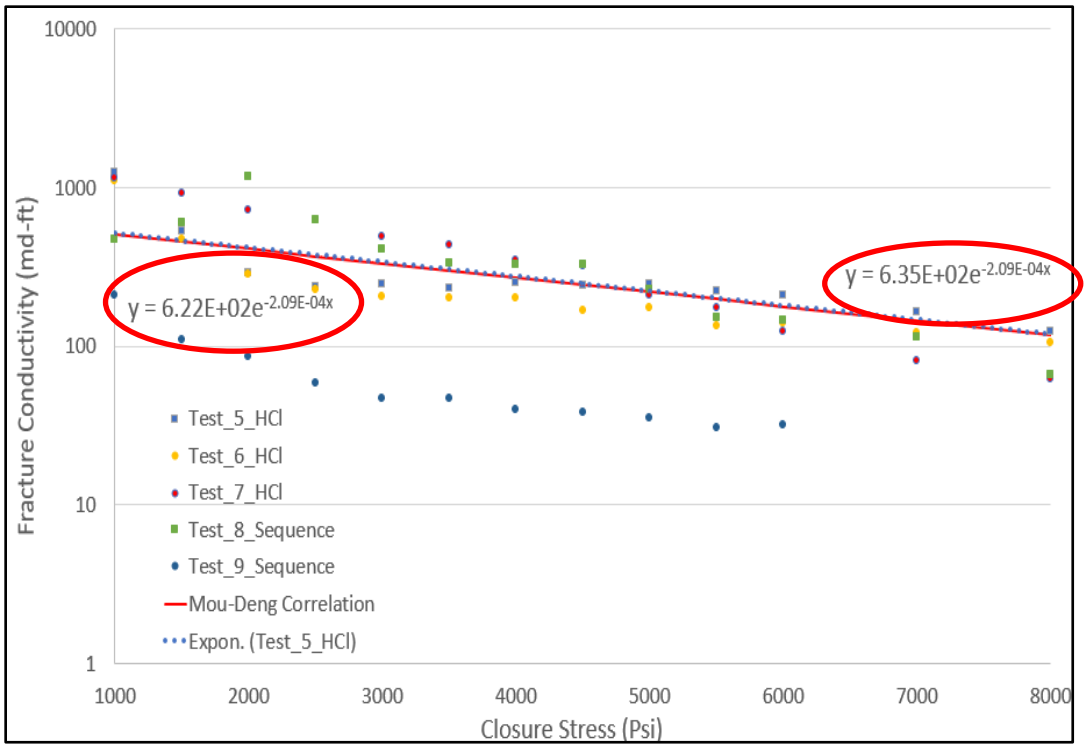

Figure 4-12: Lowest decline exponential fit and modified Mou-Deng correlation match

.

4.6 Chapter Summary

This section covered the modification of the Mou-Deng correlation by unifying the original competing effects correlation and the mineralogy correlations into one set of equations. The following conclusions are made:

- The permeability distribution dominated correlations fit the outcrop tests very well. This is expected as the correlations were benchmarked by the previously published results of Indiana Limestone tests.
- The competing effects correlations do not properly capture the fracture decline as it under predict fracture conductivity at increasing closure stress. The mineralogy distributed dominated correlations does not capture the initial fracture conductivity

because no geostatistical parameters are considered, rather only an assumption was made that the mineralogy exist as streaks perfectly parallel to flow. Since both cases consider the importance of mineralogy on the fracture face on fracture conductivity, they can be unified into one model and benchmarked by the experimental results.

- The new correlation is presented in the chapter with Equations 4-14, 4-15, and 4-17, and 4-19.

5 A FIELD CASE STUDY USING A FULLY INTEGRATED ACID FRACTURING MODEL WITH A NEW WORKFLOW

5.1 Introduction

In Chapter 4, the Mou-Deng correlation was modified to fit the experimental data. By using the experimental data fit as a benchmark, we have modified and unified both the competing-effects correlation along with the mineralogy-distribution dominated correlations into one set of equations. The modified mineralogy model now accounts for fracture conductivity changes as a function of geostatistical parameters, percentage of calcite, and the rock Young's Modulus.

In this chapter, the new correlations developed from this study are used as a part of a fully integrated acid fracturing simulator to calculate the overall fracture conductivity in a case study using field production data. In this case study, an inverse workflow (Jin et al., 2017) is used to match the production data.

5.2 Description of the Fully Integrated Acid Fracturing Model*

An acid fracturing stimulation starts with the pad fluids injection that create a hydraulically induced fracture. Then reactive fluids are injected into the fracture, often alternating with a viscous pad to create etched fracture length and create fracture conductivity. After pumping stops, the fracture closes up, and conductive declines and

---

* Reprinted with permission from Jin, X., Zhang, Hui, Yin, Guoqing et al. 2017. Applying the Integrated 3D Acid Fracturing Model Using a New Workflow in a Field Case Study. Presented at the SPE Symposium: Production Enhancement and Cost Optimisation, Kuala Lumpur, Malaysia. 2017/11/7/. https://doi.org/10.2118/189217-MS

sustained by an uneven fracture surface. A fully integrated acid fracturing model was developed and documented in detail by Aljawad (2018). The model combined an acid model with a fracture propagation model, a heat transfer model, and a reservoir flow model. The model allows the injection of multiple fluids system for both Newtonian and non-Newtonian fluids. The model incorporated multiple layer formations with different rock types and formation properties. When the acid injection is stopped, the acid concentration and etching are solved as the fracture closes. Using the etching profile, conductivity can be calculated using the Mou-Deng correlation. Using geostatistical parameters, an upper limit, and lower limit of expected fracture conductivity can be estimated. While initial fracture conductivity values will always vary due to the geostatistical parameters being more often uncertain within the target zone, the fracture conductivity decline can be characterized with a combination of XRD tests and triaxial tests. Ultimately, the fracture decline rate will often play a more important role in determining if a formation is viable for acid fracturing stimulation. In this study, the model developed by Aljawad was adopted to simulate fracture conductivity for the field case, and the new correlation was used to estimate conductivity under closure.

5.3 Data Available

The production data used for the case study is a vertical well with cased and perforated completion in a deep carbonate formation This well also had acid fracture conductivity experimental results from a previous publication (Suleimenova et al., 2015). Both oil and gas were produced from the well. The production history availability for this study

includes the surface pressure, the pressure-volume-temperature (PVT, Figure **5-1**), and the production data (Figure **5-2**).

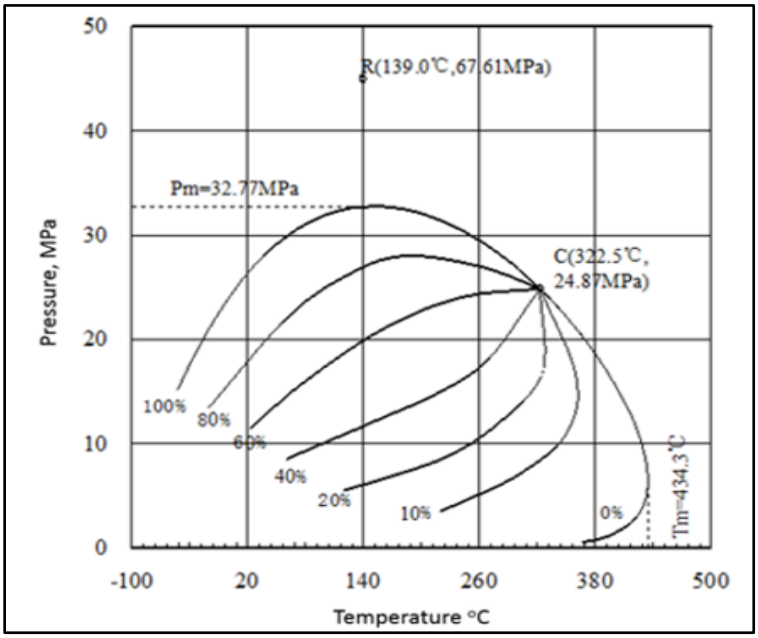

Figure 5-1: Phase diagram for case study well. (Reprinted from Jin et al., 2017).

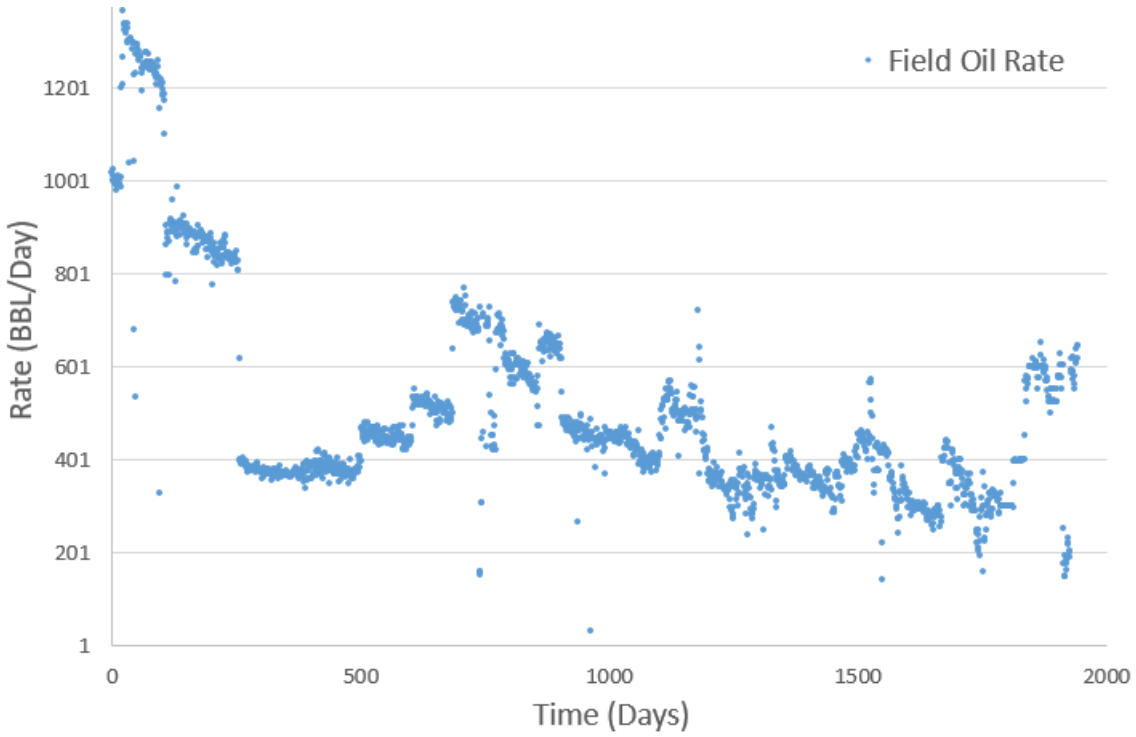

Figure 5-2: Production data for case study well.

5.3 Acid Fracturing Model Workflows

For completeness, a flowchart of the forward workflow for a forward integrated 3D acid fracturing model is shown in Figure **5-3** (Jin et al., 2017). The workflow is split into three sections, fracture propagation modeling, 3D acid fracturing simulation, and production analysis. The output of the fracture propagation model upon an adequate pressure and rate match of the treatment data is the fracture geometry. When a match is not achieved, the parameters used within the fracture propagation model, such as the injection fluids, and formation data, need to be adjusted to achieve the match. The treatment data then is used as input for 3D acid fracturing simulator. The output of the simulator is the fracture conductivity, which is then brought into the production model to match the production

data. If satisfied match is not obtained, the diagnosis of the problem and re-match will be conducted.

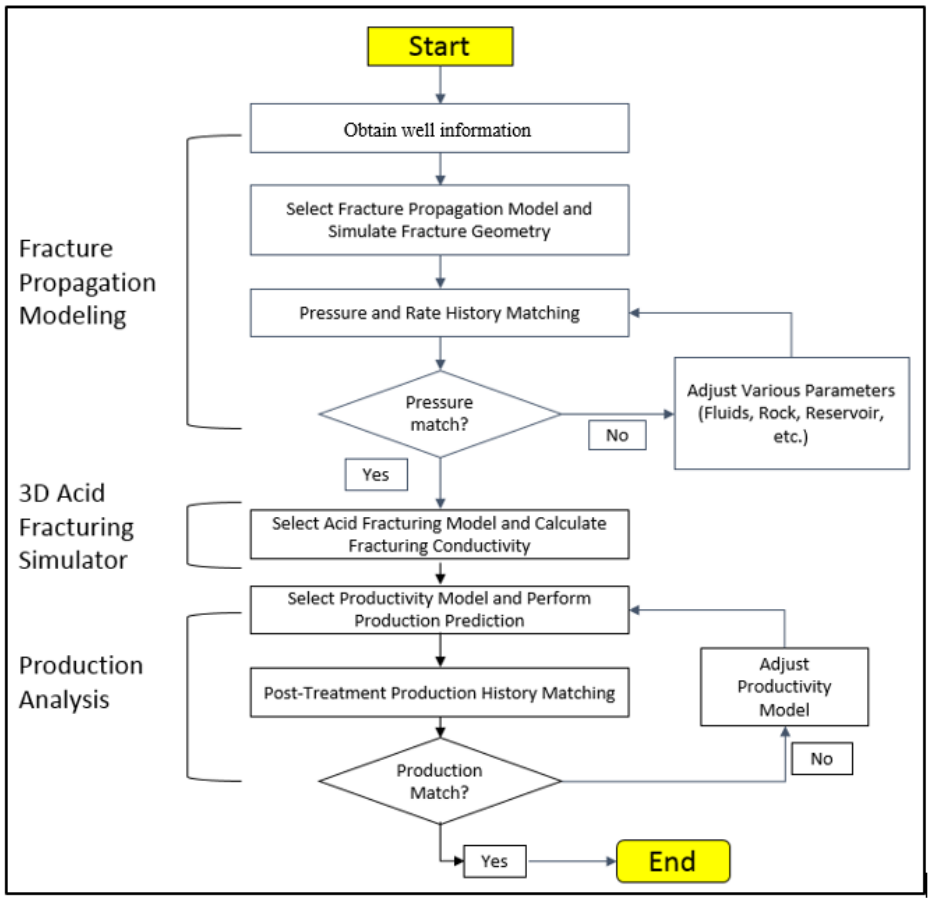

Figure 5-3: Forward flow chart (Reprinted from Jin et al., 2017).

It can be observed from the flowchart of the forward workflow that a pressure and rate match need to be achieved in order to move on with the well performance study. In this case study, this is not possible due to the missing leak-off coefficient, which would prevent the simulation of a reliable fracture geometry with the fracture propagation model; hence, a new workflow was needed. Figure **5-4** shows the inversion workflow.

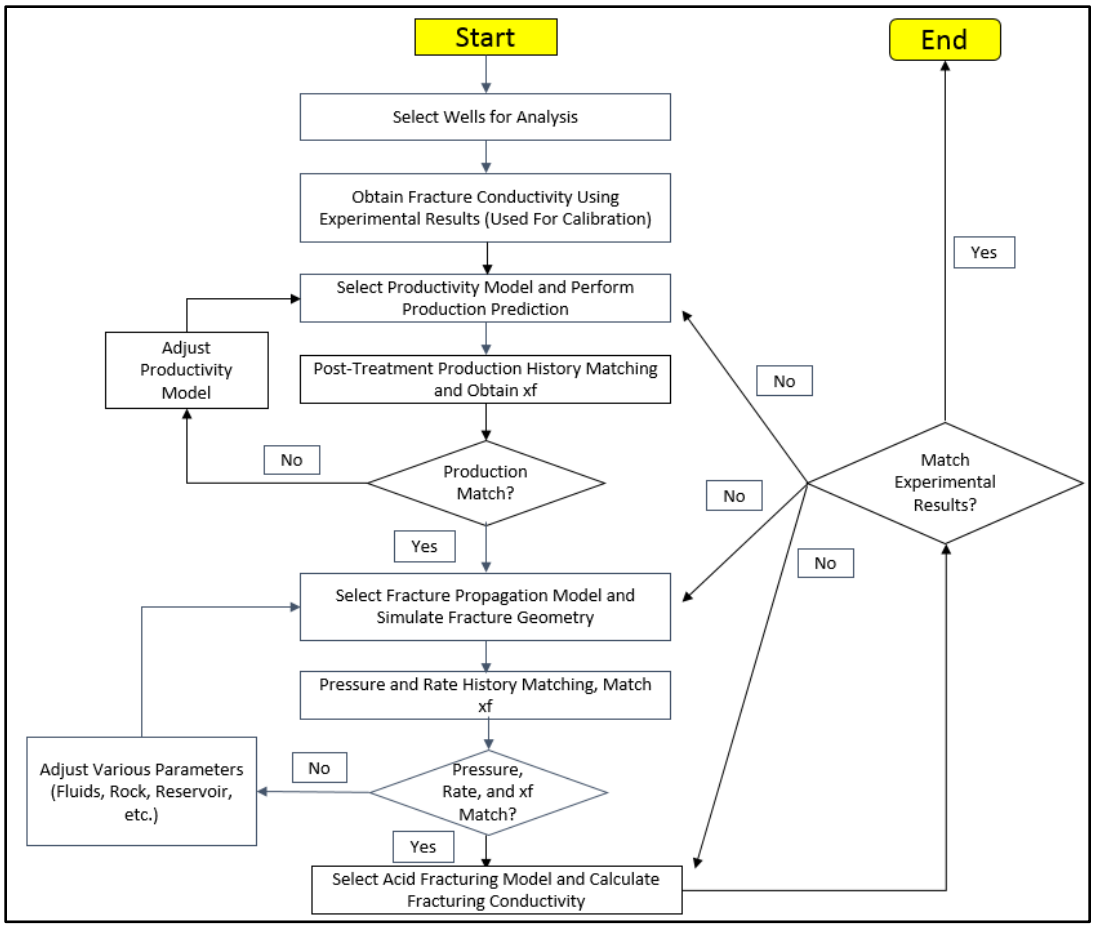

Figure 5-4: Inverse flow chart (Reprinted from Jin et al., 2017).

To obtain the fracture half-length, the production history needs to be matched, and experimental results for fracture conductivity needs to be available. In this case study, the surface pressures were converted to bottomhole pressures using the Hagedorn-Brown correlation (Hagedorn and Brown, 1965) and from the bottomhole pressures, a Vogel's two-phase correlation (1968) was used to match the oil production history.

Aljawad's acid fracturing model was used to simulate a fracture conductivity with the fracture half-length calculated from the production data. To create this fracture geometry, geomechanical data, and the leak-off coefficient of the formation must be used

as an input. This input, along with the injection fluid, has a strong effect on the simulated fracture geometry. For this case study, the leak-off coefficient was not made available. To properly simulate the fracture geometry in this situation, the production data can be used to constrain the fracture length. Once the fracture length is constrained, the leak-off coefficient is set as a variable input to match both the treatment pressure as well as the fracture length.

5.4 Applying the Inversion Workflow in the Case Study

5.4.1 Production History Analysis

Well performance models were used to perform the production history match. The performance models can be numerical reservoir simulation or analytical/semianalytical models. In this study, the generalized Vogel inflow performance model (Economides et al., 2013), derived from the original Vogel model (1968) was used. The generalized Vogel inflow model can be used to match the production data for two-phase flow with the use of absolute open flow potential utilized in the original Vogel model. To improve the match, the superposition time previously presented by Zhu and Hill (1996) for varying-rate production data, which superpose the pressure responses at different rates. The skin factor after fracturing, s_f, is adjusted to match the oil production data, which is then used to calculate the equivalent wellbore radius representing a fracture in a radial flow drainage. Using the results of this match, the equivalent wellbore radius, r_w', is calculated (Prats, 1961) by

$$r_w' = r_w e^{-s_f} \tag{5-1}$$

An analytical solution was presented by Meyer and Jacot (2005) for pseudo steady state for fractured well productivity with finite conductivity. It uses the previously calculated r_w' to represent a fracture in a radial flow drainage. This equation should be used when the fracture half-length is much smaller than the reservoir drainage area, r_e, due to the radial flow assumption. In this case study, the estimated reservoir drainage radius used was approximately 1,200 feet, which was part of the reservoir data provided initially by the owner of the well.

$$r_w' = \frac{x_f}{\frac{\pi}{C_{fD}}+2} \tag{5-2}$$

where,

$$C_{fD} = \frac{k_f w}{k x_f} \tag{5-3}$$

To match the daily flow rate, bottomhole pressure is needed. The surface pressures were provided for each well and converted to the bottomhole pressures with the Hagedorn and Brown correlation (1965).

The well performance model (the generalized Vogel flow described in the methodology) was used to match the production rate. The result is a reasonably good match shown in **Figure 5-5** considering details of production management were not provided. The post-treatment skin factor was determined to be -5.4. From acid fracturing experimental results on the relationship between closure stress and fracture conductivity, the fracture conductivity can be obtained. **Figure 5-6** (Suleimenova et al., 2016) is created

from core samples in the vicinity of the well. The conductivity from Well1/Sample A test has a value of 55 md-ft at closure stress of 4854 psi (from provided geomechanical data). Using Equation 5-2, the calculated fracture half-length is 193 feet as function of the fracture conductivity, effective wellbore radius, and formation permeability. This fracture half-length will be used in the fracture propagation model to calibrate the fracture geometry obtained from Mfrac.

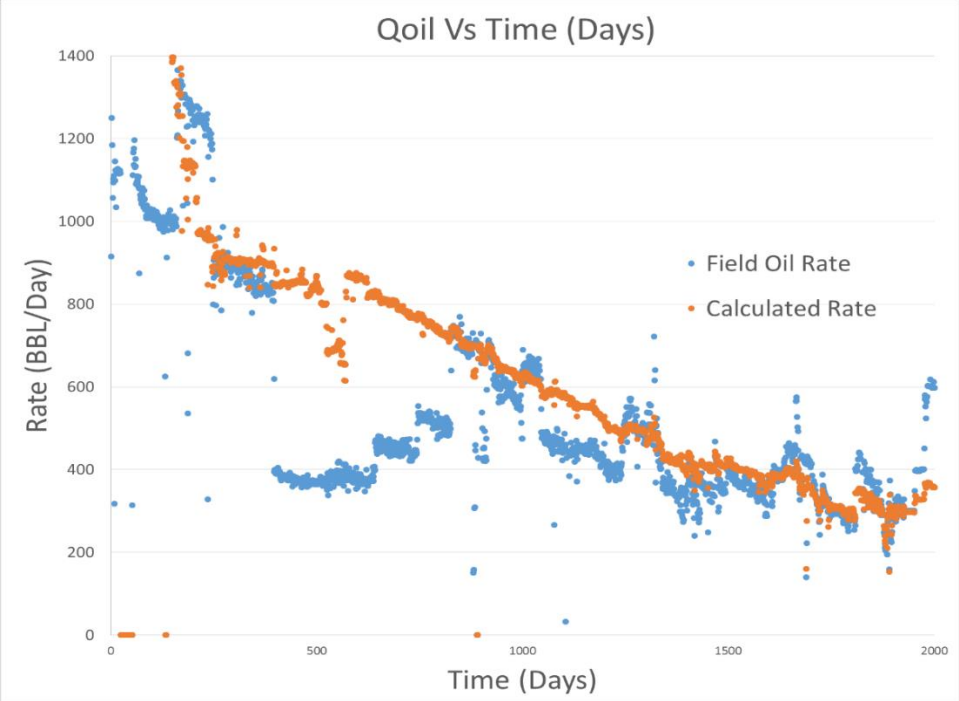

Figure 5-5: Production rate match for Well A (Reprinted from Jin et al., 2017).

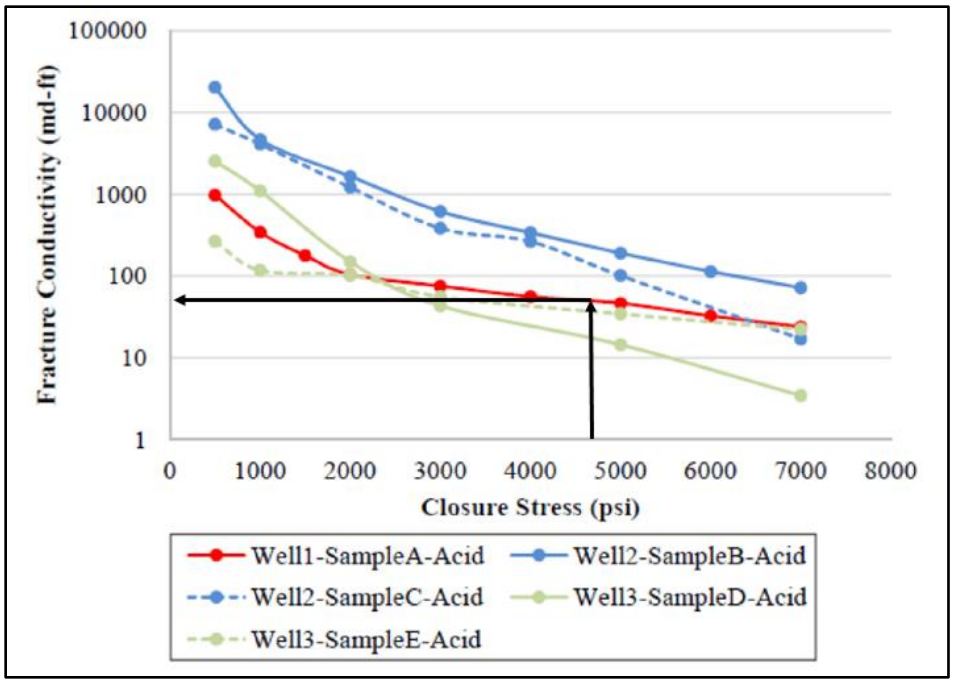

Figure 5-6: Experimental fracture conductivity results (Reprinted from Suleimenova, 2016).

5.4.4 Acid Fracturing Simulation Results Using the Aljawad Model

Originally, the geomechanical pressure values are calculated every 10 feet. However, due to input limitations of the acid fracturing model, having too many layers convergence issues. Five layers of geomechanical inputs were used in this simulation. Each layer is an average across 80 feet of the original geomechanical properties. The averaged geomechanical properties are shown in **Table 5-1**. The target zone is located at 20450 feet in the vertical well. The minimum horizontal stress is estimated to be over 15,000 psi.

Table 5-1: Geomechanical Properties

Layer	TVD (ft)	Thickness(ft)	Stress (psi)	E (psi)	υ
1	0	20370	15674	4.1E6	0.27
2	20370	80	15650	4.06E6	0.27
3	20450	80	15412	3.8E6	0.26
4	20530	80	15727	3.93E6	0.26
5	20610	1000	15851	3.95E6	0.27

The leak-off coefficient was adjusted until the fracture half-length was 193 feet. This also resulted in a fracture height of 450 feet and fracture width of 0.22 feet. The geostatistical parameters used to calculate the overall fracturing conductivity include a low correlation length of 0.1 for both directions since the fracture face has HCl-insoluble perpendicular against the flow (Figure **5-7**, Suleimenova 2015). The calculated closure stress is 4854 psi based on the in-situ stress and the bottomhole flowing pressure. The simulation calculated a fracture conductivity of 52 md-ft. The approximate fracture conductivity from the experiment, as shown in Figure 5-6, is a comparable result of 55 md-ft.

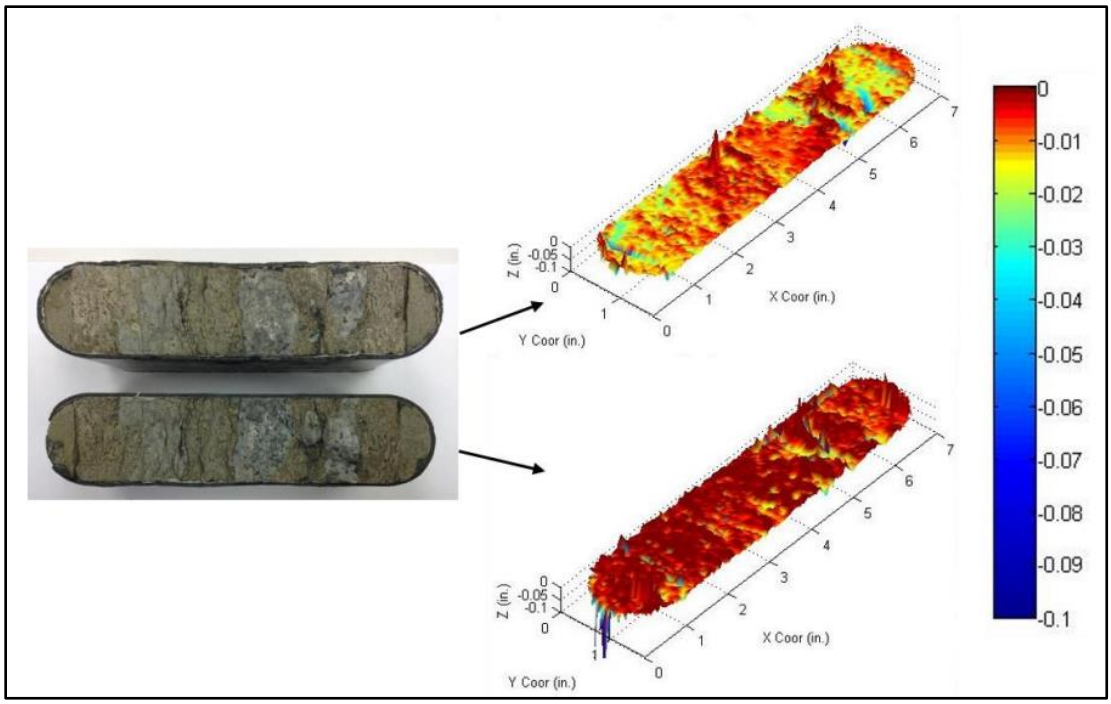

Figure 5-7: Acid-etched sample surface scans (Reprinted from Suleimenova, 2015).

6. SUMMARY AND RECOMMENDATIONS

6.1 Conclusions

This dissertation presents a series of acid fracturing experimental with both outcrop samples and downhole core samples. Traditionally outcrops are commonly used to study acid fracturing conductivity and provide qualitative examples of expected acid fracturing outcomes with various design parameters such as the acid system, acid injection rate, contact time, and temperature. These samples are usually dominated by either calcite or dolomite.

Two sets of downhole samples were available and offered important insights into acid fracturing conductivity at downhole conditions. These samples from both a U.S. onshore location and a Middle East location presented a heterogeneity with higher HCl-insoluble materials. These HCl-insoluble minerals have stronger mechanical properties and provided a more sustained fracture conductivity at higher closure stress. This is important because acid fracturing is a cheaper stimulation method than hydraulic fracturing (a commonly considered alternative), and without tests showing enough fracture conductivity at higher closure stresses, acid fracturing maybe overlooked as the treatment choice.

Some of the key conclusions from this study are summarized below:

- Acid fracturing can be an effective stimulation technique for the Ratawi limestone formation based on the sustained fracture conductivity values at higher closure stresses.

- From the testing of the analog limestone samples, calcite content greater than 80% and total HCl-insoluble content being between 5-10% could significantly limit the fracture conductivity decline at higher closure stress.
- Too much HCl-insoluble mineral (>15%) on the fracture surface could lead to poor initial fracture conductivity, canceling the benefit of the slow fracture decline behavior provided by HCl-insoluble minerals.
- Low reactivity fluids (such as linear gel) are not recommended for formation zones low in calcite content at the reservoir temperature of 140° F.
- For high calcite content zones, sequence injection created channel-like dissolution, which enhanced conductivity.

6.2 Limitations and Recommendations

The primary limitation on the experimental study is the direction at which the samples were obtained from downhole. Fracture conductivity sets with downhole samples can only be obtained along the direction where the wellbore is drilled. Side walled samples are not big enough to be cut into 7-in length fracture conductivity sets. This would result in laboratory injection direction to be perpendicular to the injection direction of field operation. This is the reason that the mineral streaks on the fracture face are often perpendicular to flow. This would under predict the initial fracture conductivity tested at laboratory conditions. The fracture decline rate is less affected as it accounts for the mineralogy and the mechanical property of the rock only rather than mineralogy distribution. Hence, these laboratory experiments can be seen mostly as low-end fracture conductivity values compared to field expectations.

REFERENCES

Aljawad, M. S. 2018. *Development of a Fully Integrated Acid Fracture Model.* PhD dissertation, Texas A&M University, College Station, Texas (May 2018).

Aljawad, M. S., Zhu, D., and Hill, A. D. 2016. Modeling Study of Acid Fracture Fluid System Performance. Presented at the SPE Hydraulic Fracturing Technology Conference, The Woodlands, Texas, USA. 2016/2/1/. https://doi.org/10.2118/179109-MS.

Almomen, A.M. . 2013. The Effects of Initial Conditions of Fracture Surfaces, Acid Spending, and Type on Conductivity of Acid Fracture. *MSc Thesis, Texas A&M University, 2013*.

Bale, Arthur, Smith, Michael Berry, and Klein, Henry H. 2010. Stimulation of Carbonates Combining Acid Fracturing With Proppant (CAPF): A Revolutionary Approach for Enhancement of Final Fracture Conductivity and Effective Fracture Half-Length. Presented at the SPE Annual Technical Conference and Exhibition, Florence, Italy. 2010/1/1/. https://doi.org/10.2118/134307-MS.

Barron, A. N., Hendrickson, A. R., and Wieland, D. R. 1962. The Effect of Flow on Acid Reactivity in a Carbonate Fracture. *Journal of Petroleum Technology* **14** (04): 409-415. https://doi.org/10.2118/134-PA.

Bartko, K. M., Nasr-El-Din, H. A., Rahim, Z. et al. 2003. Acid Fracturing of a Gas Carbonate Reservoir: The Impact of Acid Type and Lithology on Fracture Half Length and Width. Presented at the SPE Annual Technical Conference and Exhibition, Denver, Colorado. 2003/1/1/. https://doi.org/10.2118/84130-MS.

Ben-Naceur, K. and Economides, Michael J. 1988. The Effectiveness of Acid Fractures and Their Production Behavior. Presented at the SPE Eastern Regional Meeting, Charleston, West Virginia. 1988/1/1/. https://doi.org/10.2118/18536-MS.

Broaddus, G. C., Knox, J. A., and Fredrickson, S. E. 1968. Dynamic Etching Tests And Their Use In Planning Acid Treatments. Presented at the SPE Oklahoma Regional Meeting, Stillwater, Oklahoma. 1968/1/1/. https://doi.org/10.2118/2362-MS.

Deng, Jiayao, Mou, Jianye, Hill, Alfred D. et al. 2012. A New Correlation of Acid-Fracture Conductivity Subject to Closure Stress. *SPE Production & Operations* **27** (02): 158-169. https://doi.org/10.2118/140402-PA.

Economides, M.J., Hill, A.D., Ehlig-Economides, C. et al. *Petroleum Production Systems.* Prentice Hall, 2013.

Frasch, H. and Van Dyke, J.W. 1896. Increasing the Flow of Oil Wells. *US Patent No 556,669*.

Gomaa, Ahmed M., Mahmoud, Mohamed A., and Nasr-El-Din, Hisham A. 2011. Laboratory Study of Diversion Using Polymer-Based In-Situ-Gelled Acids. *SPE Production & Operations* **26** (03): 278-290. https://doi.org/10.2118/132535-PA.

Gong, Ming, Lacote, Stephan, and Hill, A. D. 1999. New Model of Acid-Fracture Conductivity Based on Deformation of Surface Asperities. *SPE Journal* **4** (03): 206-214. https://doi.org/10.2118/57017-PA.

Grebe, J.J. and Stoesser, S.M. 1935. Treatment of Deep Wells. *Patent No 1,998,756*.

Guerra, Jesse, Zhu, Ding, and Hill, Alfred D. 2018. Impairment of Fracture Conductivity in the Eagle Ford Shale Formation. *SPE Production & Operations* **33** (04): 637-653. https://doi.org/10.2118/184857-PA.

Hagedorn, Alton R. and Brown, Kermit E. 1965. Experimental Study of Pressure Gradients Occurring During Continuous Two-Phase Flow in Small-Diameter Vertical Conduits. *Journal of Petroleum Technology* **17** (04): 475-484. https://doi.org/10.2118/940-PA.

Hill, Alfred Daniel, Pournik, Maysam, Zou, ChunLei et al. 2007. Small-Scale Fracture Conductivity Created by Modern Acid Fracture Fluids. Presented at the SPE Hydraulic Fracturing Technology Conference, College Station, Texas, U.S.A. 2007/1/1/. https://doi.org/10.2118/106272-MS.

Jin, X. 2013. *Experimental Investigation For the Effects of the Core Geometry on the Optimum Acid Flux in Carbonate Acidizing.* M.S. Thesis, Texas A&M University, College Station, Texas (December 2013).

Jin, X., Zhang, Hui, Yin, Guoqing et al. 2017. Applying the Integrated 3D Acid Fracturing Model Using a New Workflow in a Field Case Study. Presented at the SPE Symposium: Production Enhancement and Cost Optimisation, Kuala Lumpur, Malaysia. 2017/11/7/. https://doi.org/10.2118/189217-MS.

Jin, Xiao, Zhu, Ding, Hill, Alfred Daniel et al. 2019. Effects of Heterogeneity in Mineralogy Distribution on Acid-Fracturing Efficiency. *SPE Production & Operations* **Preprint** (Preprint): 14. https://doi.org/10.2118/194377-PA.

Lo, K. K. and Dean, R. H. 1989. Modeling of Acid Fracturing. *SPE Production Engineering* **4** (02): 194-200. https://doi.org/10.2118/17110-PA.

Melendez, Maria Georgina, Pournik, Maysam, Zhu, Ding et al. 2007. The Effects of Acid Contact Time and the Resulting Weakening of the Rock Surfaces on Acid Fracture Conductivity. Presented at the European Formation Damage Conference, Scheveningen, The Netherlands. 2007/1/1/. https://doi.org/10.2118/107772-MS.

Meyer, Bruce Roman and Jacot, Robert Henry. 2005. Pseudosteady-State Analysis of Finite Conductivity Vertical Fractures. Presented at the SPE Annual Technical Conference and Exhibition, Dallas, Texas. 2005/1/1/. https://doi.org/10.2118/95941-MS.

Mou, Jianye, Zhu, Ding, and Hill, Alfred D. 2010. Acid-Etched Channels in Heterogeneous Carbonates--a Newly Discovered Mechanism for Creating Acid-Fracture Conductivity. *SPE Journal* **15** (02): 404-416. https://doi.org/10.2118/119619-PA.

Naik, Sarvesh, Dean, Mark, McDuff, Darren et al. 2020. Acid Fracture Conductivity Testing on the Tight Carbonate Ratawi Limestone in the Partitioned Zone. Presented at the International Petroleum Technology Conference, Dhahran, Kingdom of Saudi Arabia. 2020/1/13/. https://doi.org/10.2523/IPTC-19724-Abstract.

Nasr-El-Din, Hisham A., Samuel, Elsamma, and Samuel, Mathew. 2003. Application of a New Class of Surfactants in Stimulation Treatments. Presented at the SPE International Improved Oil Recovery Conference in Asia Pacific, Kuala Lumpur, Malaysia. 2003/1/1/. https://doi.org/10.2118/84898-MS.

Neumann, Luis Fernando, Sousa, Jose Luiz A. O., Brandao, Edimir M. et al. 2012. Acid Fracturing: New Insigths on Acid Etching Patterns from Experimental Investigation. Presented at the SPE Hydraulic Fracturing Technology Conference, The Woodlands, Texas, USA. 2012/1/1/. https://doi.org/10.2118/152179-MS.

Nierode, D. E. and Kruk, K. F. 1973. An Evaluation of Acid Fluid Loss Additives Retarded Acids, and Acidized Fracture Conductivity. Presented at the Fall Meeting of the Society of Petroleum Engineers of AIME, Las Vegas, Nevada. 1973/1/1/. https://doi.org/10.2118/4549-MS.

Nierode, D. E., Williams, B. R., and Bombardieri, C. C. 1972. Prediction of Stimulation From Acid Fracturing Treatments. *Journal of Canadian Petroleum Technology* **11** (04): 12. https://doi.org/10.2118/72-04-04.

Nieto, Camilo Malagon, Pournik, Maysam, and Hill, Alfred D. 2008. The Texture of Acidized Fracture Surfaces: Implications for Acid Fracture Conductivity. *SPE Production & Operations* **23** (03): 343-352. https://doi.org/10.2118/102167-PA.

Oeth, C. V., Hill, A. D., and Zhu, D. 2014. Acid Fracture Treatment Design with Three-Dimensional Simulation. Presented at the SPE Hydraulic Fracturing Technology Conference, The Woodlands, Texas, USA. 2014/2/4/. https://doi.org/10.2118/168602-MS.

Oeth, Cassandra, Hill, Alfred Daniel, Zhu, Ding et al. 2011. Characterization of Small Scale Heterogeneity to Predict Acid Fracture Performance. Presented at the SPE Hydraulic Fracturing Technology Conference, The Woodlands, Texas, USA. 2011/1/1/. https://doi.org/10.2118/140336-MS.

Prats, M. 1961. Effect of Vertical Fractures on Reservoir Behavior-Incompressible Fluid Case. *Society of Petroleum Engineers Journal* **1** (02): 105-118. https://doi.org/10.2118/1575-G.

Romero, J., Gu, H., and Gulrajani, S. N. 2001. 3D Transport in Acid-Fracturing Treatments: Theoretical Development and Consequences for Hydrocarbon Production. *SPE Production & Facilities* **16** (02): 122-130. https://doi.org/10.2118/72052-PA.

Ruffet, C., Fery, J. J., and Onaisi, A. 1998. Acid Fracturing Treatment: a Surface Topography Analysis of Acid Etched Fractures to Determine Residual Conductivity. *SPE Journal* **3** (02): 155-162. https://doi.org/10.2118/38175-PA.

Settari, A., Sullivan, R. B., and Hansen, Chris. 2001. A New Two-Dimensional Model for Acid-Fracturing Design. *SPE Production & Facilities* **16** (04): 200-209. https://doi.org/10.2118/73002-PA.

Settari, Antonin. 1993. Modeling of Acid-Fracturing Treatments. *SPE Production & Facilities* **8** (01): 30-38. https://doi.org/10.2118/21870-PA.

Suleimenova, A. 2015. *Acid Fracturing Feasibility Study For Heterogeneous Carbonate Formation.* M.S. Thesis, Texas A&M University, College Station, Texas (May 2015).

Tansey, J.F. 2015. Pore Network Modeling of Carbonate Acidization. *MSc Thesis, University of Texas at Austin, 2015*.

Terrill, R.M. 1965. Heat Transfer in Laminar Flow Between Parallel Porous Plates. *International Journal of Heat and Mass Transfer*.

Ueda, K., Zhang, W., Zhu, D. et al. 2016. Evaluation of Acid Fracturing by Integrated Pressure Analysis and 3D Simulation: A Field Application for Multi-Stage Stimulation in Horizontal Wells. Presented at the SPE Hydraulic Fracturing Technology Conference, The Woodlands, Texas, USA. 2016/2/1/. https://doi.org/10.2118/179123-MS.

Vogel, J. V. 1968. Inflow Performance Relationships for Solution-Gas Drive Wells. *Journal of Petroleum Technology* **20** (01): 83-92. https://doi.org/10.2118/1476-PA.

Williams, B. B. and Nierode, D. E. 1972. Design of Acid Fracturing Treatments. *Journal of Petroleum Technology* **24** (07): 849-859. https://doi.org/10.2118/3720-PA.

Wu, Xi, Hill, Alfred Daniel, Oeth, Cassandra et al. 2013. Integrated 3D Acid Fracturing Model for Carbonate Reservoir Stimulation. Presented at the OTC Brasil, Rio de Janeiro, Brazil. 2013/10/29/. https://doi.org/10.4043/24362-MS.

Zhu, Ding and Hill, A. Daniel. 1996. Field Results Demonstrate Enhanced Matrix Acidizing Through Real-Time Monitoring. Presented at the Permian Basin Oil and Gas Recovery Conference, Midland, Texas. 1996/1/1/. https://doi.org/10.2118/35197-MS.

Zou, C. 2006. Development and Testing of an Advanced Acid Fracture Conductivity. *MSc Thesis, Texas A&M University, 2006*.

NOMENCLATURE

C_{fD}	Dimensionless fracture conductivity
E	Young's modulus. Mpsi
$f_{calcite}$	Fraction of calcite in the formation
k	Formation permeability, md
k_f	Fracture permeability, md
r_w	Wellbore radius, ft.
r_w'	Effective wellbore radius, ft.
s_f	Equivalent skin factor
w	Fracture width, in.
w_i	Ideal fracture width
wk_f	Fracture conductivity
x_f	Fracture half-length
α, β	Mou-Deng correlation's constants
$\lambda_{D,x}$	Correlation length in horizontal direction
$\lambda_{D,z}$	Correlation length in vertical direction
σ_D	Normalized permeability standard deviation